Monte Carlo based comparison of constant vs. variable RBE for proton therapy patients

Johan Martin Søbstad
Supervisors: Kristian Ytre-Hauge and Sara Thørnqvist

MASTER THESIS IN MEDICAL PHYSICS
Department of Physics and Technology

UNIVERSITY OF BERGEN

June 2017

2017

Monte Carlo based comparison of constant vs. variable RBE for proton therapy patients

Johan Martin Søbstad

https://bora.uib.no/

Abstract

Around the world, the use of protons as an alternative to photons in radiation therapy of cancer is becoming more widespread. The motivations for this is that protons enable a reduction of the radiation dose to healthy tissue or increase the dose to the tumor when compared to photons. However, there is currently an uncertainty related to the biological effectiveness of protons. Protons are known to be slightly more efficient in cell inactivation than photons, which can be quantified by the relative biological effectiveness (RBE), a scaling factor. In current clinical practice a constant RBE factor of 1.1 is applied. However, several studies including data from cell irradiation experiments suggest that a variable RBE factor is more appropriate. The primary objective of this project was to calculate and compare the dose-to-patient results of constant RBE versus variable RBE calculated by different models for protons.

The calculations were done by a combination of FLUKA Monte Carlo (MC) simulations and post-processing using custom scripts written in Python. CT images and treatment plan information for a medulloblastoma patient was imported into FLUKA, where the dose and linear energy transfer (LET) was calculated. The RBE values were subsequently calculated for four different models, assuming constant tissue parameters. An in-depth investigation of the different model properties was performed by systematically varying the model parameters. RBE calculations with a simple treatment plan on a water phantom were also performed.

The models consistently predicted an equal or lower dose in the beam-entrance region compared to predictions for RBE = 1.1 ($RBE_{1.1}$) while greatly exceeding the predicted $RBE_{1.1}$ dose in the distal part of the planning target volume (PTV) and in the distal dose-falloff. There was also a considerable increase in dose distributed in the lateral direction for the PTV. The dose volume histograms (DVHs) revealed that structures located in close proximity to the PTV receive considerably higher levels of dose than predicted by $RBE_{1.1}$ due to a high RBE factor, at times double that of the constant RBE. The RBE models also show a strong dependence on dose. The models appear to be largely in agreement, and the mean RBE varies about 1.4% in the PTV. However, the mean RBE variation increases at lower doses, such as in the esophagus with 6.3% variation. For a prescribed dose of 23.4 Gy to the PTV, the mean dose to the PTV varied between 24.9 and 25.7 for the different models, while for the lungs and esophagus the mean dose varied between 3.79-4.03 and 10.2-11.5, respectively.

The results show that while the models estimations differ, they consistently deviate from the dose predicted using RBE of 1.1. For the investigated patient case RBE values from 1.1 to 1.4 were seen for the target volume, while similar and higher RBE values were also observed for several healthy tissues, and this could be of clinical relevance. This leads to the conclusion that implementing a variable RBE into clinical scenarios should be considered. At least, practitioners should use the results provided by MC as guidance for assessing the dose until more experimental data and accurate models becomes available.

Acknowledgements

I would like to thank everyone who have assisted and supported me during the work with this master thesis. First I would like to thank my supervisors, Res. Kristian Smeland Ytre-Hauge and Assoc. Prof. II Sara Thørnqvist.

Thank you, Kristian Smeland Ytre-Hauge, for presenting a variety of interesting topics and providing me with inspiration and the necessary tools for writing this thesis. Your guidance and professional commentary and input has been invaluable.

Thank you, Sara Thörnqvist, for providing helpful and optimistic guidance, as well as reading through my thesis, providing insightful comments and suggestions. Also, thanks for the short visit to the radiology department.

I would also like to thank Ph.D. candidates Eivind Rørvik and Lars Fredrik Fjæra, for their help, ideas and comments. Thank you, Eivind for reading though my thesis on several occasions, providing excellent feedback, both positive and negative, as well as pushing me to dig deeper into articles to find additional information and data. Thank you, Lars for guiding me though the programming-labyrinth known as DICOM and for providing me with useful up-to-date python-scripts from your own thesis.

Thanks to Camilla Hanquist Stokkevåg for providing the patient CT and treatment plan used in this thesis.

Additionally, I would like to thank my friend and study buddy Yannick Alexander Broese van Groenou, for coping with me over the last two years. Your friendship, study skills and our internal humor and conversations has been uplifting, hilarious and vital to where and how I am today. If it were not for you, I might not have chosen this topic, thank you.

Finally, a special thank you to my wonderful parents, Helge Søbstad and Sølvi Irene Bergstrøm Søbstad, as well as my brothers and sister. Our internal humor is legendary and is part of why I have been able to cope with the fatigue of studying for so long. Your support is invaluable to me and I am eternally grateful that you are all still with me. Asking me for help with your physics and math homework has been a pleasant distraction.

Bergen, June 2017
Johan Martin Søbstad

Contents

List of Figures and Tables

List of Abbreviations

CAR	**Car**abe-Fernandez et al. model
CPT	**C**linical **P**article **T**herapy
CSV	**C**omma-**S**eparated **V**alues
DICOM	**D**igital **I**maging and **Co**mmunications in **M**edicine
DSB	**D**ouble-**S**trand **B**reak
DVH	**D**ose **V**olume **H**istogram
HUH	**H**aukeland **U**niversity **H**ospital
ICRP	**I**nternational **C**ommission on **R**adiological **P**rotection
ICRU	**I**nternational **C**ommission on **R**adiation **U**nits
kVp	**P**eak-**K**ilo **V**oltage
LET	**L**inear **E**nergy **T**ransfer
LET_D	**L**inear **E**nergy **T**ransfer (**D**ose average)
Linac	**Lin**ear **Ac**celerator
LQ	**L**inear **Q**uadratic model
MC	**M**onte **C**arlo
MCN	**McN**amara et al. model
MLC	**M**ulti-**L**eaf **C**ollimator
OAR	**O**rgan **A**t **R**isk
PB	**P**encil **B**eam
PTV	**P**lanning **T**arget **V**olume
RBE	**R**elative **B**iological **E**ffectiveness
RT	**R**adio **T**herapy
SE	**S**tandard **E**rror
SF	**S**urvival **F**raction
SOBP	**S**pread-**O**ut **B**ragg **P**eak
TPS	**T**reatment **P**lanning **S**ystem
WED	**Wed**enberg et al. model
WIL	**Wil**kens et al. model

1 Introduction

In 2014, over 30000 new incidences of cancer was registered in Norway (Larsen et al., 2015). The last few years has had a slow but steady increase in rates for all cancers combined, most likely due to a population increase, as well as a shift towards an older population. It is predicted that the occurrences will increase by 20% from 2010 to 2020 (Helse-Vest, Helse-Sør-Øst, Helse-Midt, Helse-Nord, & Helsedirektoratet, 2013). A clear majority (about 85-90%) of cancers are diagnosed among people aged 50 years and older.

Also in 2014, roughly 11000 patients died of cancer, of which, cancers of the lung, colon, rectum, prostate and breast accounted for half of the mortality (Larsen et al., 2015). About half of all cancer patients also receive radiotherapy, and it contributes significantly as to how we cure many patients today (Ånensen, 2013). In 2015, about 50 Norwegian cancer patients were treated in other countries to receive treatment with proton therapy, due to regular radiotherapy being insufficient (Hartmann, 2016).

1.1 Radiotherapy

The dawn of radiotherapy was back in Nov 1895, when W. C. Rontgen discovered x-rays and its ability to excite chemicals to fluorescence. Using these invisible rays Rontgen could, using photographic plates placed behind what was being 'photographed', capture an image of the bony anatomy of his wife's hand. A two months later on Jan 1896, E. H. Grubbé, a manufacturer of incandescent lamps and a medical student, had developed an inflammatory area on the back of his hand after multiple exposures every day to x-rays. After this observation, it was suggested that there might be other beneficial therapeutic uses of these rays (Lederman, 1981).

Shortly after on Jan 29th, 1896, the first cancer patient was treated. This was done by placing an x-ray tube close to the lesion and allowing a full hour of exposure using a lead sheet to shield the healthy tissue surrounding the lesion; radiotherapy was born (Lederman, 1981).

Since then, radiotherapy has undergone a wide range of technological developments, such as moving from the old x-ray tube and cobalt-60 machines to todays linear accelerators (linacs). These allows for higher energies and deeper penetration than ever before and is the standard for radiotherapy. Today, out of the patients with cancer receiving radiation therapy, over 86% are treated with photons, whereas treatment using compact linear accelerators is the dominating treatment technique, given to roughly 80% of the therapy patients. Other photon therapy techniques e.g. brachytherapy and gamma knife are given to the rest of the patients. Particle therapy is still a rare treatment with is received by about 0.8% of the patients (Durante & Paganetti, 2016).

The term particle therapy usually refers to charged particle therapy (CPT), which involves the use of particles such as protons, which is the primary particle used in this thesis. Another form of CPT also in use and more common is electrons, but they are mostly used for shallow tumors

due to their light mass and consequently rapid slowdown. Hadronic therapy in general, i.e. such as the use of protons, also include the use of heavier ions such as helium or carbon (Jones, Underwood, & Dale, 2011).

1.2 Proton therapy

In July 1946, R. R. Wilson released an article suggesting the use of protons as a possible particle therapy candidate (Wilson, 1946). This was due to the depth-dose distribution of the protons which, unlike for photons, had an increasing effect with the depth. At the time, machines which could yield protons of energy 125 MeV or more were under construction which would allow for penetration up to 12 cm. Full penetration to any part of the body or up to 27 cm would require a 200 MeV beam (Wilson, 1946).

Wilson noted that as the proton traversed through the tissue it would travel in a near-straight line and ionize the tissue at the cost of the its own energy. The dosage would be inversely proportional to the proton energy and be at its highest in the last stretch before the proton would come to a halt. This would mean that, unlike in conventional radiotherapy, a single field could deposit more dose in the target area than in the entrance area, sparing more of the healthy tissue (Wilson, 1946).

The first patients were treated with protons at Lawrence Berkeley National Laboratory in California in 1958. Now, over 50 years later, an increasing number of particle therapy centers are opening or under construction all over the world. However, clinical implementation has been limited by the great costs of these facilities and has led to a debate over the cost over benefit ratio of CPT among scientists (Durante & Paganetti, 2016; McDonald & Fitzek, 2010). The cost however is steadily decreasing and the technology is becoming more available (McDonald & Fitzek, 2010).

Most advantages associated with CPT, in this case protons, lies in the possibility to deliver the energy very selectively (Belli, Campa, & Ermolli, 1997). As described by Wilson, this possibility lies in the Bragg peak, the position at which the energy deposition is at its maximum (Wilson, 1946). The Bragg peak is especially important when organs at risk (OARs) are located directly behind the target (Belli et al., 1997). This is due to the sharp decrease in deposition of dose as most of the protons come to a halt. The uncertainty of this range becomes very important, and increases with increasing range due to range straggling (section 2.1.4). Figure 1-1 visualizes the advantage of the Bragg peak when looking at the dose deposition for protons vs photons. From a more clinical perspective figure 1-2 shows the same advantage, but during treatment to the brain.

The range of the proton beam and thus the position of the Bragg peak is highly dependent on the initial energy. In proton therapy, multiple Bragg peaks can be used to spread out the dose over an area e.g. a tumor, thus creating a spread-out Bragg peak (SOBP). This is done by using multiple fine-tuned beam-energies in the same beam to stack the single Bragg peaks together (Paganetti, 2011). Applying this principle, there are two proton-beam delivery methods

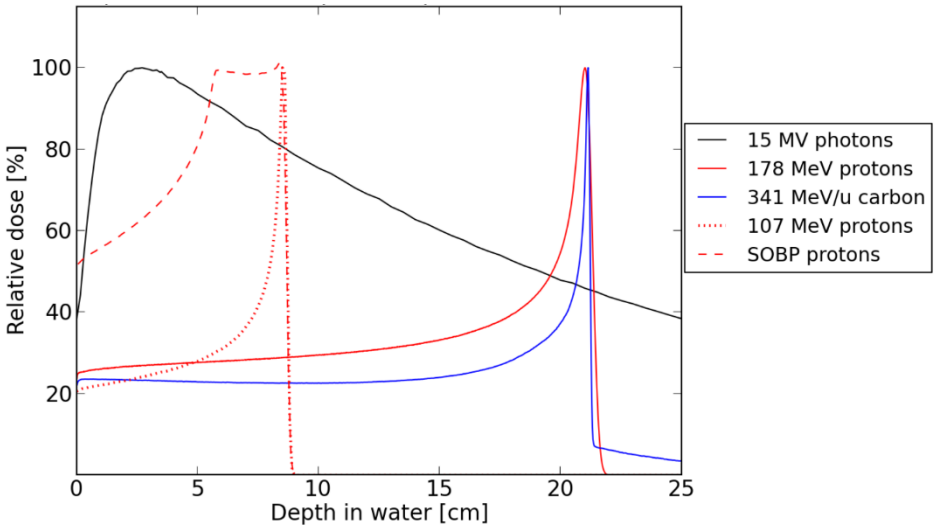

Figure 1-1: The depth dose curves for photons, protons and carbon ions. The protons and carbons deposit a large fraction of the dose deep into the medium, while the photons have a maximum dose deposition a few centimeters into the medium. The dashed red line shows a proton SOBP. Also notice the sharper carbon Bragg peak, in addition to the fragmentation tail (Ytre-Hauge, 2013).

available: Passive scattering and active scanning. Passive spreading is the first and most commonly used method in proton therapy as of 2006 (Schulz-Ertner et al., 2006), using different modulators, plates, wedges, etc. to shape the beam according to the tumor. Active beam scanning takes advantage of the electric charge, using magnets to bend the beam to allow scanning over the treatment area (Schulz-Ertner et al., 2006). These will be explained in greater detail in chapter 2. Independent of the method, the aim is to distribute Bragg peaks in such a way that the SOBP peak is covering the entire tumor.

While the physical properties of the proton beam are well known, there are still great uncertainties regarding the biological effects. Unlike for photons, there are not much clinical data and statistics yet in terms of these effects for particle therapy. Thus, to estimate the treatment iso-effects of protons, one uses the biological effects of photons with a factor. This is in most cases expressed as the relative biological effectiveness (RBE), where the biological effect of protons is compared to the biological effect of x-rays, or gamma-rays such as ^{60}Co radiation. The RBE is used when calculating the proton dose, which will be explained in chapter 2. Most proton facilities assume protons to be a constant factor of 10% more effective than the gammas (Wilkens & Oelfke, 2004), equivalent to RBE = 1.1 ($RBE_{1.1}$) as seen in the example in figure 1-2. This however is a simplification, as experimental evidence show that the RBE is not constant, but depends on variables such as the physical variables of the linear energy transfer (LET), i.e. the energy deposited by the passing proton per unit length, and the dose (Wilkens & Oelfke, 2004). This is particularly apparent for in vitro experiments, using cell cultures (Belli et al., 2009). However, for in vivo experiments, the observed variations in RBE is much less apparent and in many cases a constant RBE equal to 1.1 is clinically acceptable for most of the SOBP (Paganetti et al., 2002). There is however, still is a distinct increase in the RBE at the

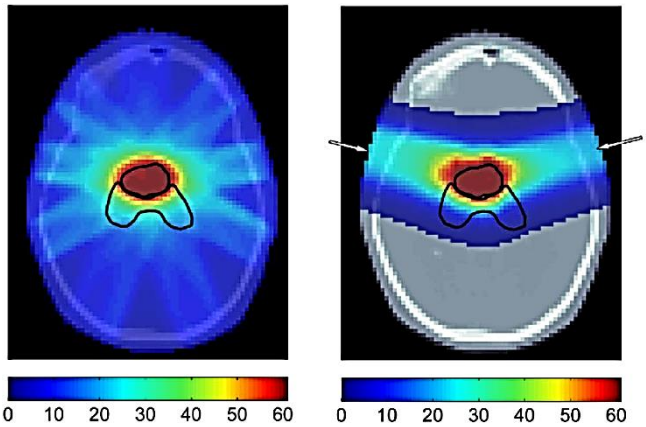

Figure 1-2: The left panel shows the dose distribution of the total dose (Gy) for the photon plan, and the right panel shows the $RBE_{1.1}$-weighted dose distribution for the proton plans (Wedenberg, 2014).

end of the proton beam range (Gueulette et al., 1997) that should be accounted for when planning and treating using protons in proton therapy (Paganetti et al., 2002). The effect of this increase will also be looked at in this project, when applying variable RBE and comparing the result with that of constant RBE.

In order to calculate a variable RBE from in vitro experiments, a number of variables that reflect differences in radiation sensitivity as well as physical properties of the protons are normally used. For differences in radio-sensitivity, so called alpha- and beta values, commonly derived from the cell survival curve which can be read about in chapter 2, are frequently used. Different models will calculate these variables differently and thus get different RBE values (Wilkens & Oelfke, 2004). Chapter 3 will review the models used in this project and can be read to learn more about these differences.

1.3 Monte Carlo simulation

To plan and deliver the dose correctly to the patient and tumor, a treatment planning system (TPS) is required. The planning system's purpose is to plan a treatment (beams, angles, etc.) such that the treatment machine delivers the prescribed dose to the tumor, while sparing as much health tissue as possible.

Today TPSs usually rely on pencil beam (PB) algorithms to calculate the doses, which compromises between accuracy and computation time (Li, 2009). Several PB algorithms have high uncertainties in calculations of low-dose regions, in highly heterogeneous tissues or if metallic materials are present. This is where Monte Carlo (MC) calculations can provide superior accuracy (Bauer et al., 2014; Stathakis et al., 2016; Yamashita, Akagi, Aso, Kimura, & Sasaki, 2012). One way to increase the accuracy of the dose calculations as well as to better understand the beam characteristics is to have simulations accompany the treatment planning system (Polster et al., 2015).

The time it takes often depends of the complexity of the problem or its geometry and therefore deterministic methods will often be used for so-called model-problems. Model problems are simplified, such that it will give an approximate answer within a reasonable timespan. In reality on the other hand, using a deterministic method can be very time-consuming or not accurate enough and stochastic methods using Monte Carlo (MC) simulations can be favorable (Bielajew, 2013). Figure 1-3 visualizes this neatly. Stochastic sampling methods were known before the age of computers. The first known reference to such a method is that of Comte de Buffon back in 1777 (Comte de Buffon, 1777; Dunn & Shultis, 2011). Other uses of MC predating computes are cited by Kalos and Whitlock (Kalos & Whitlock, 2008). The modern MC age started when stochastic methods were applied to radiation transport calculation, in a documentation dated Mar. 1947 by Neumann and Richtmyer (Eckhardt, 1987).

MC techniques, in the case of radiation therapy, is based on guided trial and error using objects such as particles [photons, protons, electrons, neutrons, charged nuclei, etc.] which interact with another object/objects in a way based on their interaction cross sections. The process, such as to shoot a particle at a target, is then repeated randomly by varying energies, angles, etc., until the results converge to their estimated values. MC attempts to model nature directly using this random/dynamic method, within a simple system (Bielajew, 2013).

The FLUKA code is a general purpose MC code simulating the transport and interaction of different particles and is developed by the European Organization for Nuclear Research (CERN) and the Italian Institute for Nuclear Physics (INFN) (Böhlen et al., 2014; Ferrari, Sala, Fasso, & Ranft, 2005). In this thesis, the FLUKA code will be used to simulate the physical interactions of protons in water, as well as in human tissue.

1.4 Project objective

The objective of this thesis was to calculate biological doses for a clinical patient case using multiple RBE models for protons applied together with the FLUKA MC code, and further compare these results with doses from the assumption of a constant RBE of 1.1, as used in current clinical practice. In addition, MC simulations were also being performed on water phantom geometries to further investigate the properties of the different RBE models and to evaluate the variation in biological dose predicted by the models in a simplified setup.

All FLUKA simulation data in this thesis are produced by the author, unless specified.

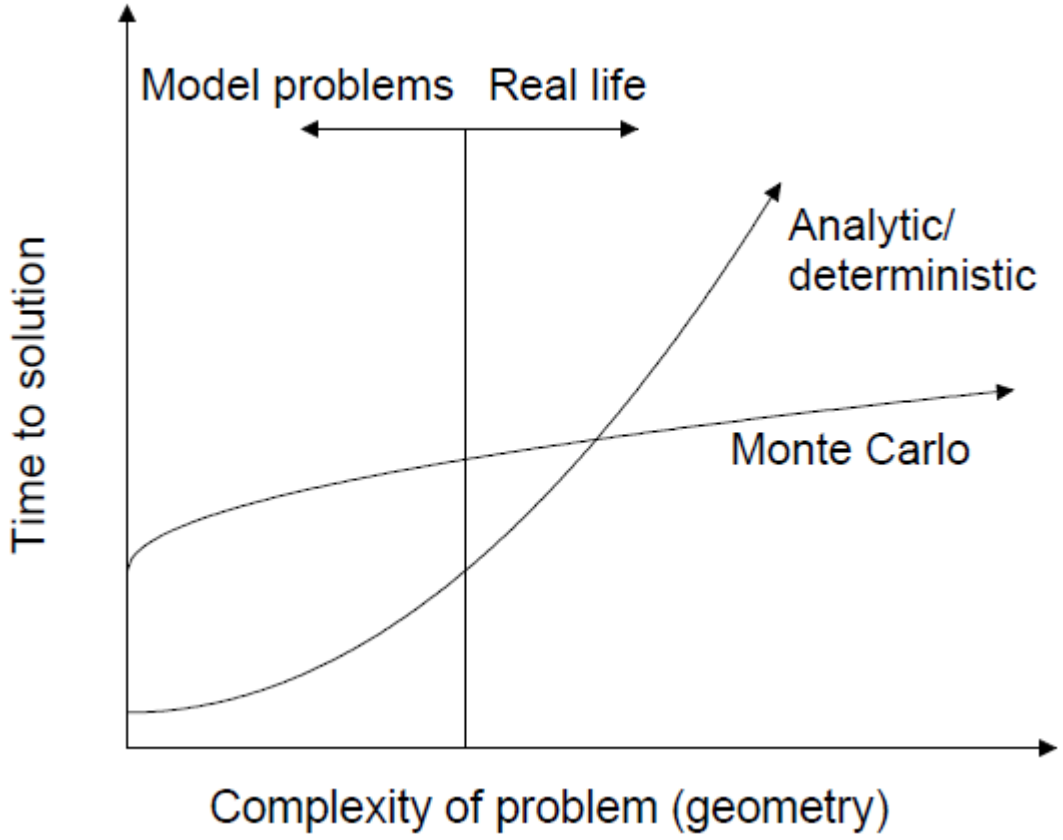

Figure 1-3: Time to solution using Monte Carlo vs. deterministic/analytic approaches. One can observe that while deterministic methods work in theory and modelled scenarios, when it comes to more realistic and complex problems, Monte Carlo methods become superior in terms of time(Bielajew, 2013).

2 Proton Therapy

This section is dedicated to the most relevant theory in regards to proton therapy. In addition, there will be a section at the end dedicated to treatment delivery.

2.1 Particle Interaction in Matter

When charged particles traverse through a material they usually interact though ionization and excitation of the material. Protons are called “heavy” charged particles. Particles are termed heavy when its rest mass is large compared to the rest mass of the electron.

2.1.1 Multiple Coulomb scattering

Heavy charged particles traveling through a material will not traverse in a completely straight line. Each particle will experience many elastic scatterings in small angles. Every interaction results in an energy loss and a deflection. These losses and deflections add up statistically. The scatterings are mostly due to each particle’s electric charge interacting with material nuclei via the Coulomb force. After passing through the material, the beam will have an increased lateral spread, which is inverse proportional to the mass of the particle and the particle velocity, and proportional to the charge of the particle. For a single particle, figure 2-1 visualizes the expected path (Henley & Garcia, 2012; Meroli, 2012).

The number of particles absorbed in the material depends on the material thickness and density relative to the incident particle energy. Up to a certain thickness, it is likely that all particles will be transmitted, while at a sufficiently large thickness, all particles will be absorbed. This makes it very important to have enough particles during a MC simulation, as the number of particles left after a certain length can become very few and increase the uncertainty. In the case of radiation therapy, it is desirable that most particles are absorbed in the tumor to give the highest possible tumor dose. Due to the energy depositions of heavy charged particles, they will release the most energy as they come to a halt, as will be explained in section 2.1.2 (Henley & Garcia, 2012). Figure 2-2 illustrates this, together with a typical beam spread for both protons and carbon-ions (Ytre-Hauge, 2013).

2.1.2 Losses by ionization and excitation

Protons, when traveling through the patient, will lose their energy mainly through elastic collisions with bound electrons. When colliding, the bound electrons are then either lifted to higher energy levels (excitation) or completely ejected from the atom (ionization) (Henley & Garcia, 2012).

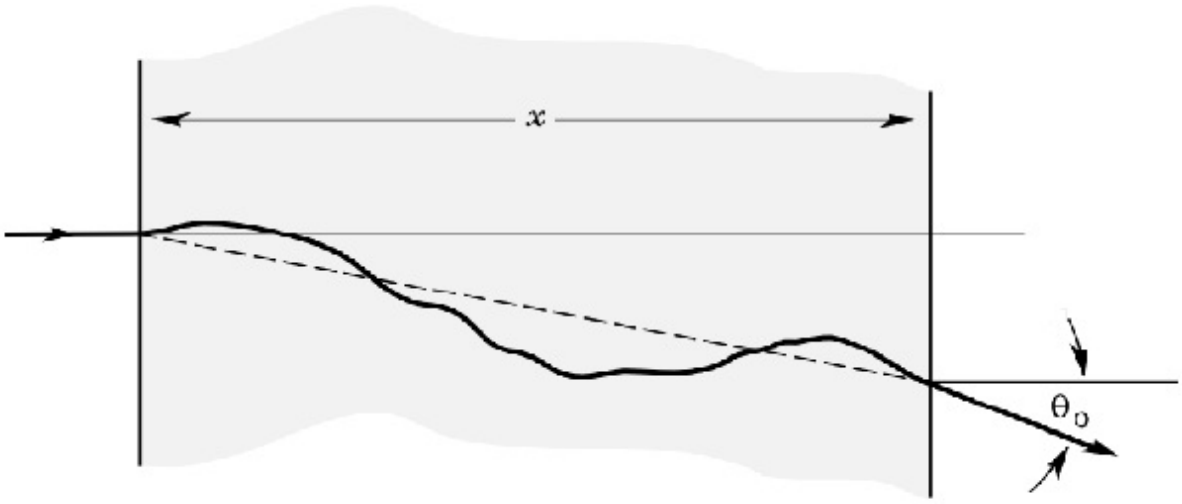

Figure 2-1: Effect of Multiple Coulomb Scattering (Meroli, 2012).

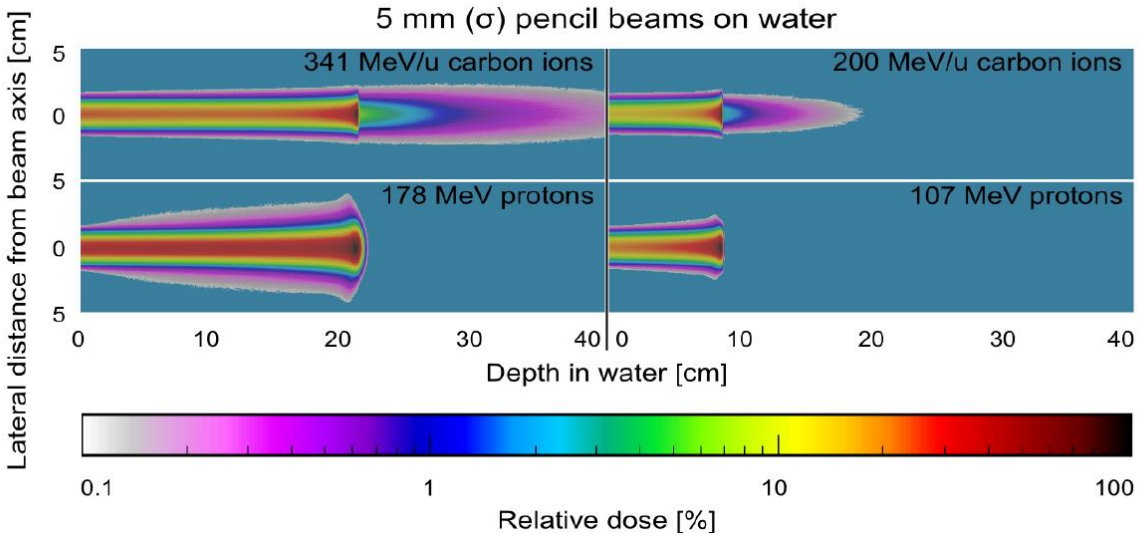

Figure 2-2: Lateral spread for proton- and carbon beams as a function of depth in water. The protons have a three times larger broadening than the carbon ions for the highest energies depicted on the left. The dose tail, as a result of fragmentation of the carbon ions, can also be seen (Ytre-Hauge, 2013).

The energy loss $(-dE)$ per unit length (dx) due to interactions with matter is called the stopping power and has been derived quantum mechanically by Bethe (Bethe & Ashkin, 1953). Relevant initial beam energies for particle therapy are typically below $220\ MeV/u$ for protons (Schardt, Elsässer, & Schulz-Ertner, 2010). In this energy range the stopping power can be quantified though modelling of elastic collisions with atomic electrons. The required equation is called the Bethe-Bloch formula. The relativistic expression is (Bethe & Ashkin, 1953; Fano, 1963; Khan & Gibbons, 2014):

$$-\frac{dE}{dx} = \frac{4\pi e^4 Z_p^2 Z_t^2}{m_e v^2}\left[\ln\frac{2m_e v^2}{\langle I\rangle} - \ln(1-\beta^2) - \beta^2 - \frac{C}{Z_t} - \frac{\delta}{2}\right]. \tag{2.1}$$

Relevant variables used in the Bethe-Block formula can be found in table 2-A. The Bethe-Bloch equation states that the stopping power is inversely proportional to the particle velocity and thus the energy loss increases as the particle comes to a halt (Bragg & Kleeman, 1904). This results in a distribution of dose where most is deposited towards the end of the path and is what is called the Bragg-peak, which is explained further in section 2.1.5.

Table 2-A: Relevant variables for the Bethe-Block formula

Symbol	Definition	Unit
e	Electron charge	*1.6e-19 C*
Z_p	Projectile charge	e
Z_t	Target charge	e
m_e	Electron mass	MeV/c
v	Projectile velocity	m/s
I	Mean excitation potential	eV
β	Relative particle velocity to speed of light	v/c
C	Shell correction	
δ	Density effect correction	

2.1.3 Inelastic nuclear interactions

In addition to the more common excitation and ionization interactions, there are also nuclear interactions, which can give dose contributions in the relevant energy range used in therapeutic instances. Figure 2-3 shows the absorbed dose as a function of depth in a water phantom for a 160 MeV proton beam. Nuclear interactions occur when the incoming protons interact with the target nucleus by knocking out other protons, neutrons or ion clusters such as alpha particles. These are called secondary particles and will usually have much lower energy then the incident particle. The secondary particles will contribute to the dose during therapy and if the secondary particle is neutral, such as a neutron, it will travel further, possibly depositing dose outside the planned target volume. Due to the directional momentum carried by the high velocity primary proton particles, the additional dose by these secondary particles will be deposited after the normal range of the primary beam (Kaderka et al., 2012).

2.1.4 Energy to range relation

Statistical fluctuations make it difficult to set a definitive range for each particle. The nature of the interactions causing energy-loss and the number of interactions required to put a particle to rest will vary slightly, causing statistical variations to the range. The phenomenon is called

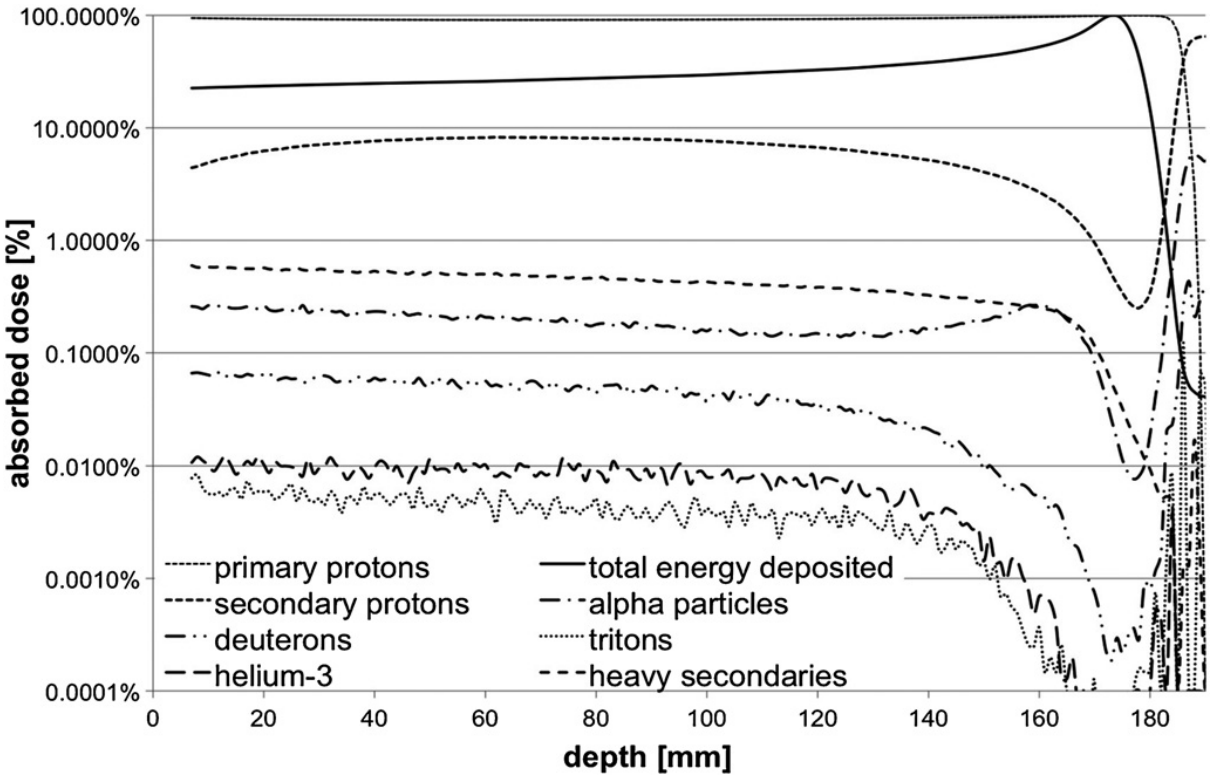

Figure 2-3: Absorbed dose as a function of depth of a 160 MeV pristine peak in a water phantom. The absorbed dose is shown as percentage of the maximum absorbed dose and the individual components are shown as percentage of absorbed dose at that depth (Grassberger & Paganetti, 2011).

range straggling (Gottschalk, 2012; Grupen & Shwartz, 2008). A formula applying the Continuous Slowing Down Approximation (CSDA), used to estimate the range is defined as:

$$R = \int_{E}^{0} \frac{1}{\frac{dE}{dx}} dE. \tag{2.2}$$

The formula integrates the stopping power from equation 2.1 above, over the entire energy range from the maximum energy E until full energy loss (Grupen & Shwartz, 2008).

2.1.5 The Bragg peak

As mentioned at the end of section 2.1.2, since the stopping power (eq. 2.1) is inversely proportional to the velocity of the proton, the dose deposition increases as the particle energy is recued. This results in a region of maximum energy loss at the end of the range, commonly referred to as Bragg-peak (Bragg & Kleeman, 1904; Paganetti, 2011).

A typical Bragg-peak for protons can be seen in figure 2-4a. As explained in section 2.1.4, some particles traverse slightly further than the peak, due to range straggling. This effect can be

observed in figure 2-4a where the dose doesn't drop to zero immediately, showing the deposition of the leftover particles (Paganetti, 2011).

The example in figure 2-4a displays a single beam example. In clinical situations however, the proton beam needs to cover an entire volume with the prescribed dose. This is done by using multiple beams with fine-selected energies that, when stacked together, form a plateau, as visualized in figure 2-4b. As mentioned in the introduction, the Bragg-peak and SOBP gives protons an advantage over photons and electrons (Jones et al., 2011; Paganetti, 2011). One can compare the percent depth-dose (PDD) of the SOBP in figure 2-4b with the typical PDD of electron- and photon beams shown in figure 2-5a and figure 2-5b. In short the SOBP has a great advantage at lower dose depositions in the entrance region and after the target region for a given beam angle.

2.2 Dosimetry and Radiobiology

2.2.1 Absorbed dose

From the proton energy loss, the amount of ionization radiation absorbed by the medium over a given mass is referred to as absorbed dose, or simply dose. It is measured in Gray [Gy] which is defined as the absorption of 1 joule of radiation energy per kilogram of tissue. The International Commission on Radiation Units (ICRU) defines the absorbed dose as the mean energy imparted ionizing radiation to a certain mass (ICRU, 1998):

$$D = \frac{\Delta E}{\Delta m}, \tag{2.3}$$

where, D being the absorbed dose, ΔE the mean energy absorbed and Δm the mass the energy is absorbed by. This dose is then often modified to account for treatment delivery and biological effects, such as dose weighted with the relative biological effectiveness, with will be explained in section 2.2.4. It is important to note that the absorbed energy is not necessarily equal to the energy lost by the particles in the proton beam, i.e. the stopping power (section 2.1.2). This is because energy can be deposited outside the target volume though different secondary particles such as neutrons or photons (ICRU, 1998; Paganetti, 2011).

Figure 2-4: Typical Bragg-peak and SOBP for a proton beam

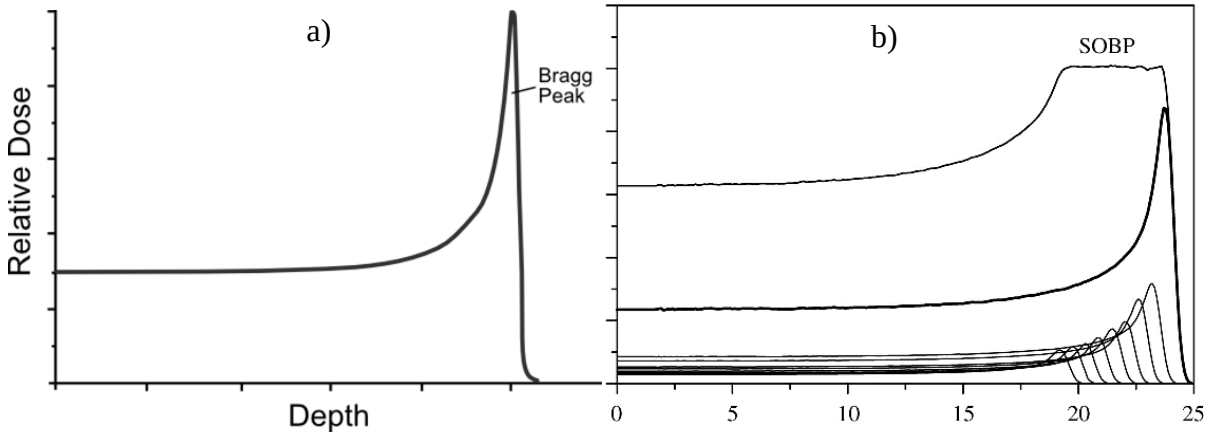

Figure 2-4: a) Graph of radiation dose with respect to depth into tissue for a proton beam (Oxford, 2015). b) Illustration of a typical spread-out Bragg-peak for a clinical proton beam. The beam consists of multiple individual beams with different specific energies in order to create an plateau of even dose distribution over the target volume (ICRU, 2014).

Figure 2-5: Typical depth-dose curves for electron and photon beams

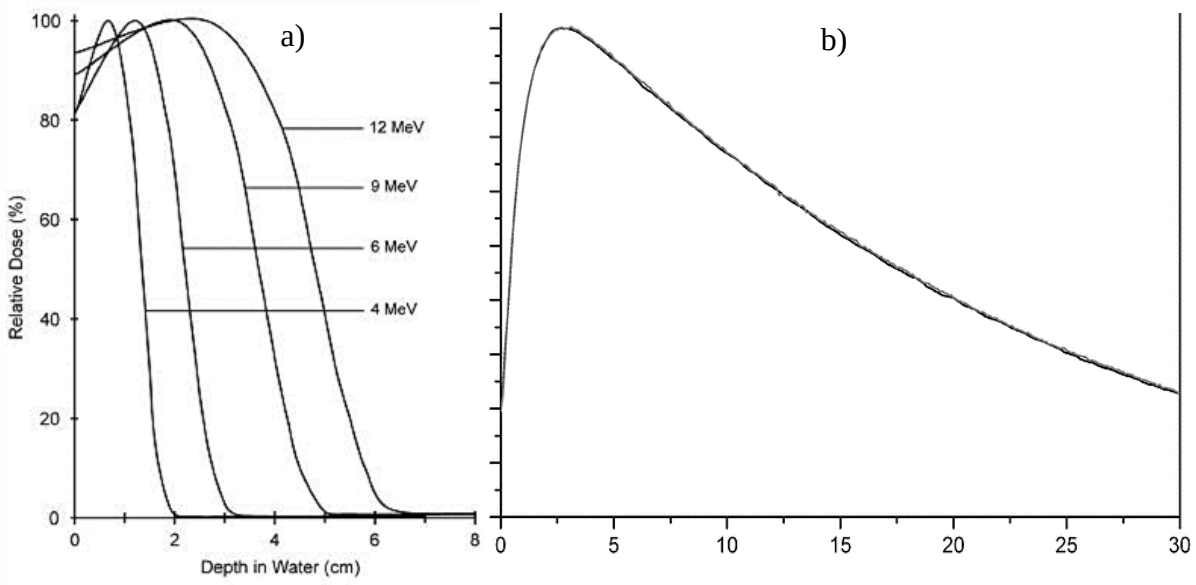

Figure 2-5: a) Depth-dose curves for 4-MeV, 6-MeV, 9-MeV, and 12-MeV electron beams for a 10-cm diameter applicator (Sam Beddar & Krishnan, 2005). b) Percent depth-dose curve of a 10 x 10 cm^2 field size 15 MV photon beam in a linac without the µMLC (Multi-leaf collimator) (Fischer, Todorovic, Drud, & Cremers, 2010).

2.2.2 Cell killing and cell survival

In radiation therapy the objective is to kill cancerous cells, while attempting to spare healthy tissue. For a proliferating cell to be considered “dead”, it must be unable to reproduce, and the most sensitive part of a cell is its DNA (Borges, Linden, & Wang, 2008).

Radiation can damage the DNA molecules in two different ways, called direct- and indirect action. In indirect action, the particles of the beam interact with the water molecules in the cell causing free radicals such as hydroxyl (OH-) to be created (Hall, 2009). Free radicals are extremely reactive and can, following a chain of reactions, turn into hydrogen peroxide (H_2O_2). This can then cause molecular structural damage to the DNA strands. Due to the high amount of water in a cell (about 70%), a substantial damage to the DNA will be caused by the indirect action mechanism (Kelley, 2011). In direct action, particles from the beam or secondary particles ionized by the beam such as electrons, ionizes atoms in the DNA stand causing them to break. This type of radiation will often cause double-strand breaks, in which case, both strands of the DNA is damaged. Direct action becomes predominant with high ionization density (LET, see section 2.2.3) such as for protons. Double-strand breaks are also much harder for the cell to repair and thus much more like to lead to DNA aberrations which in turn can cause cell death (Saha, 2012). An illustration of the two interactions can be found below in figure 2-6.

Cell irradiation experiments has been extensively used to quantify the cell survival as a function of dose. In radiotherapy the most commonly applied model is the linear-quadratic model (Lea, 1946). The survival curve is fitted by an exponential function for cell survival fraction as a function of the absorbed dose:

$$SF = \exp(-\alpha D - \beta D^2)\,. \tag{2.4}$$

The α and β values determine the shape of the curve with one linear and one quadratic component. These are so called single track events (one hit cell killing) and two track events (repairable, needs more than one hit), respectively. Different tissues will have different α/β ratios, which characterizes their fractionation sensitivity. These ratios are very useful when optimizing fractionation (dose fractions) in radiotherapy, where the total dose is split into smaller segments (Joiner & van der Kogel, 2009). Low α/β values indicate that the tissue is sensitive to change in fractionation, while for high α/β ratios fractionation has a smaller effect.

2.2.3 Linear energy transfer

As explained in 2.2.2, direct action interactions are more likely with increasing ionization density, i.e. the amount of ionizations per unit length. This is referred to as the linear energy transfer (LET). It is the average energy imparted to the medium as the particle travels a certain distance, usually in keV/µm (Joiner & van der Kogel, 2009). In general, an increase of LET leads to a higher cell kill per dose, regardless of radiation type up to a certain point. In other words, the steepness of the survival fraction curve increases with increasing LET, as well as becoming straighter, meaning that α increases and β decreases (Joiner & van der Kogel, 2009). Protons have a higher LET at lower kinetic energies compared to photons. Thus, there are more

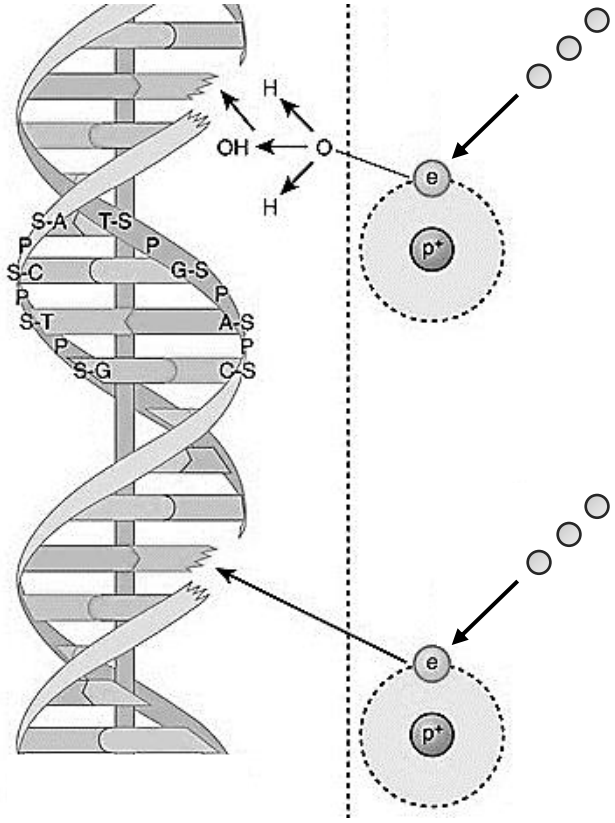

Figure 2-6: Indirect action (top of figure), the secondary electron interacts with a water molecule to produce a hydroxyl radical that then damages the DNA. Direct action (bottom of figure), the secondary electron interacts directly with the DNA. Modified from (Hall, 2009).

secondary particles produced, increasing the chance of double-strand breaks and cell killing (Joiner & van der Kogel, 2009). The concept of LET_D is used then relative dose is used as a weighting factor to calculate the averaged LET (Guan et al., 2015). LET_D is used in the RBE calculations.

2.2.4 Relative biological effectiveness

It is important when determining what kind of radiation to use, that the dose can be compared to that of other radiation types. This can be done using relative biological effectiveness (RBE). The RBE of a radiation beam being tested and biological dose [Gy(RBE)] are defined with the formulas:

$$RBE_{iso-effect} = \frac{dose\ of\ reference\ radiation}{dose\ of\ test\ radiation} \tag{2.5}$$

$$Biological\ dose = Physical\ dose * RBE \tag{2.6}$$

The RBE defines how much dose of the test radiation would be needed to acquire the same biological effect as that from a given dose of the reference radiation. The reference radiation is commonly 250 kVp (peak kilo voltage) X-rays or ^{60}Co gamma-rays since these radiations are well known and available when RBE is to be evaluated (Joiner & van der Kogel, 2009). In clinical practice, proton therapy is given with the assumption of a constant RBE value of 1.1. The value is based on cell and animal (in vivo) experiments (Paganetti, 2015). However, several experimental studies show that the RBE varies depending on a variety of variables such as particle energy, LET and the reference radiation ratio (Wilkens & Oelfke, 2004). The RBE will increase as LET increases, until a maximum RBE is reached and then decrease. An example of this can be observed in figure 2-7. According to a study, the optimal LET for the maximum RBE for protons roughly 30 keV/µm (Belli et al., 1997). At the optimal LET, the RBE will vary depending on the survival fraction (SF in the figure). Beyond the optimal LET, the cell killing becomes less effected due to the phenomenon called "overkilling". Overkilling occur when the radiation deposits more energy to the cell and DNA than required to kill the cell. This waste of energy means the process becomes less effective per unit dose (Paganetti, 2011).

2.3 Treatment delivery

In order to deliver the dose to the entire tumor and target volume uniformly, like a SOBP, the particles must be spread in lateral, axial and longitudinal directions. To do this there are two common delivery techniques used in particle therapy. They are called passive beam shaping (passive scattering) and active beam scanning (pencil beam scanning) (Schulz-Ertner et al., 2006). Figure 2-8a shows the design of a passive beam shaping delivery system.

Active beam shaping utilize magnets to steer the charged particles of the beam towards the target. The steering magnets consists of two dipoles, one for vertical and one for horizontal steering. Since the beam is still narrow and not scattered like in passive shaping, it is instead steered across the PTV, voxel by voxel and layer by layer. This can be seen in figure 2-8b below. The first layer is the farthermost from the beam source and is reached with the maximum particle energy of the beam. Once the first layer and all of its voxels has been covered, the particle energy is reduced to irradiate the next layer and so on (Grupen & Buvat, 2011). The voxels may be irradiated continuously using raster-scanning, i.e. the beam is always on, and is steered continuously by the dipoles. Else, the voxels may be irradiated one at a time using discrete spot scanning, where the beam is turned off between each voxel (Schippers, 2009).

Compared to passive shaping the active shaping achieves higher dose conformity and thus sparing more of the health tissue. This is due to the passive technique shifting the SOBP towards the entrance region of the PTV, where normal tissue is located. In addition, due to the amount of material in the beam line, there will be a considerable increase in nuclear fragments. The lower energies of these fragments also lead to a higher LET, which in turn will lead to an increased dose deposited in the normal tissue in front of the PTV. However the scanning takes more optimization, as the SOBP is optimized separately for each voxel in the field (Schulz-Ertner et al., 2006).

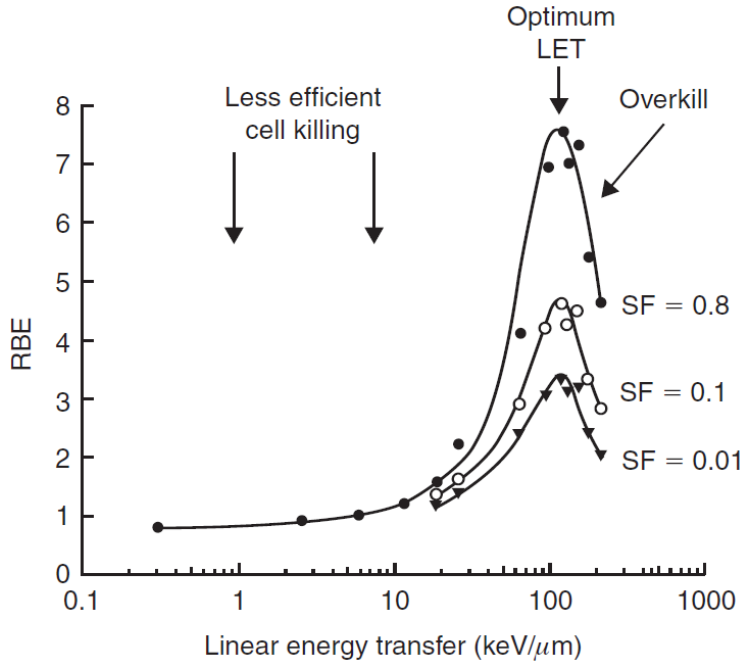

Figure 2-7: Dependence of relative biological effectiveness (RBE) on linear energy transfer (LET) and the phenomenon of overkill by very high LET radiations. The RBE has been calculated from Fig. 6.2 at cell surviving fraction (SF) levels of 0.8, 0.1 and 0.01 (Barendsen, 1968; Joiner & van der Kogel, 2009).

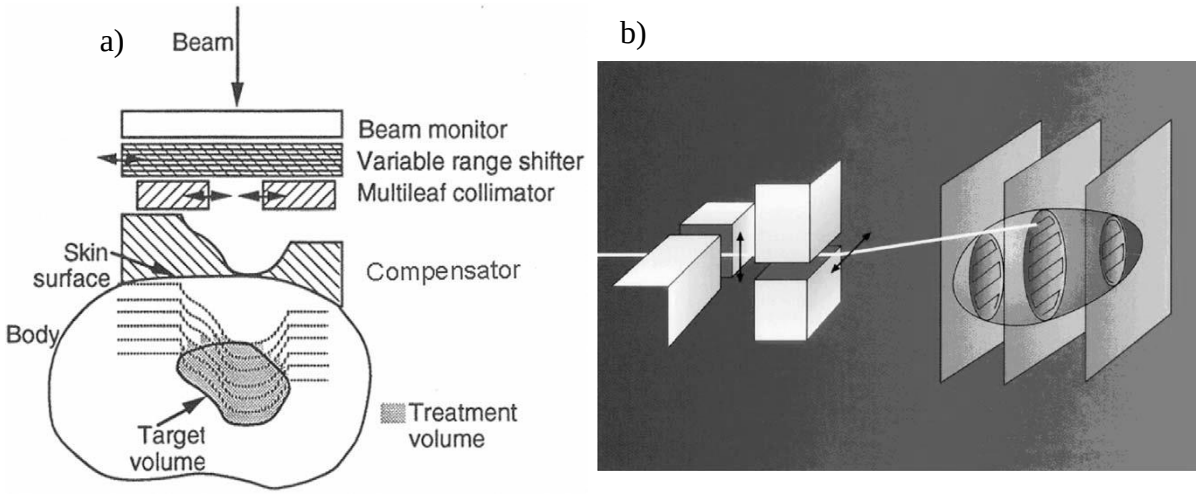

Figure 2-8: a) Principle of the passive dose-delivery system used for charged particle therapy. Shown is the incoming broadened beam. The variable range shifter has to shift the depth dose to the desired depth, whereas the compensator and collimator are patient-specific devices and adapt the dose distribution to the size and distal shape of the target volume. The lines in the body represent the distal falloff that can be shifted in depth with the range shifter (Schulz-Ertner, Jäkel, & Schlegel, 2006). b) Principle of the active raster scan system used at GSI for carbon ions. A small pencil beam is scanned in vertical and horizontal direction by using 2 pairs of scanner magnets. By switching the energy of the synchrotron, the position of the Bragg peak can be chosen so that each scanned area is adapted to the extent of the target in depth (Schulz-Ertner et al., 2006).

3 RBE models

3.1 Wilkens model (WIL)

Wilkens and Oelfke proposed a model for the RBE to be used in therapeutic scenarios using proton beams. It was made in order to study the effects of variable RBE in inverse treatment planning, where fast methods of calculation would be required (Wilkens & Oelfke, 2004).

In order to acquire the RBE, equation 2. (section 2.2.4) must be written in such a way that the RBE will depend on dose, tissue and two different radiations: a proton beam and a reference radiation (Wilkens & Oelfke, 2004). Since the RBE is simply defined as the difference in doses needed to have the same survival of cells, it is based on the surviving fraction (SF) and the LQ model (Kellerer & Rossi, 1978). Though the following formula can be written in many different ways and thus may look slightly different depending on which article you read, the formulas should be equivalent (Dale & Jones, 1999; Hawkins, 1998; Joiner & Field, 1988). One way to write the formula, which Wilkens and Oelfke used, is:

$$RBE\left(D_p, \alpha_x, \beta_x, \alpha_p, \beta_p\right) = \frac{\sqrt{\alpha_x^2 + 4\beta_x D_p\left(\alpha_p + \beta_p D_p\right)} - \alpha_x}{2\beta_x D_p}. \tag{3.1}$$

Here, D_p is the dose of protons, while α_x/β_x (reference radiation) and α_p/β_p (proton radiation) are parameters used to characterize the tissue and biological system. The parameters can be used to draw the survival curves for the same biological system using the LQ model.

The reason why the RBE is not constant is due to the values of α_p/β_p not being constant, since they depend on the LET of the proton beam. As was explained throughout section 2.1, the energy deposition per unit length, or LET, varies as the protons traverse through the tissue. Figure 3-1a shows data points from many different experiments on the survival of V79 cells (in vitro) with proton beams. The data is the α_p parameter as a function of LET_D (dose averaged LET) up to roughly 30 keV/µm which is within the practical LET range of proton therapy. Looking at the low LET region, Wilkens and Oelfke assumes, with linear regression, a linear dependence of the α_p parameter on the LET_D:

$$\alpha_p(L) = \alpha_0 + \lambda L. \tag{3.2}$$

Here L is the LET_D, while α_0 and λ are fit parameters. When looking at the data in figure 3-1 for the V79 cells, Wilkens and Oelfke found the best fit was obtained when $\alpha_0 = 0.1\ Gy^{-1}$ and $\lambda = 0.02\ \mu m\ keV^{-1}\ Gy^{-1}$ (Wilkens & Oelfke, 2004).

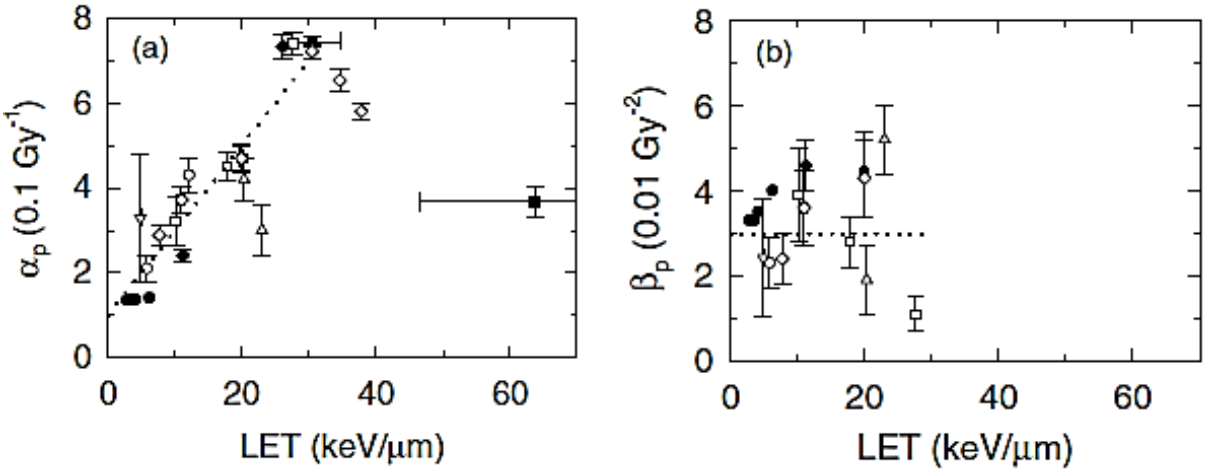

Figure 3-1: Data and results for the LQ parameters for the survival of V79 cells, in vitro: (a) α_p versus LET_D; (b) β_p versus LET_D (○ (Perris, Pialoglou, Katsanos, & Sideris, 1986); ∆ (Goodhead et al., 1992); ∇ (Blomquist et al., 1993); ■ (Belli et al., 1993); (Folkard et al., 1996); ● (Wouters et al., 1996); ◇(Belli et al., 1998); ◆(Schettino et al., 2001)). Figure by (Wilkens & Oelfke, 2004).

The β_p parameter, shown in figure 3-1b, is not as clear as the α_p parameter. Depending on the study, some found an increasing β_p (Belli et al., 1998), while some reported decreasing values (Folkard et al., 1996). Wilkens and Oelfke decided to assume a constant β_p, which they set equal to the reference radiation β_x, i.e.:

$$\beta_p(L) = \beta_x. \tag{3.3}$$

As mentioned in section 2.2.4, the reference radiation when calculating RBE is often either 200/250 kVp X-rays or cobalt 60 gamma-rays. For their model, Wilkens and Oelfke chose cobalt 60, which for V79 cells, means using $\alpha_x = 0.112\ Gy^{-1}$ and $\beta_x = 0.0298\ Gy^{-2}$ (Tilly, Brahme, Carlsson, & Glimelius, 1999). Upon discussion, the model fits with measurements within experimental uncertainties, but with some limitations. The model overshoots the experimental values slightly when LET is above 15 keV/µm. In terms of LET it only accounts for primary and secondary protons. The model was also derived from the survival of V79 cells (in vitro) (Wilkens & Oelfke, 2004). Figure 3-2 shows the calculated RBE for different LET values.

3.2 Wedenberg model (WED)

Wedenberg, Lind and Hårdemark proposed a model for the RBE of protons, where the aim for the model was to "capture the basic features of the RBE using a minimum of assumptions, each supported by experimental data" (Wedenberg et al., 2013).

Similar to Wilkens et. al. (section 3.1) Wedenberg et. al. observed the increase of the α parameter up to 30 keV/µm, after which it decreases (Belli et al., 1998). Likewise, Wedenberg et. al. chose to not account for this decrease, since that high LET_D values are of little practical

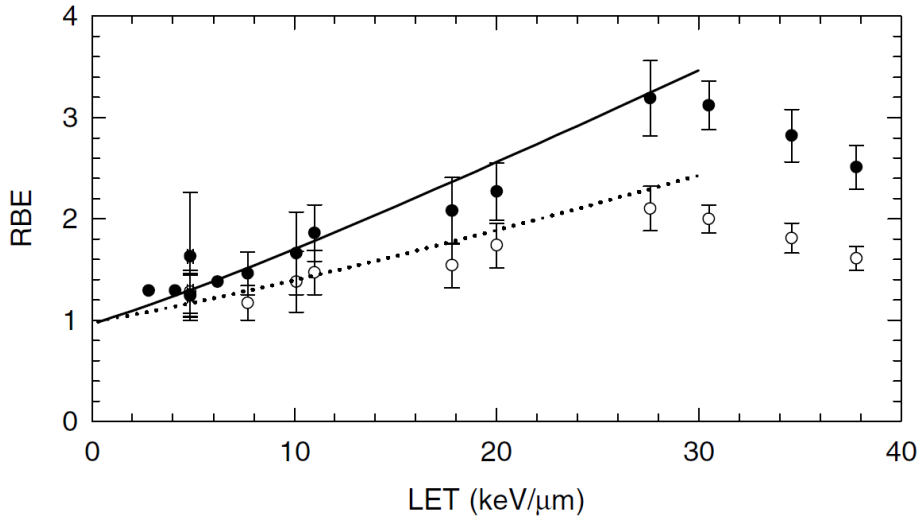

Figure 3-2: RBE values for different LET values. The experimental data for two survival levels (◦10%, •50%) are from (Blomquist et al., 1993), (Folkard et al., 1996), (Wouters et al., 1996) and (Belli et al., 1998). RBE values that were reported relative to 200 kVp (Belli et al., 1998) or 240 kVp X-rays (Folkard et al., 1996) were corrected to ^{60}Co by applying a dose independent factor of 1.1 (Spadinger & Palcic, 1992). Figure by (Wilkens & Oelfke, 2004).

relevance compared to the energy used in clinical proton therapy (Wedenberg et al., 2013). Different α parameters are reported from different studies, possibly because they use different cell lines. Wedenberg et. al therefore assume that the parameter is dependent on the cell type and propose an inverse relationship between α and the tissue related parameter $(\alpha/\beta)_x$. The resulting expression is:

$$\frac{\alpha}{\alpha_x} = 1 + \frac{qL}{(\alpha/\beta)_x}. \tag{3.4}$$

Here α_x is the photon parameter, L is LET_D and q is a free parameter (Wedenberg et al., 2013). Wedenberg et. al. concluded similarly to Wilkens et. al. that the correlation between β and LET is not as strong as that for the α parameter. Therefore, they assume:

$$\frac{\beta}{\beta_x} = 1. \tag{3.5}$$

The model was tested with many different cell lines including V79 cells. Depending on the $(\alpha/\beta)_x$ of the cell line, the slope of the α/α_x vs. LET_D would increase. Table 3-A lists the different data grouped together based on the cell type, resulting in a slope $k = \frac{q}{(\alpha/\beta)_x}$ (Wedenberg et al., 2013). The resulting curves are shown in figure 3-3.

Table 3-A: Resulting slope for different cell lines

$(\alpha/\beta)_x$ [Gy] **(Cell line)**	k [$keV/\mu m$]$^{-1}$
2.7-3.1 (V79-379A, V79-753B, DLD1)[1]	0.14-0.16
7.7-7.7 (SQ20B, C1-1)[2]	0.057-0.057
15-18 (C3H10T1/2, SCC25)[3]	0.024-0.029
70-∞ (HCT116, M/10, HF19)[4]	0-0.0060

Wedenberg et. al. found the free parameter q of eq. 3.4 to be $0.434\ Gy\ \mu m/keV$. This is also included in the k value in table 3-A and figure 3-3. Upon discussion, Wedenberg et. al. saw the relation between α/α_x and LET_D that they had hypothesized. However, this was mostly from the low $(\alpha/\beta)_x$ cell lines, while those with $(\alpha/\beta)_x \geq 15$ showed no statistically significant relation. The expression (eq. 3.4) sees an increasing α/α_x with increasing LET_D with a slope that decreases with increasing $(\alpha/\beta)_x$. An advantage of the approach Wedenberg et. al used is that the model fits to a range of different cell lines and LET_D values, instead of just a single cell line and radiation (Wedenberg et al., 2013). Figure 3-4 shows the calculated RBE for different LET_D values.

3.3 Carabe model (CAR)

Carabe-Fernandez, Dale and Jones proposed a RBE model for high-LET via the RBE_{max} and RBE_{min} concepts. These represents the high and lower limits of the RBE, seen at a dose per fraction approaching zero and infinite respectively. The model used in this study is the extension by Carabe-Fernandez et al. (Carabe-Fernandez, Dale, & Jones, 2007) of the approach proposed by Dale and Jones (Carabe, Moteabbed, Depauw, Schuemann, & Paganetti, 2012; Dale & Jones, 1999; Giovannini et al., 2016).

The RBE_{max} and RBE_{min} concepts are defined as:

$$RBE_{max} = \frac{\alpha}{\alpha_x} \tag{3.6}$$

$$RBE_{min} = \sqrt{\frac{\beta}{\beta_x}}. \tag{3.7}$$

[1] (Baggio et al., 2002; Belli et al., 1998; Folkard et al., 1996)
[2] (Belli et al., 2000; Sgura, 2000)
[3] (Belli et al., 2000; Bettega et al., 1998)
[4] (Baggio et al., 2002; Belli et al., 2000)

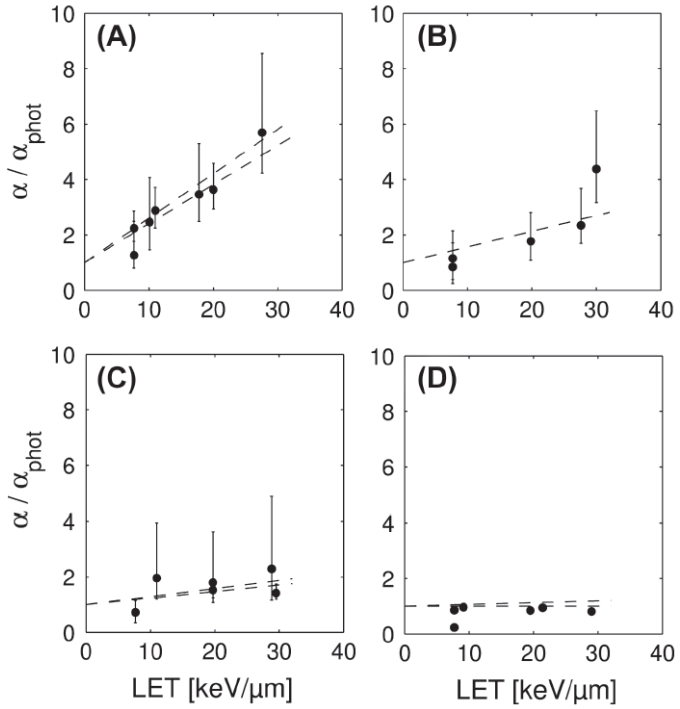

Figure 3-3: Experimentally obtained α/α_x values as a function of LET. Panel A with $(\alpha/\beta)_x = 2.7–3.1$: V79-379A cells (Folkard et al., 1996), V79-753B cells (Belli et al., 1998), and DLD1 cells (Baggio et al., 2002). Panel B with $(\alpha/\beta)_x = 7.7–7.7$: SQ20B (Belli et al., 2000), and C1-1 cells (Sgura, 2000). Panel C with $(\alpha/\beta)_x = 15–18$: C3H10T1/2 (Bettega et al., 1998), and SCC25 (Belli et al., 2000). Panel D with $(\alpha/\beta)_x \geq 70$: HCT116 (Baggio et al., 2002), M/10 cells and HF19 cells (Belli et al., 2000). The error bars show the 95% CI. The dashed lines are obtained with Equation 2 where the highest and lowest $(\alpha/\beta)_x$ in each panel is used (Wedenberg et al., 2013).

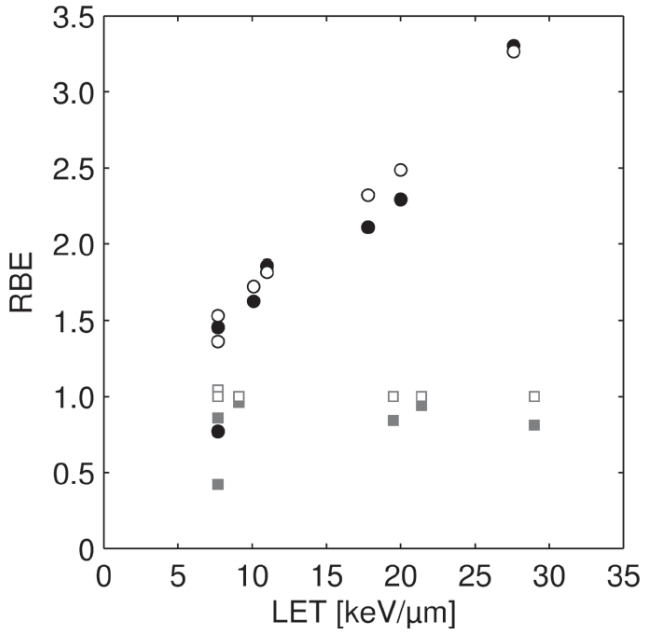

Figure 3-4: RBE as a function of LET at 2 Gy photon dose for cell lines with $(\alpha/\beta)_x$ ratio < 4 (circles) and $(\alpha/\beta)_x$ ratio ≥ 70 (squares). The experimental data is shown with filled symbols and the calculated data from Equation 3 has open symbols (Wedenberg, Lind, & Hardemark, 2013).

Similar to Wilkens and Wedenberg, these concepts are assumed to contain the dependence of the RBE on LET (Giovannini et al., 2016) and are used in an expression for the RBE by McNamara (eq. 3.10) (McNamara et al., 2015).

In order to assess the dependence of RBE_{max} and RBE_{min} on the LET_D the authors used 4 sets of experimental data for V79 cells. Finding the mean, they found an $(\alpha/\beta)_x$ value of 2.686 Gy. Furthermore, a reciprocal dependence was assumed, meaning that tissues with that exact $(\alpha/\beta)_x$ must exactly fit the cell data, whereas other tissues must have a steeper or flatter slope according to their $(\alpha/\beta)_x$ (Carabe et al., 2012). Based on this, eq. 3.6 and 3.7 could be expressed as:

$$RBE_{max}[(\alpha/\beta)_x, LET_D] = 0.834 + 0.154\frac{2.686}{(\alpha/\beta)_x}LET_D \tag{3.8}$$

$$RBE_{min}[(\alpha/\beta)_x, LET_D] = 1.09 + 0.006\frac{2.686}{(\alpha/\beta)_x}LET_D, \tag{3.9}$$

3.4 McNamara model (MCN)

McNamara, Schuemann and Paganetti proposed a RBE model based on the linear quadratic (LQ) model and a comprehensive dataset from a review study (Paganetti, 2014). The review study collected 76 different reports on proton RBE with over 287 experimental data points for the model to fit using non-linear regression (McNamara et al., 2015).

As mentioned in section 3.1, there are many ways to express the RBE formula, based on the same LQ-based RBE model. In order to have proton RBE depend on the dose average LET (LET_D), photon reference parameters $(\alpha/\beta)_x$ and dose, McNamara et. al. used:

$$RBE\left(D_p, \left(\frac{\alpha}{\beta}\right)_x, LET_D\right) = \frac{1}{2D}\left(\sqrt{\left(\frac{\alpha}{\beta}\right)_x^2 + 4D\left(\frac{\alpha}{\beta}\right)_x RBE_{max} + 4RBE_{min}^2 D^2} - \left(\frac{\alpha}{\beta}\right)_x\right). \tag{3.10}$$

This is the expression used in this thesis during calculation and programming. Wilkens model and Wedenberg model will be expressed in terms of RBE_{max} and RBE_{min} in section 3.5. The dependence of the RBE_{max} value on LET_D is similarly to Carabe et. al. (Carabe et al., 2012) assumed to be linear. However, McNamara et. al. assume that RBE_{min} has a dependence on $\sqrt{(\alpha/\beta)_x}$ (Jones, 2015):

$$RBE_{max}[(\alpha/\beta)_x, LET_D] = p_0 + \frac{p_1}{(\alpha/\beta)_x}LET_D \tag{3.11}$$

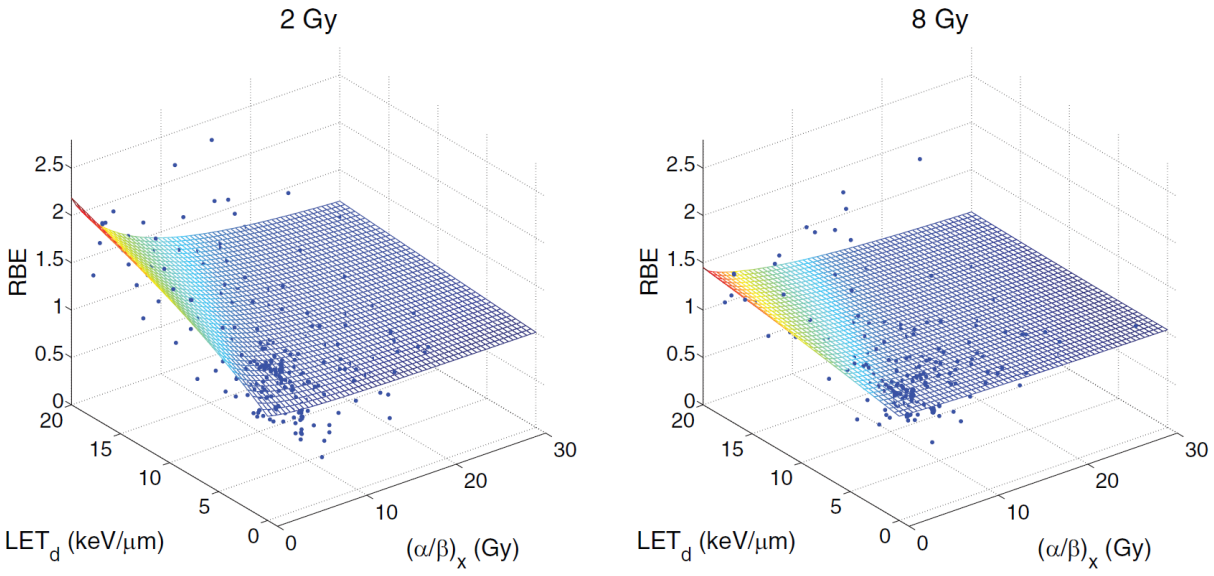

Figure 3-5: The RBE as a function of LET_D and $(\alpha/\beta)_x$ for a dose of 2 Gy (left panel) and 8 Gy (right panel) as predicted by the model. The experimental data used in the fit is also plotted. The LET_D is given relative to the reference photon radiation (McNamara, Schuemann, & Paganetti, 2015).

$$RBE_{min}[(\alpha/\beta)_x, LET_D] = p_2 + p_3\sqrt{(\alpha/\beta)_x}LET_D, \tag{3.12}$$

where p_{0-3} are fit parameters, calculated using a non-linear regression technique in Matlab. Table 3-B lists the parameters while figure 3-5 shows the calculated RBE for different LET values.

Table 3-B: McNamara best fit parameters

Parameter	Value	Standard Error
p_0	0.99064	0.014125
p_1	0.35605	0.015038
p_2	1.1012	0.0059972
p_3	−0.0038703	0.00091303

3.5 Models summary and comparison

In table 3-C the different models are listed, with some important differences and similarities highlighted.

Table 3-C: Model summary

Model	Cell line	LET threshold	Data points	Reference Radiation	Proton parameters	Photon parameters
WIL	V79	30	19	Cobalt 60	$\alpha = 0.1 + 0.02L$ $\beta = \beta_x$	$\alpha_x = 0.112$ $\beta_x = 0.0298$
WED	Many	30	24	200 kV x-rays 240 kV x-rays ^{60}Co γ-rays ^{137}Cs γ-rays	$\frac{\alpha}{\alpha_x} = 1 + \frac{0.434L}{(\alpha/\beta)_x}$ $\frac{\beta}{\beta_x} = 1$	Many
CAR	V79	20	44	250 kVp x-rays d^{16}Be neutrons	$RBE_{max} = 0.834 + 0.154\frac{2.686}{(\alpha/\beta)_x}LET_D$ $RBE_{min} = 1.09 + 0.006\frac{2.686}{(\alpha/\beta)_x}LET_D$	$(\alpha/\beta)_x = 2.686$
MCN	Many	20	285	Many	$RBE_{max} = 0.991 + \frac{0.356}{(\alpha/\beta)_x}LET_D$ $RBE_{min} = 1.1 - 0.004\sqrt{\left(\frac{\alpha}{\beta}\right)_x}\,LET_D$	$(\alpha/\beta)_x = 2.686$

An important thing to note is that some of the models uses 200-250 kV x-rays while some use Cobalt 60 gamma-rays as reference radiation, a more clinically relevant radiation (Mairani et al., 2016). This is important because the LET resulting from these photons vary, due to their respective secondary electrons (Mairani et al., 2016). The LET-energy relation is illustrated in figure 3-6. Out of the models above, Wilkens and McNamara have tried to accommodate this. Wilkens et al. applied a correction factor of 1.1 to all RBE values that were reported with a reference radiation of 200 kVp or 240 kVp X-rays (Wilkens & Oelfke, 2004). While not stated in the article, they implicitly used the following formula (Mairani et al., 2016):

$$RBE = \frac{D_{60Co}}{D_{ph}} \tag{3.13}$$

McNamara et al. based their study on data presented by Paganetti (Paganetti, 2014), in which they did not use the absolute proton LET_D values, but instead used relative values to the reference photon generated LET_D values (6MV). While not stated in the article, they implicitly used the following formula without the final part (Mairani et al., 2016):

$$LET^* \equiv LET - LET_{ph}\ (+LET_{co60}) \tag{3.14}$$

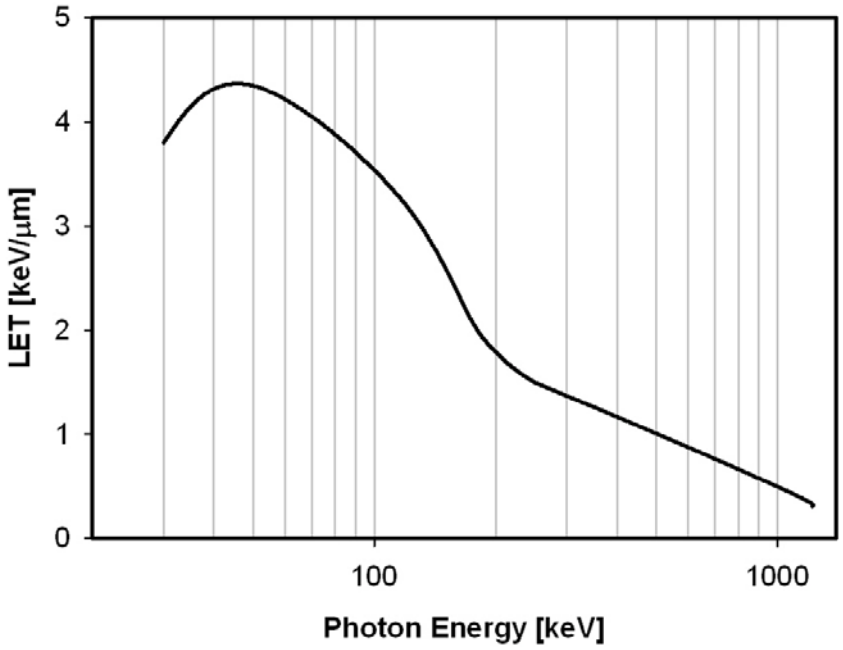

Figure 3-6: LET_D of the resulting electrons as a function of the photon energy used for normalizing proton LET_D values (Kellerer, 2002).

As for the Wedenberg and Carabe models, they do not apply any correction factor to the LET for the different reference radiations.

Another important thing is that the models of Wilkens and Carabe are based on V79 cells with $(\alpha/\beta)_x = 3.758$ and $(\alpha/\beta)_x = 2.686$ respectively, yet these models are to be used on different tissues/organs with different $(\alpha/\beta)_x$. Carabe et al. addressed this in the article by arguing that the RBE-LET_D relationship should include the dependence of RBE on $(\alpha/\beta)_x$ (Carabe et al., 2012). They assumed a simple reciprocal dependence of the RBE on $(\alpha/\beta)_x$, with $(\alpha/\beta)_x = 2.686$ as the base. This is seen in the formulas 3.8 and 3.9 or in table 3-C, with the parameters 0.843, 0.154, 1.09 and 0.006 describing the intersection point and slope of the relationship. Wilkens model on the other hand does not have such a correction and only uses the constant values of $\alpha_x = 0.112$ and $\beta_x = 0.0298$ (Wilkens & Oelfke, 2004). Wedenberg and McNamara base their models on multiple cell-lines.

The different models include different assumptions. Wilkens et. al assumes a linear dependence of α_p on LET_D and a β that is independent of LET_D (Wilkens & Oelfke, 2004). Wedenberg et. al. also assumes a linear α_p-LET_D relation, but with a slope that depends on cell type represented by the $(\alpha/\beta)_x$ ratio. They also see a weak correlation between β and LET_D, and therefore assumes $\beta = \beta_x$ like Wilkens (Wedenberg et al., 2013). Carabe et. al. assumes a LET_D of 10 keV µm^{-1} at the mid-SOBP positions for the beams they used to acquire the average $(\alpha/\beta)_x$ of 2.686 Gy. They also assume a simple reciprocal dependence of RBE_{min} and RBE_{max} on $(\alpha/\beta)_x$, which they assume to vary within 0.5 and 20 Gy, as well as a linear relationship with respect to LET_D (Carabe-Fernandez et al., 2007). McNamara et. al. assumes the same relationship for RBE_{max} as Carabe, but instead assumes that RBE_{min} depends on $\sqrt{(\alpha/\beta)_x}$.

The data points used by the different models are quite similar. Notice the figures 3-1, 3-3 and 3-5 are actually showing the same thing. Figure 3-5 is a 3D figure with RBE, LET and $(\alpha/\beta)_x$, while 3-3 shows slices of the $(\alpha/\beta)_x$ axis, except with α/α_{phot}. Figure 3-1 shows a couple of slices together in the same plot.

For ease of programming, all of these models needs to be expressed with the same RBE formula and parameters. The α_x and β_x parameters for the reference radiation are set to 0.112 and 0.0298 respectively (Cobalt 60, V79 cells) for the WIL model (Wilkens & Oelfke, 2004). This leads to the $(\alpha/\beta)_x$ value of $\sim$3,7584. The other models have $(\alpha/\beta)_x = 2.686$ (Carabe-Fernandez et al., 2007). The RBE expression which is used throughout this study is eq. 3.10, which means eq. 3.2-3.5 needs to be reformulated. Using eq. 3.6 and 3.7, the formulas are reformulated and are listed together with eq. 3.8, 3.9, 3.11 and 3.12 in table 3-D[5].

Table 3-D: Models RBE_{max} & RBE_{min} parameters

Model	RBE_{max} and RBE_{min} parameters
Wilkens	$RBE_{max} = 0.893 + 0.179L$ $RBE_{min} = 1$
Wedenberg	$RBE_{max} = 1 + 0.162L$ $RBE_{min} = 1$
Carabe	$RBE_{max} = 0.834 + 0.154L$ $RBE_{min} = 1.09 + 0.006L$
McNamara	$RBE_{max} = 0.991 + 0.133L$ $RBE_{min} = 1.1 - 0{,}007L$

[5] Approximate numbers, exact numbers are used when simulating and acquiring the results.

4 Methods and materials

This chapter will elaborate on the work put into the simulations, scripting and how the results were calculated. It is split into two parts: The TPS, FLUKA and simulations part, as well as the post-processing part with Python. In short, the patient CT images were converted into a voxel geometry and a TPS made the treatment plan. These were then imported into FLUKA which simulated and calculated the dose and LET_D. This data was then processed in custom scripts to acquire the RBE. Illustrations of the patient voxel geometry and the water phantom geometry is found in figures 4-1 and 4-2.

4.1 Simulations with FLUKA

FLUKA version 2011.2c.4 was used in the thesis, as well as the advanced user interface for FLUKA: Flair, version 2.2-3 [R3899] (Böhlen et al., 2014; Ferrari et al., 2005).

4.1.1 Patient materials and water phantom

Before the CT images can be used in Flair, the dose plan for the voxel geometry is created by a TPS. Used in this thesis and in the PhD by Stokkevåg (Stokkevag, 2016) is the commercial TPS called Varian Eclipse (Varian Medical Systems, Palo Alto, CA). After importing the images and drawing the PTV, Eclipse attempts to deliver the prescribed dose to the PTV during a fast simulation, which is the basis for the beam used in Flair. The fast simulation was optimized by applying minimum and maximum caps on the PTV and surrounding tissue and running additional iterations. The water phantom used is a 20 x 20 x 20 cm^3 volume of water with a 4 x 4 x 4 cm^3 PTV in the center, assigned a prescribed biological dose of 2 Gy($RBE_{1.1}$).

The patient data used in this thesis was provided by Stokkevåg C.H., which was used in her PhD (Stokkevag, 2016). It consists of CT images of a paediatric patient aged 5 and well as an actual treatment plan, with all target volumes and OARs delineated by experienced radiation oncologists. The patient is receiving treatment for medulloblastoma (brain cancer), which tend to spread via the cerebrospinal fluid surrounding the brain and spinal cord. The treatment involves 4 intensity-modulated proton therapy (IMPT) treatment fields using active scanning. Two of the fields are directed at the brain (shown in figure 4-1), while two are directed at the upper and lower spine volume, entering the patient from the back. The PTV surrounding these structures was assigned a prescribed biological dose of 23.4 Gy ($RBE_{1.1}$).

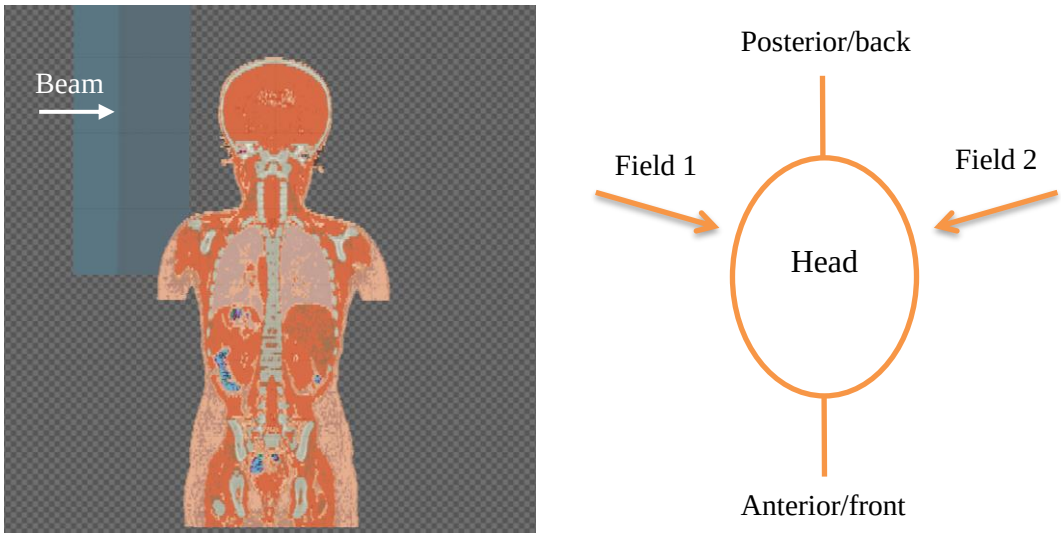

Figure 4-1: Patient geometry of a 5-year-old girl. The spatial resolution is 0.125 x 0.125 x 0.3 cm. The blue object in the upper left in the range-shifter for one of the cranium fields, which is used to account for treatment-head to patient distance in air. The cranium fields enter the head at a ±75 degree angle of the posterior (back) direction.

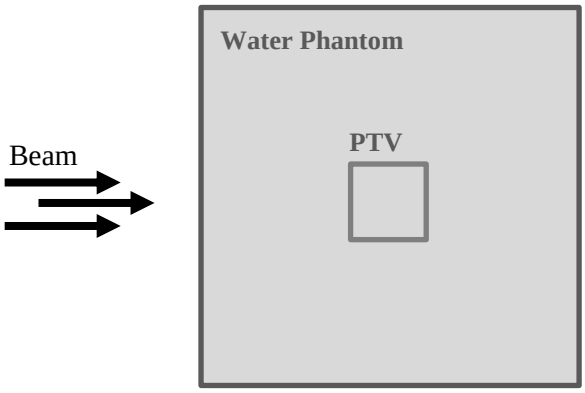

Figure 4-2: Illustration of the 20 x 20 x 20 cm^3 water phantom. The PTV is located in the iso-center and is 4 x 4 x 4 cm^3.

4.1.2 FLUKA and Flair setup

Once sufficient optimization was applied to the beam, the CT images, structure plan and beam data were processed by a Python script made by Fjæra, L.F. (Fjæra, 2016). The script renamed and sorted the CT and structure files, as well as creating different files which contain settings and commands on how FLUKA should simulate and calculate the dose and LET_D. Calibration curves and material conversion files were also made. Next, the CT images were corrected by

applying vacuum outside the patient body. This is done because in Eclipse the Hounsfield units (HU) outside the patient is set to -1000 (air), which is now corrected to -1024 (vacuum). To correct for the distance of air between patient and treatment head, a "range shifter" made of water was placed in each field as seen in figure 4-1. Because the water phantom is only for analytical purposes, the range shifter is not needed during its simulation.

The physics settings provided by the HADROTHE card were applied. Among the different files there is also a beam.dat file which lists all the beam data (i.e. energy, position, angle, weighting, etc.). The beam.dat file was created automatically in Eclipse and is the optimized beam to deliver the predicted dose distribution from the TPS (4.1.1).

The import to FLUKA was based on Fjæra's work (Fjæra, 2016). In short, the Hounsfield Units (HU) were converted to density and material composition in flairs DICOM module using the material and calibration files. The different input cards needed were generated automatically in the sorting script mentioned above, though the energy spread was set manually to 0.91%. This value was set based to trial and error on a water phantom to get the best agreement between FLUKA and the TPS for the SOBP water phantom setup.

4.1.3 Running the simulation

For the patient, 5 independent simulation cycles were used for each of the 4 fields. 10^7 particles were assigned to each cycle, so in total the number of particles per field were $5*10^7$ (50 million). The water phantom was assigned 8 cycles (1 field) with $1.25*10^6$ particles per cycle, making a total of 10^7 (10 million) particles. Once completed the data from each cycle were merged for each data type (dose, LET_D).

4.2 Post-processing

Once FLUKA had finished the simulations, the scoring files containing the dose and LET_D data were converted back into DICOM files using a script made by Fjæra (Fjæra, 2016). The spatial resolution on the water phantom were 0.2 x 0.2 x 0.2 cm, while the patient files had a spatial resolution of 0.125 x 0.125 x 0.3 cm. The conversion was done by using the Pydicom library in Python, updating the dose matrix from the original DICOM files with the FLUKA calculated dose distribution matrix. The biological dose ($RBE_{1.1}$) from FLUKA were then normalized to the TPS biological dose ($RBE_{1.1}$). The matrixes containing the dose and LET_D, which is the parameters needed in equation 3.10, were then used to calculate the RBE from the models. The $(\alpha/\beta)_x$ parameters were assumed to be constants at 3.758 [Gy] for Wilkens model and 2.686 [Gy] for the other models. For every voxel, an RBE value was created for each model, as well as new dose matrixes by multiplying with the physical dose (eq. 2.6).

4.2.1 Slicer and Dose Volume Histograms

Cumulative dose volume histograms (DVHs) visualizes how the dose is distributed in terms of the structure volume. 100% coverage means that the entire structure received a given amount of dose or more. On the other hand, 10% coverage means that only 10% of the volume received the given amount, or more. To draw DVHs for the patient organs and structures, an open source software for medical image informatics called 3D Slicer was used (client version 4.6.2, with SlicerRT extension version 0.18.0) (Fedorov et al., 2012). By importing the structure file made by the TPS and the recalculated DICOM files into Slicer, the DVHs were exported. For simplicity, every structure available was exported in the same file (csv format), which would then be interpreted by a new Python script. Once a csv file was made for every plan ($RBE_{1.1}$, the models, etc.) the script would read all the files and ask for which files to use and which structures to plot.

4.2.2 2D and 1D plotting

To plot 2D dose plots of slices of the patient, another script made by Fjæra, L.F. was used (Fjæra, 2016). This script plotted the dose onto the CT images and a transverse plane was selected where the dose would be plotted, along with outlines of selected structures.

Based on Fjæra's script, a new script was created to do the 1D plotting along one of the axes. The script produces .dat files containing the average dose delivered to specific areas of voxels inside a selected plotting volume. These were then read by the same script used to plot the DVHs (section 4.2.1).

4.2.3 Uncertainty calculation

Using only the statistical uncertainty calculated by FLUKA, the relative (%) uncertainty was calculated for the physical dose and LET_D. For each of the models, the uncertainty was calculated for each RBE_{max} and RBE_{min} formula before following the error propagation to find the uncertainty of the RBE. Details on these calculations, see appendix B.

4.2.4 Model dependency plotting

To plot how the different models respond to changes in certain variables, a script was made that could vary one of the variables in the RBE formula (3.10) while keeping the others constant. One variable, such as dose, was changed while the LET_D and $(\alpha/\beta)_x$ had 2 different changes each, making a 2x2 figure set of how the models respond to dose change. This same process was also done with LET_D and $(\alpha/\beta)_x$. These calculations are entirely analytical and are not part of the MC calculations on water phantom and patient.

5 Results

5.1 Water phantom

5.1.1 Biological dose

The dose distributions from the MC simulations can be observed in figures 5-1 to 5-3. Figure 5-1(b,d,f,h) shows the dose predicted by the models on a plane in the center of the PTV, with the beam entering from the left. From the $RBE_{1.1}$(a) plot it is indicated that a homogeneous biological dose is delivered to the target. However, the results from the variable RBE models illustrates that this may not be the case. In general, the models predict equal or lower dose in the entrance region, while higher doses in the PTV and distal drop-off. The figure also include comparison plots (c,e,g,i) with the $RBE_{1.1}$ distribution. Figure 5-2 and 5-3 shows the longitudinal and lateral distributions respectively. The latter two figures show that the MC simulations have good agreement with the TPS for calculation of $RBE_{1.1}$ dose.

Figure 5-4 is a dose volume histogram, showing the dose coverage for the different beam results. The models all predict a near 100% coverage of at least 1.9 Gy and less than 10% coverage of 2.3 Gy or more. This shows that most of the PTV, according to the models, is receiving a greater dose than the prescribed 2 Gy, but it is contained within roughly 2.15 ± 10%.

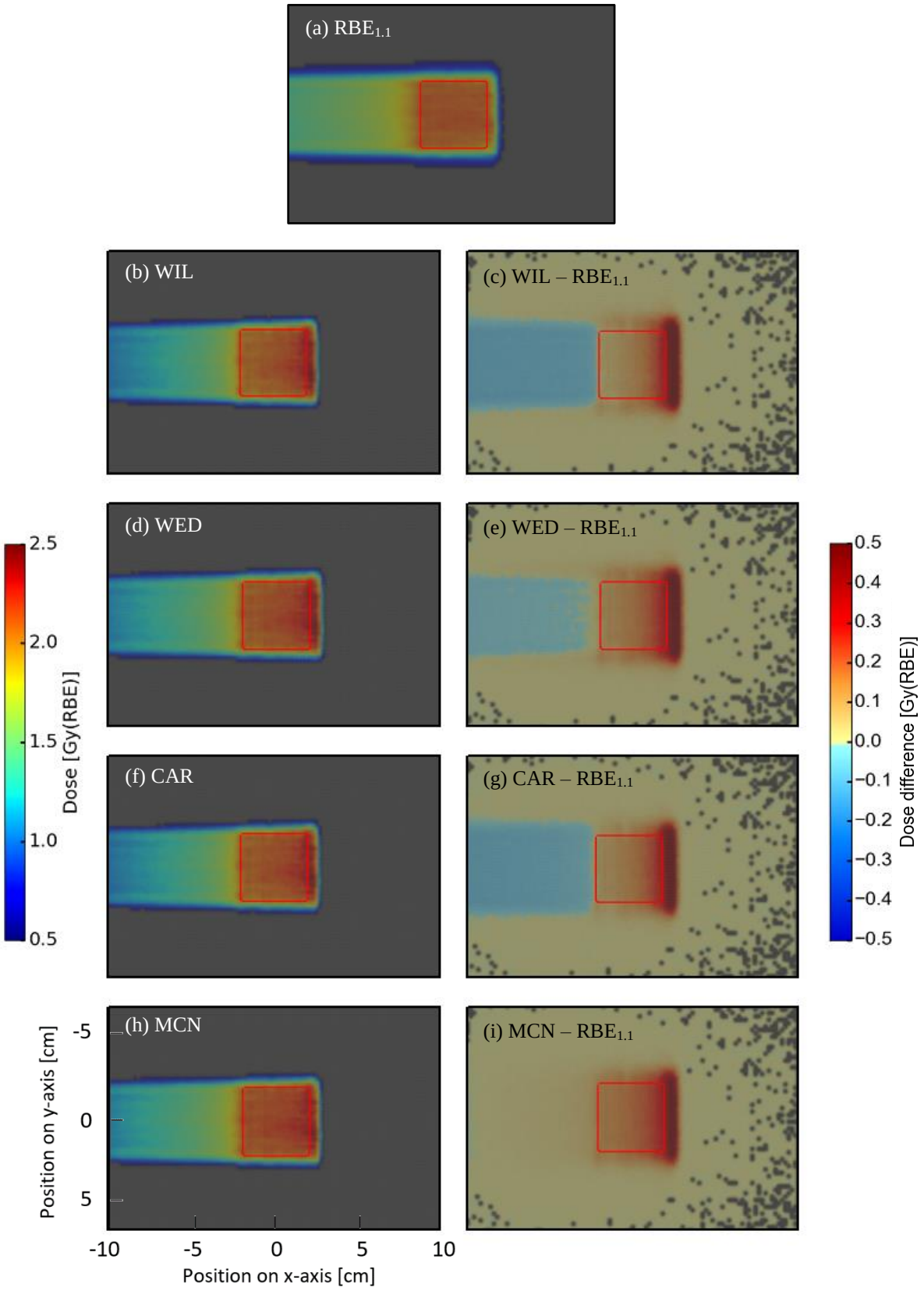

Figure 5-1: 2D water phantom dose distribution plots of the different models used in the thesis. The left column shows the different distributions and uses the color bar on the left. The right column shows the difference between the model distributions and the $RBE_{1.1}$ *distribution at the top (a), while using the color bar on the right. The PTV is a 4x4x4 cm cube in the center and the displayed 2d slices are located in the center of the water phantom and PTV. The dose values in the left column are transparent if the dose is less than 0.5 Gy.*

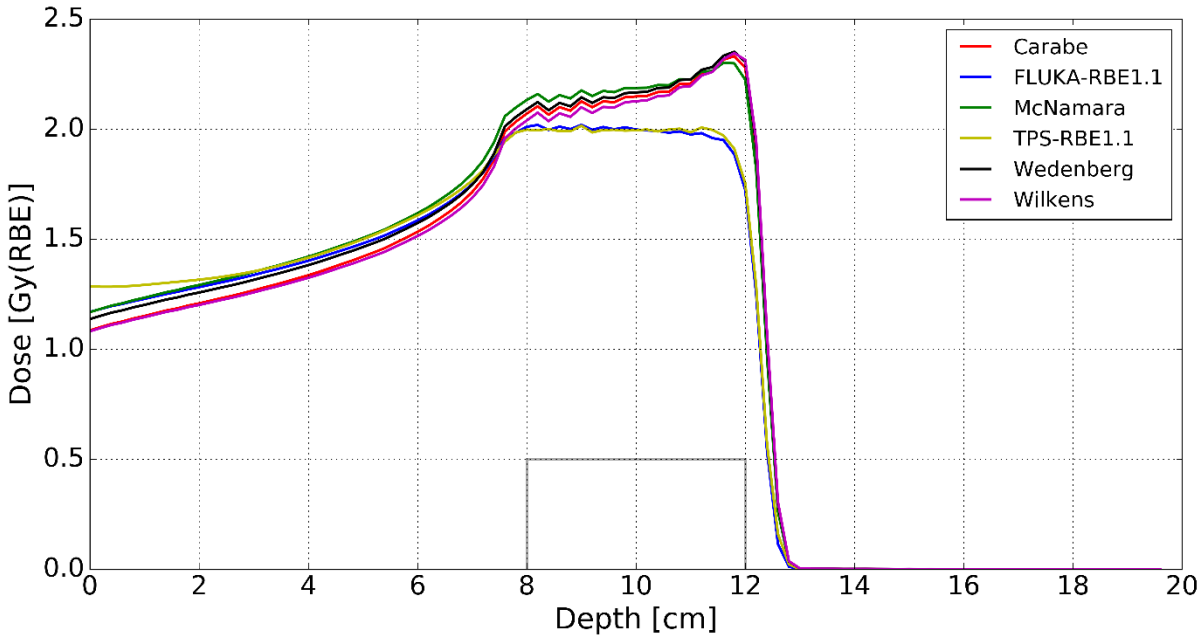

Figure 5-2: 1D longitudinal water phantom dose disribution, where depth is the x-axis equivalent in the 2D plot (y = ± 2). The grey box shows the boundary of the PTV on the depth-axis and is equivalent to the red box in the 2D plot.

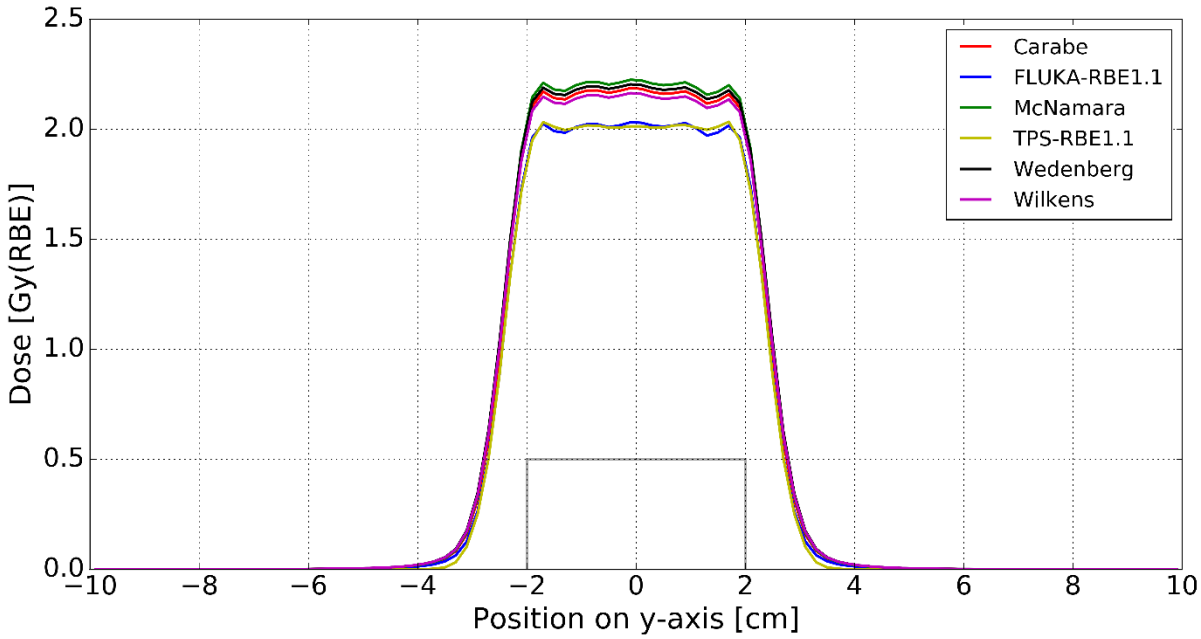

Figure 5-3: 1D lateral water phantom dose disribution, where the y-axis is the same as the y-axis in the 2D plot (x = ± 2). The grey box shows the boundary of the PTV on the y-axis and is equivalent to the red box in the 2D plot.

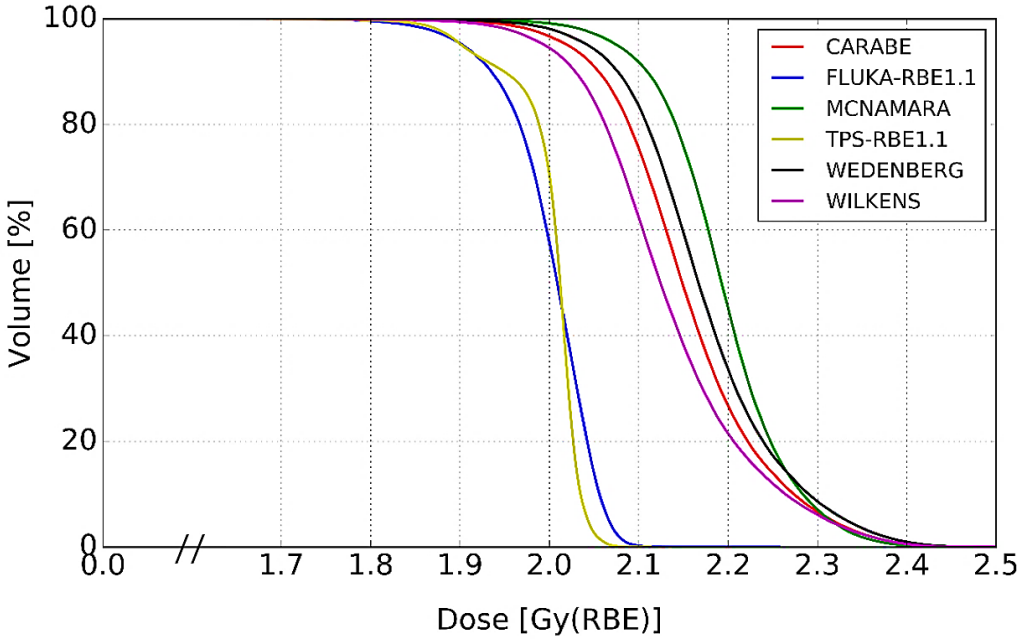

Figure 5-4: Water phantom Dose Volume Histogram (DVH). Values are ~100% from 0 to 1.7 Gy.

5.1.2 Water Phantom RBE

Figure 5-5 shows the RBE distributions calculated by the different models. Voxels containing RBE values larger than 1.5 are all outside the PTV and in low dose areas. We see that the models predict an RBE from 1.0 to 1.15 in the entrance region and RBE from 1.15 to 1.35 in the PTV. The distal drop-off receives RBE values from 1.35 to above 1.5, but the dose is approaching 0.1 Gy which is the cutoff to transparency in the figure. Figure 5-6 is a longitudinal view of 5-5, with the $RBE_{1.1}$ line plotted. From 5-6 we clearly see the entire PTV contains RBE values larger than 1.1, for any of the models. In addition, we see that the WED and MCN models predict RBE values around 1.1 in the entrance region.

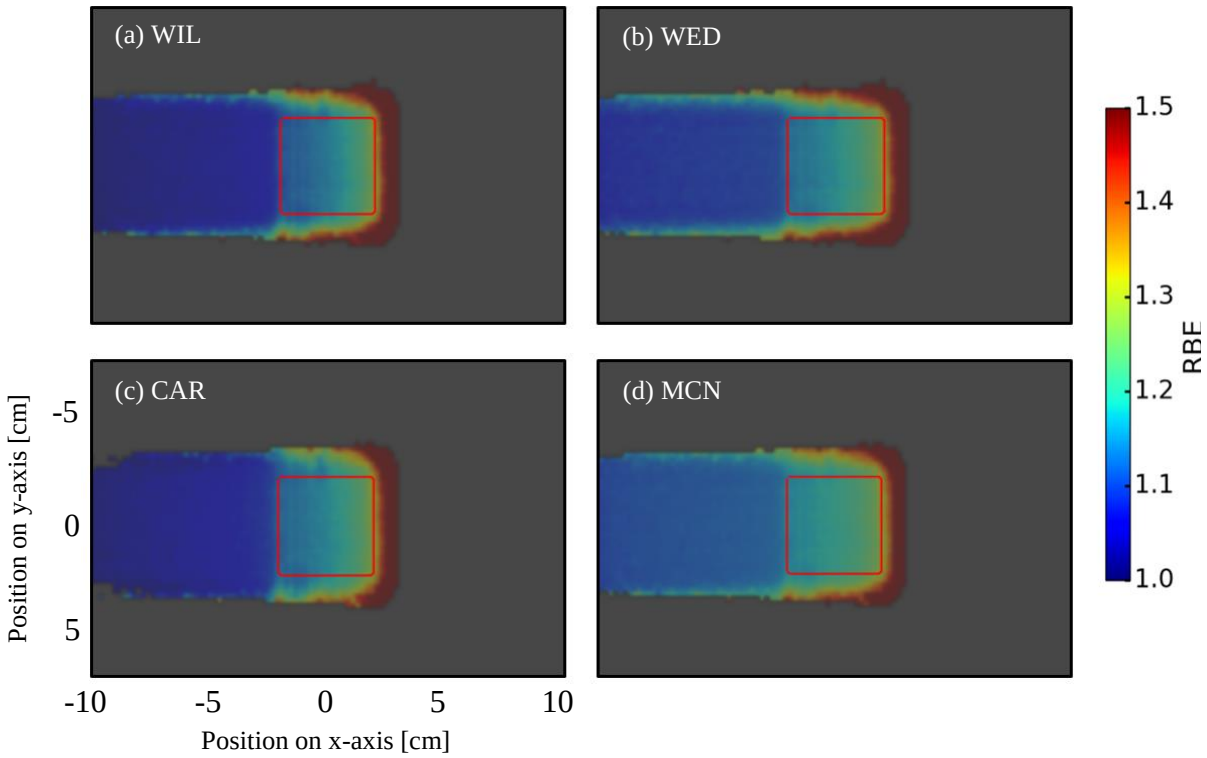

Figure 5-5: 2D water phantom RBE distribution plots of the different models used in the thesis. The PTV is a 4x4x4 cm cube in the center of a 20x20x20 cm water phantom and the displayed slices are located in the center of the phantom and PTV. RBE values are transparent if the dose is less than 0.1 Gy.

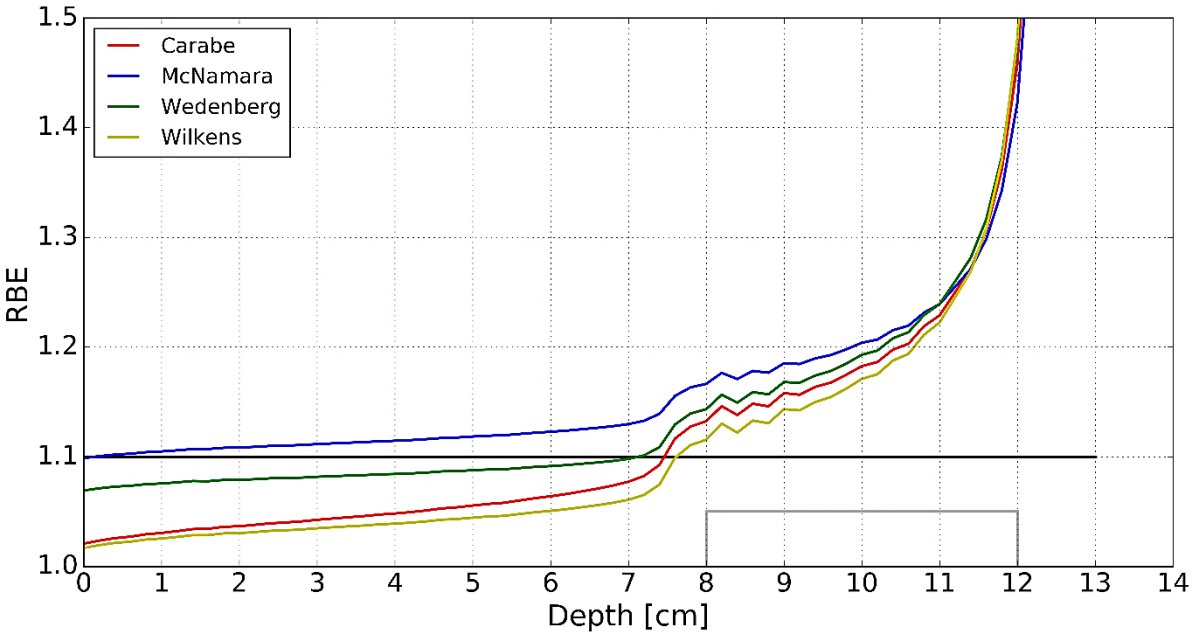

Figure 5-6: 1D longitudinal water phantom RBE distribution, where depth is the x-axis equivalent in the 2D plot (y = ±2). The black horizontal line is $RBE_{1.1}$. The grey box shows the boundary of the PTV on the depth-axis and is equivalent to the red box in the 2D plot.

5.2 Patient case

5.2.1 Biological dose

Figure 5-7 shows the biological doses obtained from MC simulations of the patient case. The PTV is encircled in red like before, while structures like the lungs (blue), heart (yellow) and esophagus (green) are also marked. The $RBE_{1.1}$ plot (a) indicates that a homogeneous biological dose is delivered to the target. Like for the water phantom, figure 5-7(b,d,f,h) shows the dose predicted by the models on a plane at a selected location of interest (see miniature patient in figure), with the beam entering from the posterior (back). This plane was selected because it contains some structures of interest, which will be explained. The figure also include comparison plots (c,e,g,i) with the $RBE_{1.1}$ distribution. The models seem to predict a lower dose in the entrance region, while a higher dose in the PTV and distal drop-off. There is also higher dose laterally. Figure 5-8 and 5-9 shows the longitudinal and lateral distributions respectively. Additional plots are found in appendix D.

Figure 5-10 is a dose volume histogram, showing the structure-specific dose coverage for the different beam results in 3 different structures. Out of the available structures, these were selected based on relevance. The esophagus is longitudinally adjacent to the PTV, while the lungs are lateral. This is why figure 5-7 shows this specific location. Table 5-A contains some specific data points of interest from the DVH. The mean dose to the PTV were 25.3, 25.3, 24.9 and 25.7 Gy for WIL, WED, CAR and MCN models respectively, while for the Lungs: 4.03, 4.01, 3.79 and 3.89 Gy. The Esophagus had 11.5, 10.8, 10.4 and 10.2 Gy. Additional figures with other structures and data is found in appendix A and appendix C.

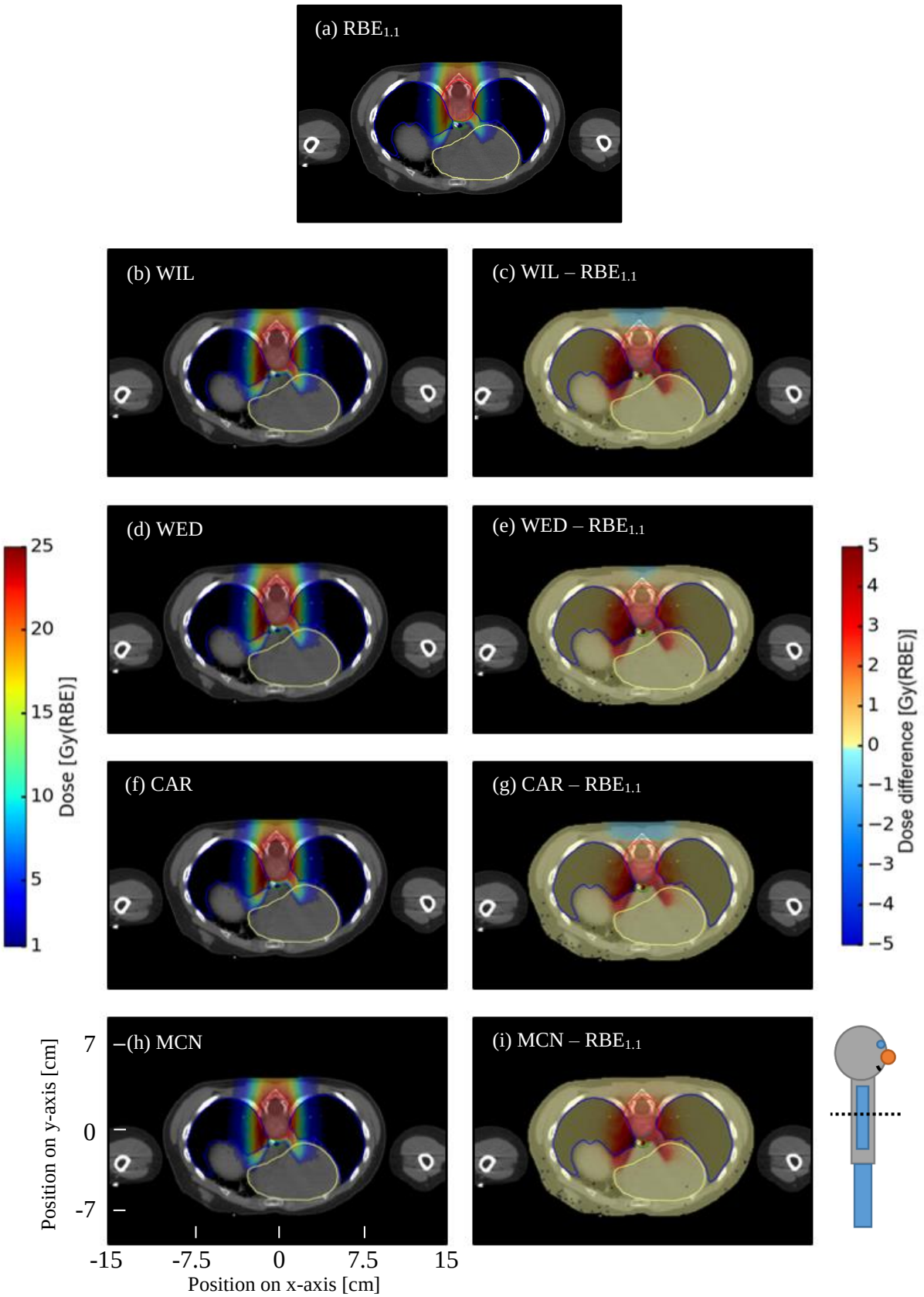

Figure 5-7: 2D patient dose distribution plots of the different models used in the thesis. The left column shows the different distributions and uses the color bar on the left. The right column shows the difference between the model distributions and the $RBE_{1.1}$ distribution at the top, while using the color bar on the right. The PTV is marked by the red curve, while other organs of interest such as the lungs (blue), heart (yellow) and esophagus (green) are also marked. The dose values in the left column are transparent if the dose is less than 1 Gy. The patient arms were assumed to be "outside" the relevant volume (dose < 1 Gy) and were therefore not colored.

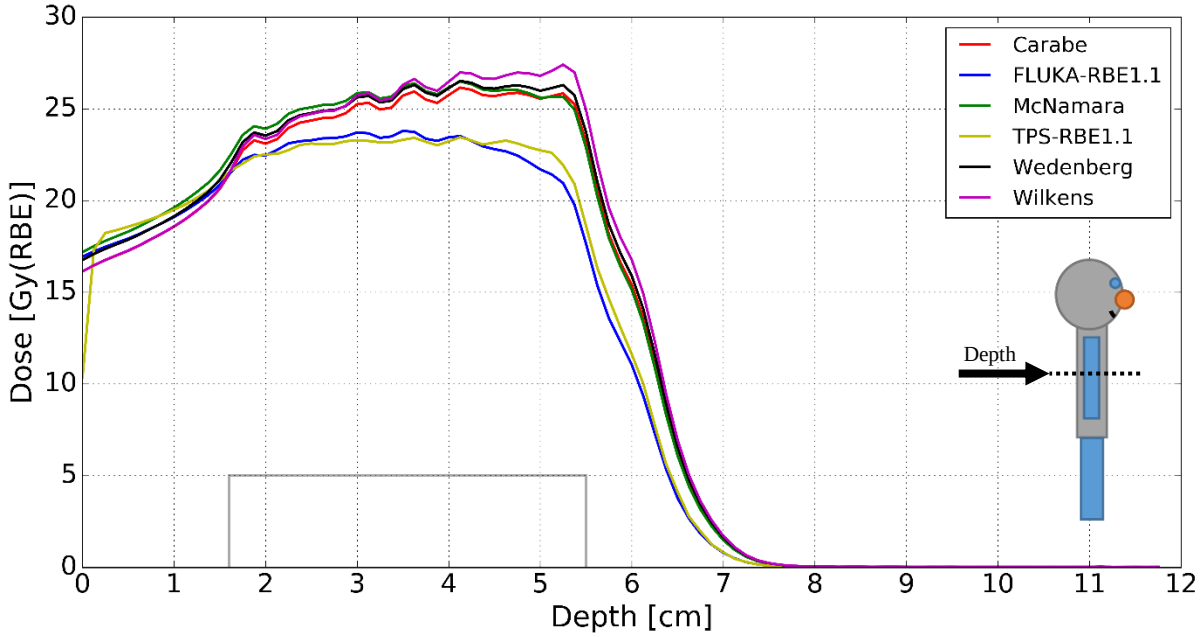

Figure 5-8: 1D longitudinal patient dose distribution, where depth is the y-axis equivalent in the 2D plot (x = ±1). Depth = 0 cm refers to the point of entry into the patient, while approx. 12 cm is the length through the patient. The grey box shows the boundary of the PTV on the depth-axis and is equivalent to the red box in the 2D plot.

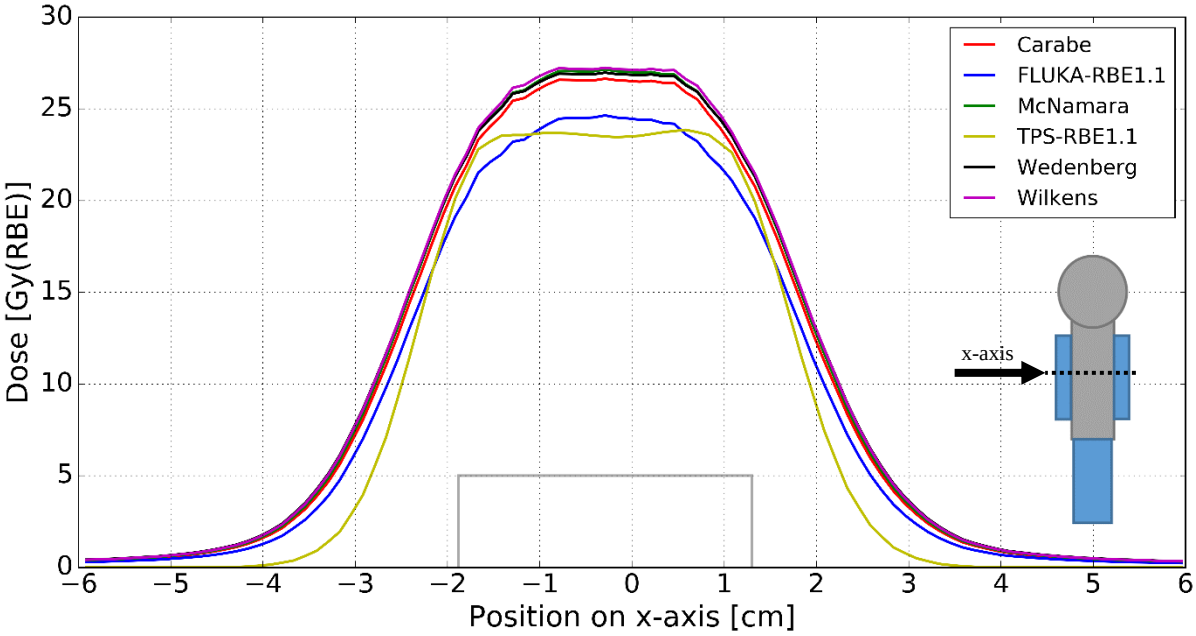

Figure 5-9: 1D lateral patient dose distribution, where the x-axis is the same as the x-axis in the 2D plot (y = ±1.5). This cut from -6 to 6 is all within a relevant volume in the patient geometry, with positive values towards the right of the patient (see miniature model). The patient is between roughly -10.5 to 10.9, however there is only negligible dose distributed outside this cut. The grey box shows the boundary of the PTV on the x-axis and is equivalent to the red box in the 2D plot.

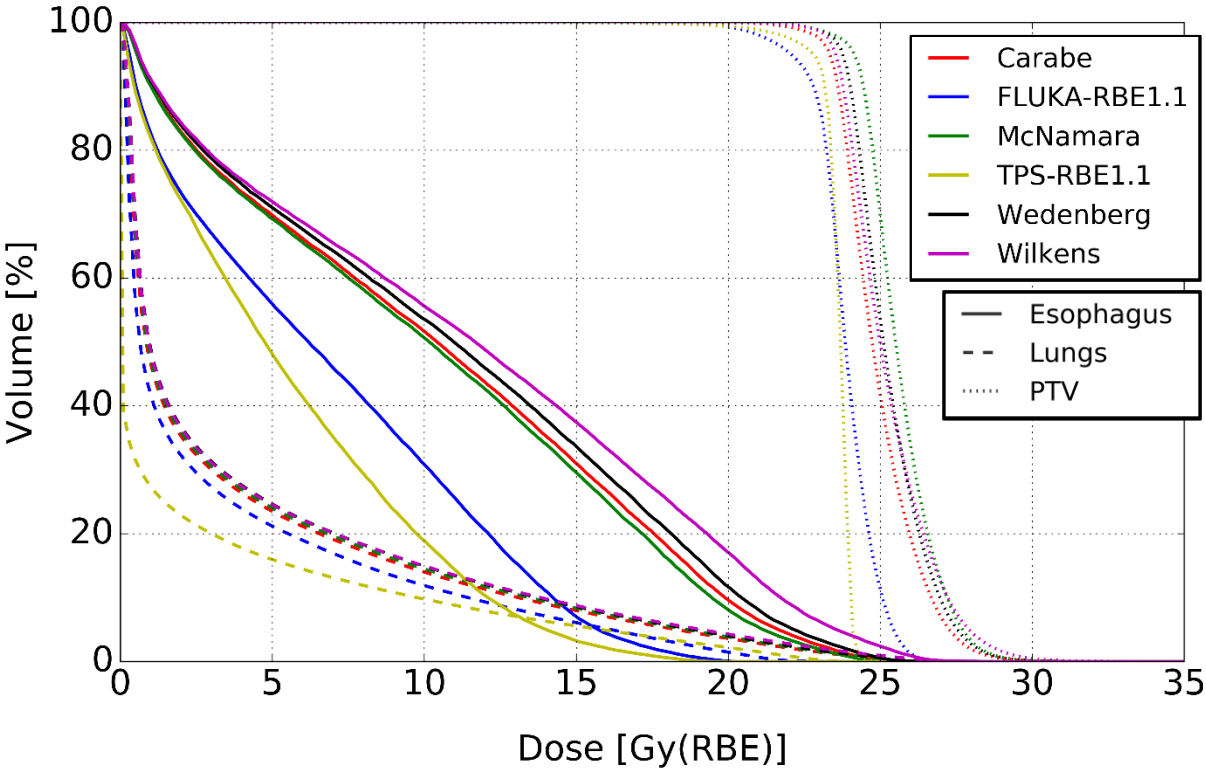

Figure 5-10: Patient DVH for Esophagus, lungs and PTV. Specific values are shown in table 5-A. *Out of all available structures, these were selected based on relevance. Esophagus is longitudinally adjacent to the PTV, while the lungs are laterally adjacent.*

Table 5-A: Patient dose coverage comparison

	$TPS_{RBE1.1}$	$RBE_{1.1}$	Wilkens	Wedenberg	Carabe	McNamara
PTV						
D_2	24.239	25.837	28.802	28.222	27.973	28.306
Mean	23.581	23.847	25.276	25.310	24.944	25.657
Lungs						
D_2	20.299	19.349	23.113	22.610	22.151	22.376
Mean	2.3852	3.2226	4.0301	4.0075	3.7909	3.8943
Esophagus						
D_2	16.087	17.551	25.262	23.882	23.381	22.951
Mean	5.6292	6.8298	11.505	10.837	10.412	10.172

5.2.2 Patient case RBE

Figure 5-11 shows the RBE distribution for the patient plan calculated by the different models. As also seen in the water phantom, there is an increase in RBE both longitudinally and laterally, with a high RBE in both esophagus and lungs. Additional slices of the patient are found in appendix D.

Figure 5-12 is a RBE volume histogram for PTV, lungs and esophagus, with table 5-B listing specific values. The esophagus seems to have RBE values from roughly 1.4 and up to 3, while lungs have values between 1.2 and 2.2. Both structures have much higher values than what the PTV contains, which is between 1.1 and 1.4. Additional figures and DVHs with other structures and data is found in appendix A and appendix C.

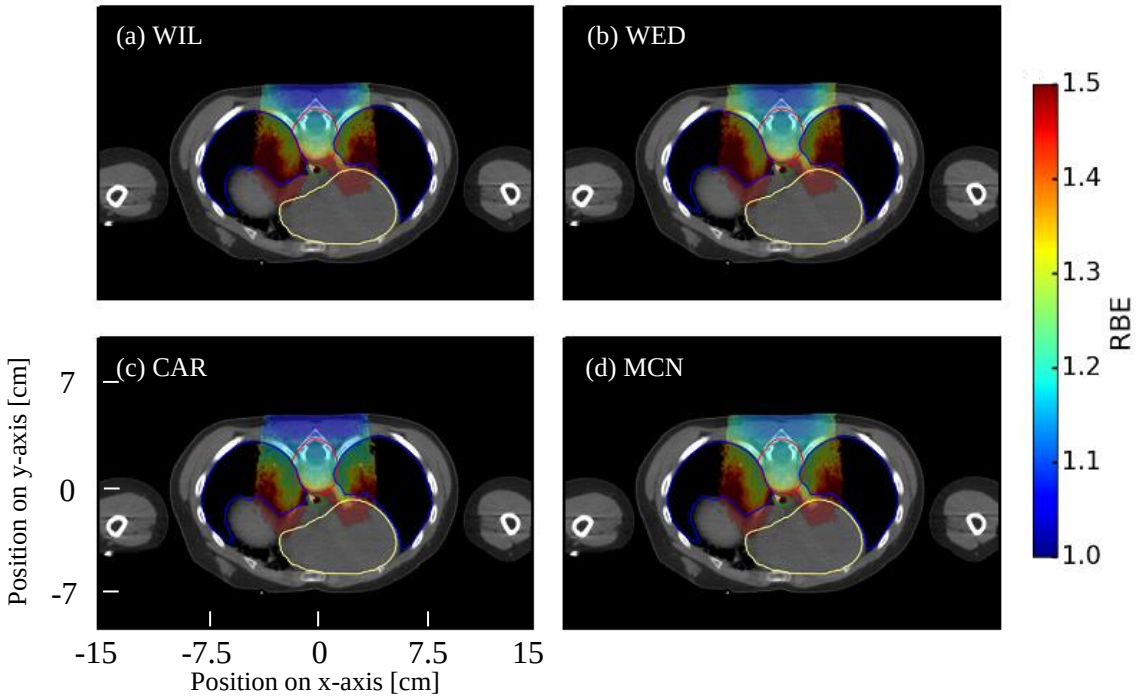

Figure 5-11: 2D patient RBE distribution plots of the different models used in the thesis. The PTV is marked by the red curve, while other organs of interest such as the lungs (blue), heart (yellow) and esophagus (green) are also marked. The RBE values in the plots are transparent if the dose is less than 1 Gy.

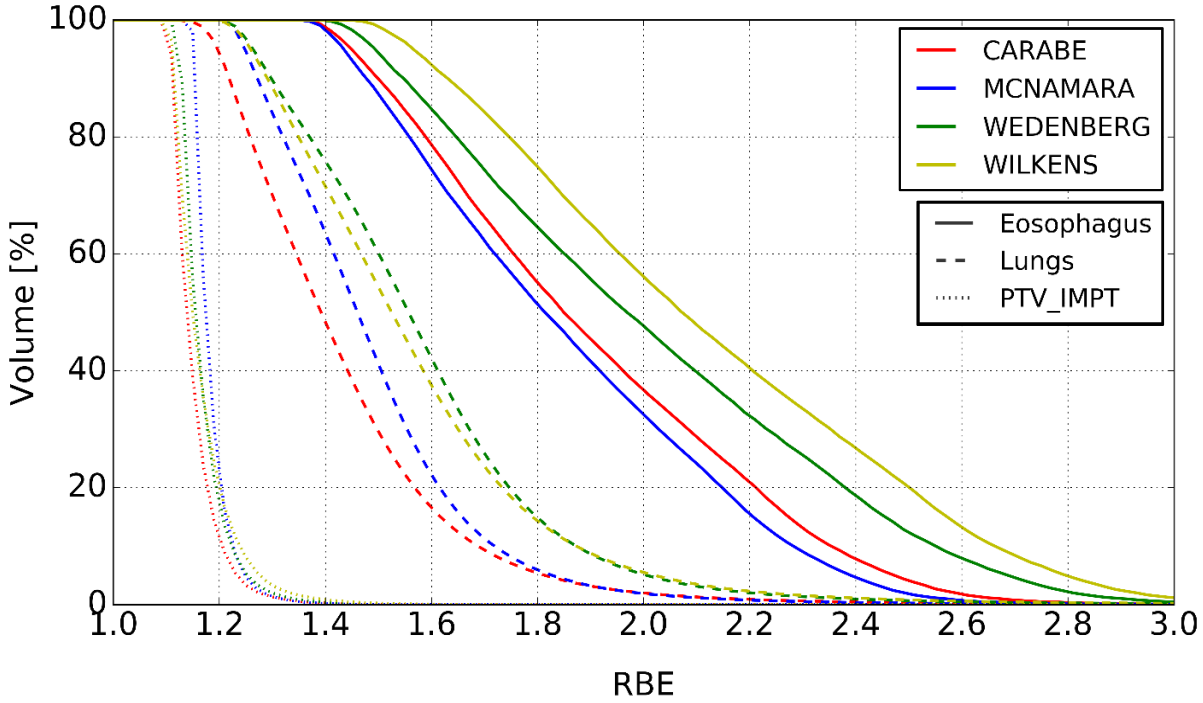

Figure 5-12: RBE Volume Histogram for the patient. See table 5-B *for some specific values.*

Table 5-B: Patient RBE coverage comparison

	Wilkens	Wedenberg	Carabe	McNamara
PTV				
RBE_2	1.3840	1.3000	1.2986	1.2988
Mean	1.1667	1.1605	1.1511	1.1840
Lungs				
RBE_2	2.2548	2.2273	2.0248	2.0195
Mean	1.5662	1.5830	1.4335	1.4874
Esophagus				
RBE_2	2.9433	2.8455	2.6268	2.4965
Mean	2.1214	2.0165	1.8988	1.8542

5.3 Uncertainties

The uncertainties for the physical dose of the water phantom were found to reach 1.3% in the distal PTV, while the RBE of the water phantom reached about 0.14%. More on the uncertainty is found in appendix B.

5.4 Model dependencies

The different models depend on dose, LET_D and $(\alpha/\beta)_x$ differently. Figures 5-13 to 5-15 illustrates these dependencies, while varying the other two parameters.

For the $(\alpha/\beta)_x$ dependency we see that increasing LET_D increases the effect of $(\alpha/\beta)_x$, while increasing dose decreases the effect. On the other hand, while the models remain roughly equally dependent on $(\alpha/\beta)_x$ with increasing LET_D, we see that the WED and MCN models separate from the CAR model with increasing dose. Since the WIL model does not depend on $(\alpha/\beta)_x$, it is a straight line.

For the LET_D dependence, we see that increasing $(\alpha/\beta)_x$ decreases the effect of LET_D, separating the WIL model from the others, which is unaffected. Increase the dose also seems to decrease the dependency, which also affects the WIL model.

For the dose dependence, we see that increasing $(\alpha/\beta)_x$ greatly reduces the effect of the dose on the WED, CAR and MCN models. On the other hand, increasing LET_D will increase the dependence.

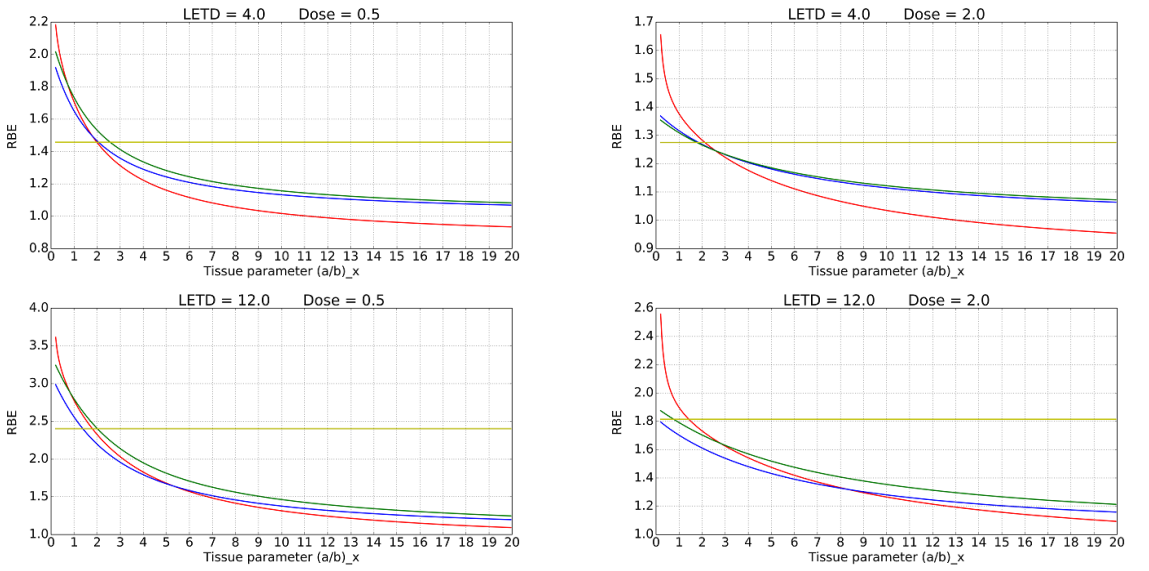

Figure 5-13: Illustrates the models dependence on the tissue parameter from 0.2 to 20. LET and dose are kept constant at 4,12 and 0.5,2 respectively.

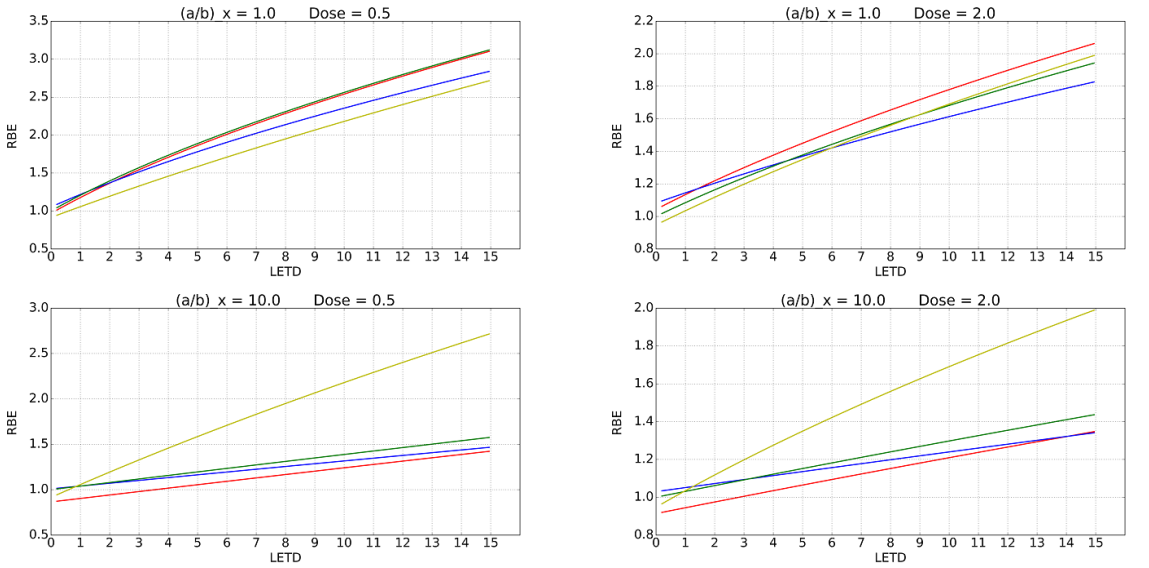

Figure 5-14: Illustrates the models dependence on LET_D from 0.1 to 15. $(\alpha/\beta)_x$ and dose are kept constant at 1,10 and 0.5,2 respectively.

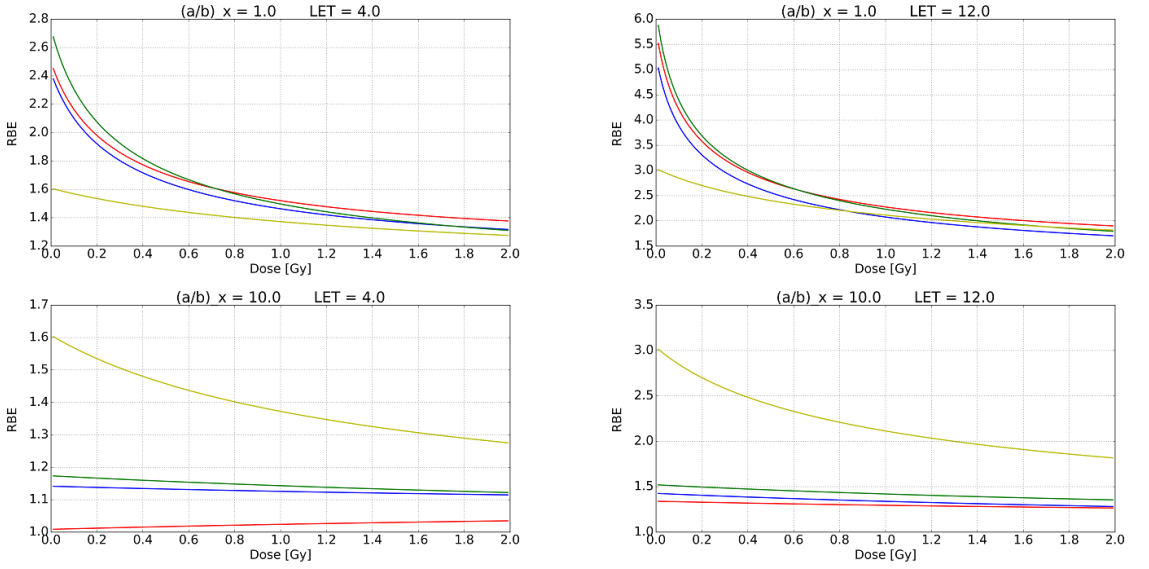

Figure 5-15: Illustrates the models dependence on the dose from 0.01 to 2. LET and $(\alpha/\beta)_x$ are kept constant at 4,12 and 1,10 respectively.

6 Discussion

6.1 Differences between the RBE models

6.1.1 Result dose difference

The dose on the water phantom gives a good first impression of the differences between the models and FLUKA vs the TPS (Eclipse) while working with a simple geometry and plot. Also, because the water phantom only contains water and all models are set up to the V79 cell line with $(\alpha/\beta)_x$ = 2.686 Gy (except for the WIL model, with 3.758 Gy), the only dynamic factors affecting the RBE should be the LET_D of the protons and physical dose. As seen in figure 5-1, the models in general seems to predict an equal or lower dose in the entrance region of the beam, while a higher dose in the SOBP/PTV and distal region. The low-dose regions excluding the distal drop-off, appears to have similar distributions as the $RBE_{1.1}$ distribution. The MCN model separates itself from the others in the entrance region, where it is predicting an almost identical dose deposit as $RBE_{1.1}$.

For the patient plan, dose distributed past the sides of the PTV is even more noticeable for the models. This is caused by the increased RBE towards the distal region as seen in figure 5-11. The structure-specific dose coverage illustrated in figure 5-10, as well as figures A-1 to A-4 shows that the difference between the models and $RBE_{1.1}$ distribution increases with certain structures. Specifically, the PTV with spinal cord, brain, etc. and structures behind the PTV (distal region) such as the esophagus, trachea, eyes, lenses, thyroid, etc. The increased dose to the PTV from the models compared to the $RBE_{1.1}$ distribution shows that the physical dose to the distal part of the target perhaps could be reduced in order to reduce the dose the OARs.

6.1.2 Result RBE difference

The McNamara model clearly has the narrowest RBE range in the water phantom seen in figures 5-5 and 5-6. Wilkens model on the other hand has the widest RBE range, which is, when calculated from the raw data, almost 50% wider than the McNamara model. This means that, when optimized against the TPS dose, the choice of model will greatly impact the resulting dose.

The RBE distribution for the patient is similar to that of the water phantom in that there is a longitudinal and lateral increase. The structures with the largest deviation in dose from $RBE_{1.1}$, also had the largest RBE, as further deviation from $RBE_{1.1}$ would cause such differences. There is also a noticeable increase in difference between the models, especially the WIL model in the PTV and Esophagus (table 5-B).

6.1.3 Model dose difference summary and comparison to other work

In general, the models were consistently deviating from the $RBE_{1.1}$ distribution. However, as illustrated in the analytical figures 5-13 to 5-15 the different models react differently to change in the variables. As change in the $(\alpha/\beta)_x$ ratio was not included in the calculations of the RBE, the primary differences in the results were caused by change in dose and LET_D. However, as seen in the figures mentioned, the ratio makes a substantial difference in how the models behave and deviate from each other.

Since the WIL model had $(\alpha/\beta)_x$ set to 3.758 instead of 2.686 like the others (section 4.2), this probably caused this model to be more resistant to change in RBE at very low doses as reflected in figure 5-15. However, the WIL model is also the model that depends the most on LET_D in its RBE_{max} formula (table 3-D). Therefore, while RBE_{max} is lower at low LET_D, it increases faster than the other models with increasing LET_D. This is likely what caused the WIL model to predict the widest dose- coverage for the PTV as visualized in figure 5-10 and table 5-A.

The WED model predicted typically an RBE in-between the values estimated by the other models. This could be because the model is less dependent on LET_D than WIL model, due to a different tissue parameter. Arguably, the model is also less dependent on LET_D than the CAR and MCN models for high fraction doses, since the others have an RBE_{min}-LET_D dependence. The WED model is also the model with the highest initial RBE_{max} at low LET_D. Looking at tissue dependence, the model, along with the MCN model, is the least dependent on $(\alpha/\beta)_x$ even at lower doses and LET_D (ignoring Wilkens). This is could be due to the non-dependent RBE_{min}.

The Carabe model is the only model where RBE_{min} is increasing away from 1 as LET_D increases. This effect becomes more important with increasing dose and LET_D, as seen from formula 3.10 and figure 5-14, where the model starts to separate itself from the other models. The model seems to be susceptible to larger LET_D changes compared to the other models. The CAR model has, like the WED model, predicted doses and RBE that often was in-between the other models.

The least variation-susceptible model appears to be the McNamara model. The model had in general the narrowest RBE range both for the water phantom and for the patient. This is probably due to the model having the lowest RBE_{max}-LET_D dependence, as well as an RBE_{min} approximately 1 (within a relevant LET_D range). As mentioned above, the model is also one of the least dependent on the tissue parameter, probably due to the square root in the RBE_{min} formula.

In a comparison article by Giovannini et al. they found some similar dose distribution results when they compared different models such as the WED and CAR models to the $RBE_{1.1}$ distribution. Their analytical plots, where they look at the RBE-LET dependence and RBE-dose dependence, show similar trends to that of figure 5-14 and 5-15. They also make a great point

that using opposite beam arrangements, if available, could be preferable to reduce the LET_D and RBE values in structures (Giovannini et al., 2016). McNamara et al. also compared their model with the WED and CAR model in terms of RBE-dose, RBE-LET and RBE-$(\alpha/\beta)_x$ dependencies and found similar results (McNamara et al., 2015). Polster et al. found that the WED model calculated the lowest RBE in their water phantom, with the WIL and CAR models predicting higher RBE. This is clearly different than what we see in figure 5-6. However, when comparing the WED model to the $RBE_{1.1}$ on a patient they saw a similar distribution difference (Polster et al., 2015).

6.2 Assumptions in normalization, RBE and uncertainties

One of the most important factors to acquire adequately correct data was the normalization between FLUKA and the TPS. It was done by finding the median dose of the TPS in the PTV [brain] or PTV [spine] depending on the field and setting this value as the median dose for the FLUKA field in the same region. However, this method can lead to large uncertainties. Without knowing the number of particles used in the treatment or the conversion factor between the monitor unit output and the number of particles the normalization can't be completely accurate. For the purposes of this thesis, the normalization method was assumed to be accurate enough for the comparison between the models. The resulting doses found in this thesis should not be used in any clinical scenario, as the normalization must be done properly. FLUKA-TPS comparison figures are found in appendix E.

The $(\alpha/\beta)_x$ ratios were assumed as constants, which in general is not the case. This is not an issue for the water phantom case (as there is no cells in the water), but for the patient case it might lead to significantly incorrect RBE and thus incorrect dose in certain regions and structures. Including variable tissue parameters would also lead to increased uncertainty, since the $(\alpha/\beta)_x$ uncertainty would be considered in formula B. 1. The WIL model was the only model where $(\alpha/\beta)_x = 3.758$ Gy was used, due to equations 3.2 and 3.3 not allowing for other tissue parameters. This, of course, would lead to some noticeable differences compared to the other models as discussed in section 6.1.3.

Only the statistical uncertainty calculated by FLUKA were considered in the uncertainty calculations of the water phantom in this thesis. Fjæra (Fjæra, 2016) touches on the uncertainties of some of the pre-simulation processes. With this in mind, figure B-1 shows that the uncertainty of the physical dose is low, so that we most likely have used enough particles in the water phantom simulation.

6.3 Suggestions for further work

This thesis did not look at the models dependence on a variable $(\alpha/\beta)_x$ as part of the patient dose and RBE results. Further work should be put into creating a way to implement tissue parameters as structure matrixes which for example can be used alongside the structure DICOM-file exported by the TPS. Implementing this into the RBE calculation should improve results and allow for more organ specific research. It could however, increase the uncertainties related to RBE and model doses (Gy(RBE)).

More work should be done on quantifying the uncertainty of dose and RBE on patient data, especially when more than one beam is included. The implementation of the normalization would probably contain some difficult decisions as to how a low dose high uncertainty voxel from one field would combine with a high dose low uncertainty voxel from another.

There should be more work put into generating experimental data on the effects of proton therapy. Right now, this data is scarce compared to that of photon therapy and could greatly increase our understanding of variable RBE, leading to more accurate models in the future. Also, a new study comparing the most recent models should be considered.

7 Conclusion

The models used in this thesis applies various assumptions regarding the different RBE relationships, but do give consistent deviations from the current clinical practice of assuming a constant RBE of 1.1. There has been observed a general trend where the models predict lower dose- and RBE values in the entrance region, while predicting higher values in the PTV and distal drop-off. In addition, there has been observed a lateral dose and RBE increase, which was particularly apparent in the patient case. These longitudinal and lateral increases could be of clinical importance in regards to certain OARs.

RBE values up to 1.38 (RBE_2) was observed in the target volume, while elevated biological dose was seen for all structures, especially for structures in low-dose regions, which had RBE values up to 8.1 (RBE_2) (appendix C). The RBE_{98} was observed to always be greater or equal to 1.1 in any structure, regardless of model, with the exceptions of the body, bladder and normal tissue, which either had parts of the structure in front of the PTV (entrance region) or received a very low dose (mean $\leq$ 0.1 Gy).

The results suggest that implementing variable RBE calculations into clinical scenarios should be considered, at least with dependence on dose and LET_D, and possibly variable tissue parameters when this is implemented into the calculation. This is especially the case if there are any OARs in close proximity to the PTV.

Bibliography

Baggio, L., Cavinato, M., Cherubini, R., Conzato, M., Cucinotta, F. A., Favaretto, S., . . . Williams, J. R. (2002). Relative biological effectiveness of light ions in human tumoural cell lines: role of protein p53. *Radiation Protection Dosimetry, 99*(1-4), 211-214.

Barendsen, G. W. (1968). Responses of cultured cells, tumours, and normal tissues to radiations of different linear energy transfer. *Current Topics in Radiation Research, IV*, 293-356.

Bauer, J., Sommerer, F., Mairani, A., Unholtz, D., Farook, R., Handrack, J., . . . Parodi, K. (2014). Integration and evaluation of automated Monte Carlo simulations in the clinical practice of scanned proton and carbon ion beam therapy. *Phys Med Biol, 59*(16), 4635-4659. doi:10.1088/0031-9155/59/16/4635

Belli, M., Bettega, D., Calzolari, P., Cera, F., Cherubini, R., Dalla Vecchia, M., . . . Grossi, G. (2000). Inactivation of human normal and tumour cells irradiated with low energy protons. *International Journal of Radiation Biology, 76*(6), 831-839.

Belli, M., Campa, A., & Ermolli, I. (1997). A semi-empirical approach to the evaluation of the relative biological effectiveness of therapeutic proton beams: the methodological framework. *Radiat Res, 148*(6), 592-598.

Belli, M., Cera, F., Cherubini, R., Dalla Vecchia, M., Haque, A. M. I., Ianzini, F., . . . Tiveron, P. (1998). RBE-LET relationships for cell inactivation and mutation induced by low energy protons in V79 cells: further results at the LNL facility. *International Journal of Radiation Biology, 74*(4), 501-509.

Belli, M., Cera, F., Cherubini, R., Haque, A. M. I., Ianzini, F., Moschini, G., . . . Tiveron, P. (1993). Inactivation and mutation induction in V79 cells by low energy protons: re-evaluation of the results at the LNL facility. *International Journal of Radiation Biology, 63*(3), 331-337.

Belli, M., Cherubini, R., Finotto, S., Moschini, G., Sapora, O., Simone, G., & Tabocchini, M. A. (2009). RBE-LET Relationship for the Survival of V79 Cells Irradiated with Low Energy Protons. *International Journal of Radiation Biology, 55*(1), 93-104. doi:10.1080/09553008914550101

Bethe, H., & Ashkin, J. (1953). Experimental Nuclear Physics. In E. Segré & J. Wiley (Eds.), (pp. 253). New York.

Bettega, D., Calzolari, P., Marchesini, R., Noris Chiorda, G. L., Piazzolla, A., Tallone, L., . . . Tiveron, P. (1998). Inactivation of C3H10T1/2 cells by low energy protons and deuterons. *International Journal of Radiation Biology, 73*(3), 303-309.

Bielajew, A. F. (2013). History of Monte Carlo *Monte Carlo Techniques in Radiation Therapy* (pp. 3-16): Taylor & Francis.

Blomquist, E., Russell, K. R., Stenerlöw, B., Montelius, A., Grusell, E., & Carlsson, J. (1993). Relative biological effectiveness of intermediate energy protons. Comparisons with 60 Co gamma-radiation using two cell lines. *Radiotherapy and Oncology, 28*(1), 44-51.

Borges, H. L., Linden, R., & Wang, J. Y. (2008). DNA damage-induced cell death: lessons from the central nervous system. *Cell research, 18*(1), 17-26.

Bragg, W. H., & Kleeman, R. (1904). LXXIV. On the ionization curves of radium. *The London, Edinburgh, and Dublin Philosophical Magazine and Journal of Science, 8*(48), 726-738.

Böhlen, T., Cerutti, F., Chin, M., Fassò, A., Ferrari, A., Ortega, P., . . . Vlachoudis, V. (2014). The FLUKA code: developments and challenges for high energy and medical applications. *Nuclear Data Sheets, 120*, 211-214.

Carabe-Fernandez, A., Dale, R. G., & Jones, B. (2007). The incorporation of the concept of minimum RBE (RBE min) into the linear-quadratic model and the potential for improved radiobiological analysis of high-LET treatments. *International Journal of Radiation Biology, 83*(1), 27-39.

Carabe, A., Moteabbed, M., Depauw, N., Schuemann, J., & Paganetti, H. (2012). Range uncertainty in proton therapy due to variable biological effectiveness. *Phys Med Biol, 57*(5), 1159-1172. doi:10.1088/0031-9155/57/5/1159

Comte de Buffon, G. (1777). *Essai d'arithm´etique morale* (Vol. 4).

Dale, R. G., & Jones, B. (1999). The assessment of RBE effects using the concept of biologically effective dose. *International Journal of Radiation Oncology* Biology* Physics, 43*(3), 639-645.

Dunn, W. L., & Shultis, J. K. (2011). *Exploring Monte Carlo Methods*: Elsevier.

Durante, M., & Paganetti, H. (2016). Nuclear physics in particle therapy: a review. *Rep Prog Phys, 79*(9), 096702. doi:10.1088/0034-4885/79/9/096702

Eckhardt, R. (1987). Stan ulam, john von neumann, and the monte carlo method. *Los Alamos Science, 15*(131-136), 30.

Fano, U. (1963). Penetration of protons, alpha particles, and mesons. *Annual Review of Nuclear Science, 13*(1), 1-66.

Fedorov, A., Beichel, R., Kalpathy-Cramer, J., Finet, J., Fillion-Robin, J.-C., Pujol, S., . . . Sonka, M. (2012). 3D Slicer as an image computing platform for the Quantitative Imaging Network. *Magnetic resonance imaging, 30*(9), 1323-1341.

Ferrari, A., Sala, P. R., Fasso, A., & Ranft, J. (2005). *FLUKA: A multi-particle transport code (Program version 2005)*. Retrieved from

Fischer, M., Todorovic, M., Drud, E., & Cremers, F. (2010). Percentage depth dose (PDD). In P. d. dose (Ed.). Journal of Applied Clinical Medical Physics: http://www.jacmp.org/index.php/jacmp/rt/printerFriendly/3131/1871: JACMP: Accessed on 09.01.2017.

Fjæra, L. F. (2016). *Development of a Monte Carlo Based Treatment Planning Verification Tool for Particle Therapy*. (Master), University of Bergen.

Folkard, M., Prise, K. M., Vojnovic, B., Newman, H. C., Roper, M. J., & Michael, B. D. (1996). Inactivation of V79 cells by low-energy protons, deuterons and helium-3 ions. *International Journal of Radiation Biology, 69*(6), 729-738.

Giovannini, G., Bohlen, T., Cabal, G., Bauer, J., Tessonnier, T., Frey, K., . . . Parodi, K. (2016). Variable RBE in proton therapy: comparison of different model predictions and their influence on clinical-like scenarios. *Radiat Oncol, 11*, 68. doi:10.1186/s13014-016-0642-6

Goodhead, D. T., Belli, M., Mill, A. J., Bance, D. A., Allens, L. A., Hall, S. C., . . . Stretch, A. (1992). Direct comparison between protons and alpha-particles of the same LET: I. Irradiation methods and inactivation of asynchronous V79, HeLa and C3H 10T½ cells. *International Journal of Radiation Biology, 61*(5), 611-624.

Gottschalk, B. (2012). Physics of proton interactions in matter. *Proton Therapy Physics*, 19-60.

Grassberger, C., & Paganetti, H. (2011). Elevated LET components in clinical proton beams. *Phys Med Biol, 56*(20), 6677-6691. doi:10.1088/0031-9155/56/20/011

Grupen, C., & Buvat, I. (2011). *Handbook of particle detection and imaging*: Springer Science & Business Media.

Grupen, C., & Shwartz, B. (2008). *Particle detectors* (Vol. 26): Cambridge university press.

Guan, F., Peeler, C., Bronk, L., Geng, C., Taleei, R., Randeniya, S., . . . Mohan, R. (2015). Analysis of the track-and dose-averaged LET and LET spectra in proton therapy using the geant4 Monte Carlo code. *Medical physics, 42*(11), 6234-6247.

Gueulette, J., Böhm, L., Coster, B., Vynckier, S., Octave-Prigot, M., Schreuder, A. N., . . . Scalliet, P. (1997). RBE variation as a function of depth in the 200-MeV proton beam produced at the National Accelerator Centre in Faure. *Radiat Oncol, 42*, 303-309.

Hall, E. J. (2009). Radiation biology for pediatric radiologists *Pediatric radiology* (Vol. 39, pp. 57-64). http://radiologykey.com/radiation-bioeffects-risks-and-radiation-protection-in-medical-imaging-in-children/: Accessed on 11.01.2017.

Hartmann, V. (2016). Anbefaler ny strålebehandling i Norge. Retrieved from http://sykehusbygg.no/anbefaler-ny-stralebehandling-i-norge/

Hawkins, R. B. (1998). A microdosimetric-kinetic theory of the dependence of the RBE for cell death on LET. *Medical physics, 25*(7), 1157-1170.

Helse-Vest, Helse-Sør-Øst, Helse-Midt, Helse-Nord, & Helsedirektoratet. (2013). *Planlegging av norsk senter for partikkelterapi*. Retrieved from http://ous.prod.fpl.nhn.no/SiteCollectionDocuments/Aktuelt/Prosjekter/Planlegging%20av%20norsk%20senter%20for%20partikkelterapi%202013.pdf

Henley, E. M., & Garcia, A. (2012). Passage of Radiation Through Matter *Subatomic Physics* (3rd ed., pp. 39-52): WORLD SCIENTIFIC.

ICRU. (1998). *Fundamental Quantities and Units for Ionizing Radiation* (Vol. 60): International Commission on Radiation.

ICRU. (2014). Spread out Bragg peak. In S. o. B. peak (Ed.), (pp. Spread out Bragg peak). Journal of the ICRU Website: http://jicru.oxfordjournals.org/content/7/2/11/F4.large.jpg: ICRU, Accessed on September 17, 2014.

Joiner, M. C., & Field, S. B. (1988). The response of mouse skin to irradiation with neutrons from the 62 MV cyclotron at Clatterbridge, UK. *Radiotherapy and Oncology, 12*(2), 153-166.

Joiner, M. C., & van der Kogel, A. (2009). *Basic Clinical Radiobiology* (4th ed.).

Jones, B. (2015). Towards achieving the full clinical potential of proton therapy by inclusion of LET and RBE models. *Cancers, 7*(1), 460-480.

Jones, B., Underwood, T. S., & Dale, R. G. (2011). The potential impact of relative biological effectiveness uncertainty on charged particle treatment prescriptions. *Br J Radiol, 84 Spec No 1*, S61-69. doi:10.1259/bjr/36792876

Kaderka, R., Schardt, D., Durante, M., Berger, T., Ramm, U., Licher, J., & La Tessa, C. (2012). Out-of-field dose measurements in a water phantom using different radiotherapy modalities. *Physics in medicine and biology, 57*(16), 5059.

Kalos, M. H., & Whitlock, P. A. (2008). *Monte carlo methods*: John Wiley & Sons.

Kellerer, A. M. (2002). Electron spectra and the RBE of X rays. *Radiation Research, 158*(1), 13-22.

Kellerer, A. M., & Rossi, H. H. (1978). A generalized formulation of dual radiation action. *Radiation Research, 75*(3), 471-488.

Kelley, M. R. (2011). *DNA repair in cancer therapy: molecular targets and clinical applications*: Academic Press.

Khan, F. M., & Gibbons, J. P. (2014). *Khan's the physics of radiation therapy*: Lippincott Williams & Wilkins.

Larsen, I. K., Johannesen, T. B., Grumsrud, T. K., Larønningen, S., Møller, B., Robsahm, T. E., & Ursin, G. (2015). *Cancer in Norway 2014*. Oslo: Cancer Registry of Norway.

Lea, D. E. (1946). *Actions of radiations on living cells*: University Press, Cambridge.

Lederman, M. (1981). The Early History of Radiotherapy - 1895-1939. *International Journal of Radiation Oncology Biology Physics, 7*(5), 639-648. doi:doi:10.1016/0360-3016(81)90379-5

Li, Z. (2009). ICRU Report 78 Prescribing, Recording, and Reporting Proton-Beam Therapy. *International Journal of Radiation Oncology * Biology * Physics*(73.5).
Mairani, A., Magro, G., Dokic, I., Valle, S. M., Tessonnier, T., Galm, R., . . . Bohlen, T. T. (2016). Data-driven RBE parameterization for helium ion beams. *Phys Med Biol, 61*(2), 888-905. doi:10.1088/0031-9155/61/2/888
McDonald, M. W., & Fitzek, M. M. (2010). Proton therapy. *Curr Probl Cancer, 34*(4), 257-296. doi:10.1016/j.currproblcancer.2010.04.008
McNamara, A. L., Schuemann, J., & Paganetti, H. (2015). A phenomenological relative biological effectiveness (RBE) model for proton therapy based on all published in vitro cell survival data. *Phys Med Biol, 60*(21), 8399-8416. doi:10.1088/0031-9155/60/21/8399
Meroli, S. (2012). Multiple scattering for particles in the matter. (pp. Effect of Multiple Coulomb Scattering). http://meroli.web.cern.ch/meroli/lecture_multiple_scattering.html.
Oxford, U. o. (2015). Introduction. In G. o. r. dose (Ed.), (pp. Graph of radiation dose with respect to depth into tissue for a proton beam). Particle Therapy Cancer Research Institute (Webpage): University of Oxford.
Paganetti, H. (2011). *Proton Therapy Physics*. Boca Raton, UNITED STATES: CRC Press.
Paganetti, H. (2014). Relative biological effectiveness (RBE) values for proton beam therapy. Variations as a function of biological endpoint, dose, and linear energy transfer. *Phys Med Biol, 59*(22), R419-472. doi:10.1088/0031-9155/59/22/R419
Paganetti, H. (2015). Relating proton treatments to photon treatments via the relative biological effectiveness—should we revise current clinical practice? *Int J Radiat Oncol Biol Phys, 91*, 892-894.
Paganetti, H., Niemierko, A., Ancukiewicz, M., Gerweck, L. E., Goitein, M., Loeffler, J. S., & Suit, H. D. (2002). Relative biological effectiveness (RBE) values for proton beam therapy. *Int J Radiat Oncol Biol Phys, 53*(2), 407-421.
Perris, A., Pialoglou, P., Katsanos, A. A., & Sideris, E. G. (1986). Biological effectiveness of low energy protons. I. Survival of Chinese hamster cells. *International Journal of Radiation Biology and Related Studies in Physics, Chemistry and Medicine, 50*(6), 1093-1101.
Polster, L., Schuemann, J., Rinaldi, I., Burigo, L., McNamara, A. L., Stewart, R. D., . . . Paganetti, H. (2015). Extension of TOPAS for the simulation of proton radiation effects considering molecular and cellular endpoints. *Phys Med Biol, 60*(13), 5053-5070. doi:10.1088/0031-9155/60/13/5053
Saha, G. B. (2012). *Physics and radiobiology of nuclear medicine*: Springer Science & Business Media.
Sam Beddar, A., & Krishnan, S. (2005). Depth-dose curves for electron beams. In D.-d. c. f. e. beams (Ed.), (pp. Depth-dose curves for electron beams). Journal of Applied Clinical Madical Physics: http://www.jacmp.org/index.php/jacmp/article/view/2109/1220: JACMP, Accessed 09.01.2016.
Schardt, D., Elsässer, T., & Schulz-Ertner, D. (2010). Heavy-ion tumor therapy: physical and radiobiological benefits. *Reviews of modern physics, 82*(1), 383.
Schettino, G., Folkard, M., Prise, K. M., Vojnovic, B., Bowey, A. G., & Michael, B. D. (2001). Low-dose hypersensitivity in Chinese hamster V79 cells targeted with counted protons using a charged-particle microbeam. *Radiation Research, 156*(5), 526-534.
Schippers, J. (2009). Beam delivery systems for particle radiation therapy: current status and recent developments. *Reviews of Accelerator Science and Technology, 2*(01), 179-200.

Schulz-Ertner, D., Jäkel, O., & Schlegel, W. (2006). *Radiation therapy with charged particles.* Paper presented at the Seminars in radiation oncology.
Sgura, A. A., R. Cherubini, M. Dalla Vecchia, P. Tiveron, F. Degrassi, C. Tanzarella, A. (2000). Micronuclei, CREST-positive micronuclei and cell inactivation induced in Chinese hamster cells by radiation with different quality. *International Journal of Radiation Biology, 76*(3), 367-374.
Spadinger, I., & Palcic, B. (1992). The relative biological effectiveness of 60Co γ-rays, 55 kVp X-rays, 250 kVp X-rays, and 11 MeV electrons at low doses. *International Journal of Radiation Biology, 61*(3), 345-353.
Stathakis, S., Defoor, D., Saenz, D., Kirby, N., Mavroidis, P., & Papanikolaou, N. (2016). SU-G-TeP1-14: SRS Dose Calculation Accuracy Comparison Between Pencil Beam and Monte Carlo Algorithms. *Med Phys, 43*(6), 3655. doi:10.1118/1.4957004
Stokkevag, C. H. (2016). *Model-based predictions of secondary cancer and late effect risks following particle therapy.* (PhD), University of Bergen, Norway.
Tilly, N., Brahme, A., Carlsson, J., & Glimelius, B. (1999). Comparison of cell survival models for mixed LET radiation. *International Journal of Radiation Biology, 75*(2), 233-243.
Wedenberg, M. (2014). Dose distribution photons vs protons.
Wedenberg, M., Lind, B. K., & Hardemark, B. (2013). A model for the relative biological effectiveness of protons: the tissue specific parameter alpha/beta of photons is a predictor for the sensitivity to LET changes. *Acta Oncol, 52*(3), 580-588. doi:10.3109/0284186X.2012.705892
Wilkens, J. J., & Oelfke, U. (2004). A phenomenological model for the relative biological effectiveness in therapeutic proton beams. *Phys Med Biol, 49*(13), 2811-2825. doi:10.1088/0031-9155/49/13/004
Wilson, R. R. (1946). Radiological Use of Fast Protons. *Radiology, 47*(5), 487-491. doi:doi:10.1148/47.5.487
Wouters, B. G., Lam, G. K. Y., Oelfke, U., Gardey, K., Durand, R. E., & Skarsgard, L. D. (1996). Measurements of relative biological effectiveness of the 70 MeV proton beam at TRIUMF using Chinese hamster V79 cells and the high-precision cell sorter assay. *Radiation Research, 146*(2), 159-170.
Yamashita, T., Akagi, T., Aso, T., Kimura, A., & Sasaki, T. (2012). Effect of inhomogeneity in a patient's body on the accuracy of the pencil beam algorithm in comparison to Monte Carlo. *Phys Med Biol, 57*(22), 7673-7688. doi:10.1088/0031-9155/57/22/7673
Ytre-Hauge, K. (2013). *Measurements and Monte Carlo simulations of neutron doses from radiation therapy with photons, protons and carbon ions.* PhD thesis, PhD dissertation. University of Bergen.
Ånensen, N. (2013). Treffsikker strålebehandling av kreft. Retrieved from http://forskning.no/medisinske-metoder-kreft/2013/09/treffsikker-stralebehandling-av-kreft

Appendix A

DVHs and RBE-VHs for the other structures than shown in figures 5-10 and 5-12. Structures Uterus/Cervix and Vertebrae were not included due to very low doses (D_2 < 0.5 Gy) and poor resolution.

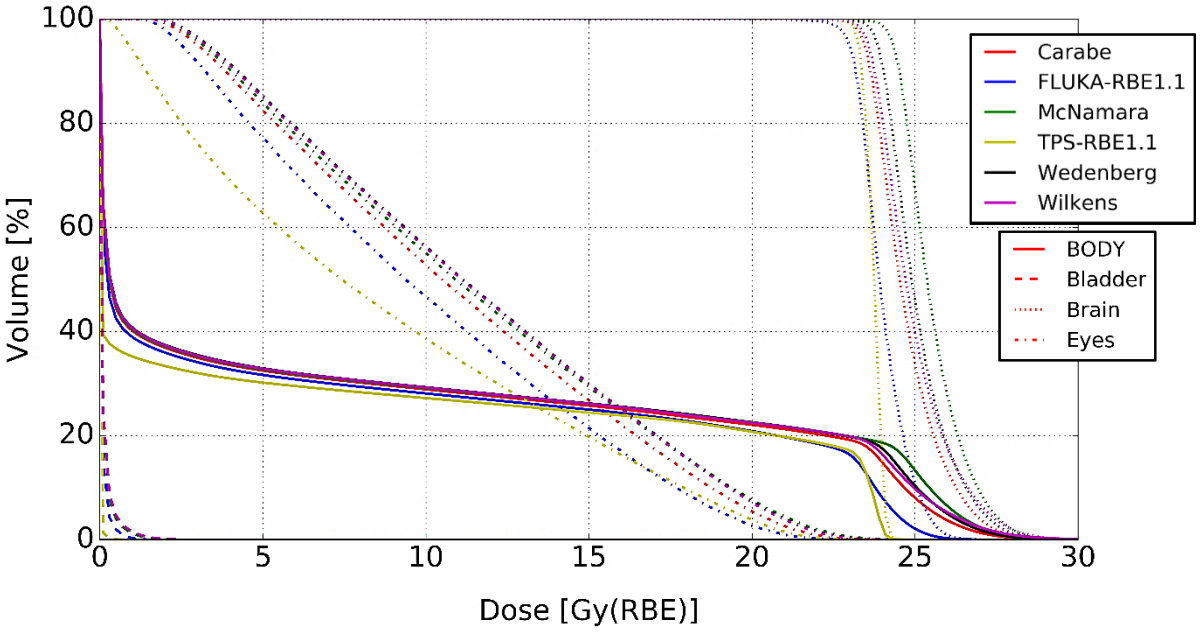

Figure A-1: DVH with additional structures. Specific data found in Appendix C.

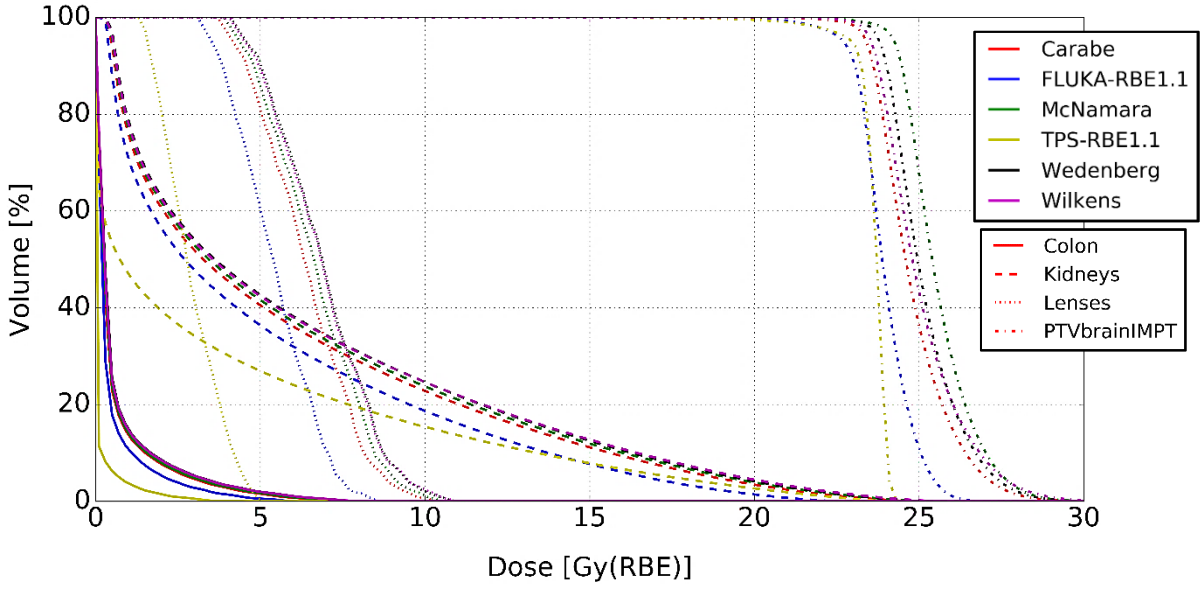

Figure A-2: DVH with additional structures. Specific data found in Appendix C.

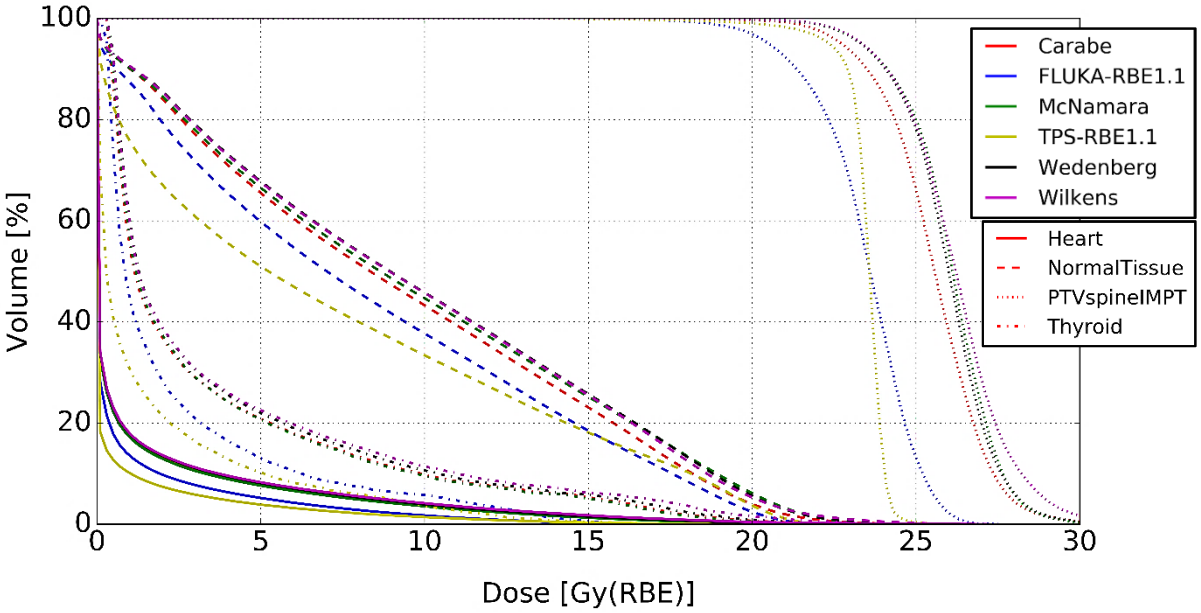

Figure A-3: DVH with additional structures. Specific data found in Appendix C.

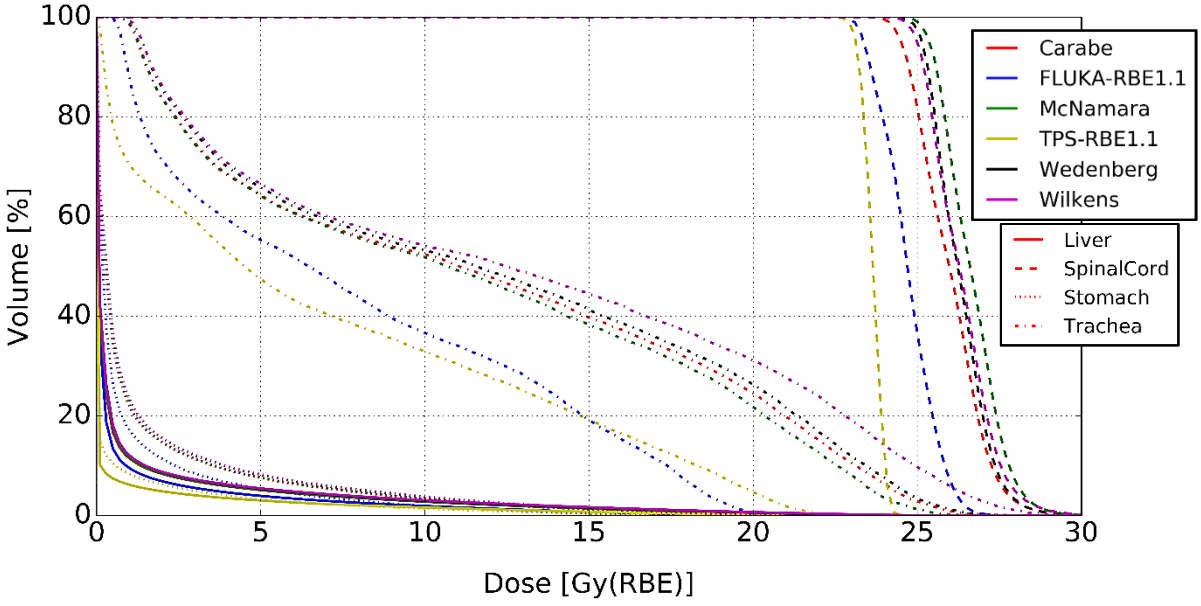

Figure A-4: DVH with additional structures. Specific data found in Appendix C.

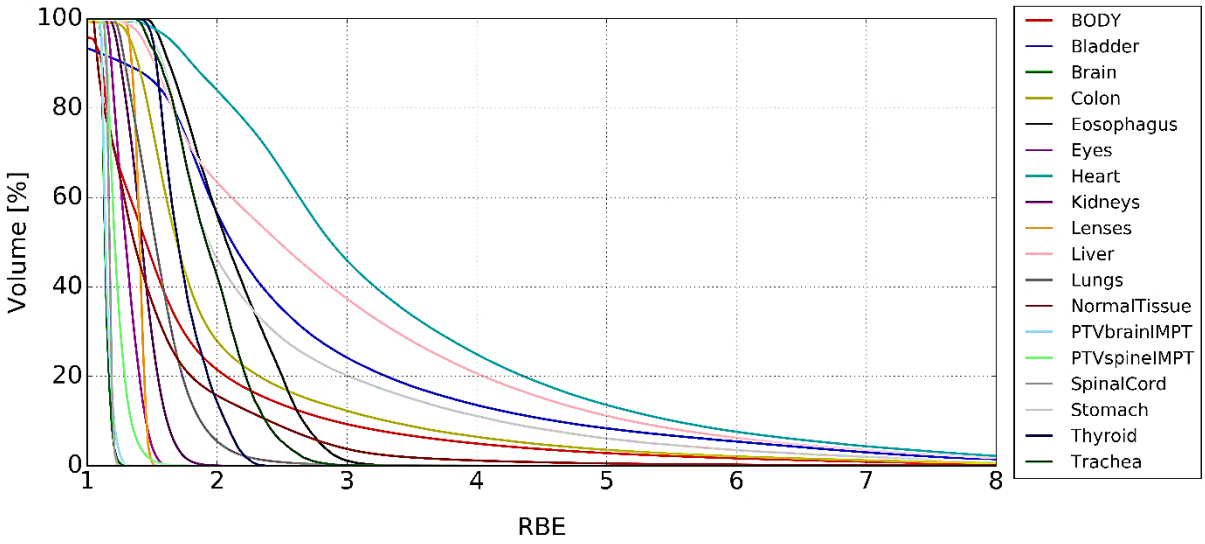

Figure A-5: RBE Volume Histogram for Wilkens model only, with all structures. Specific data found in Appendix C.

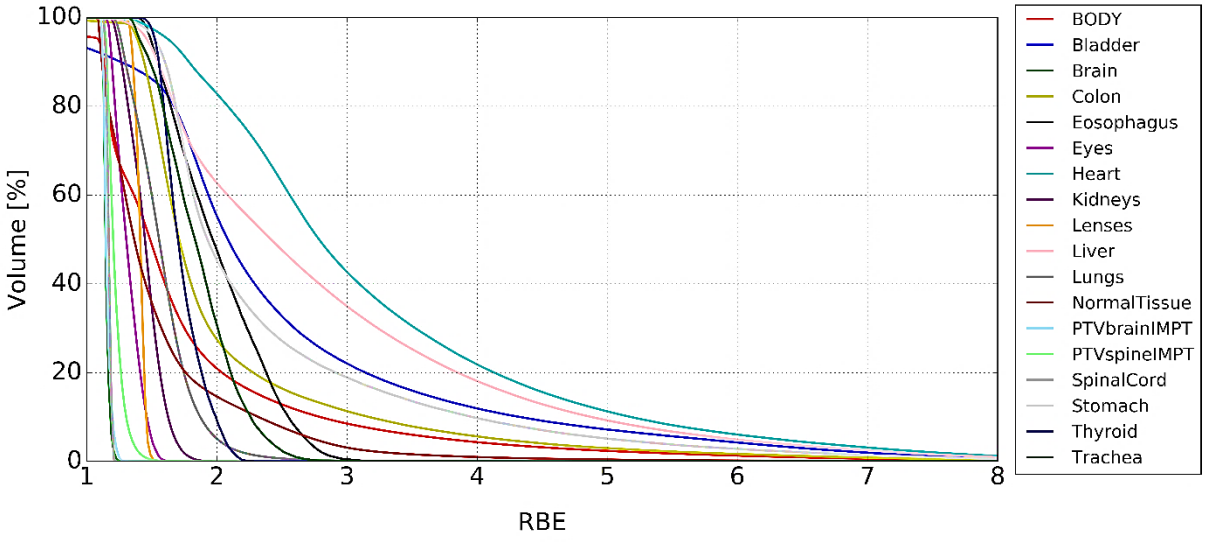

Figure A-6: RBE Volume Histogram for Wedenberg model only, with all structures. Specific data found in Appendix C.

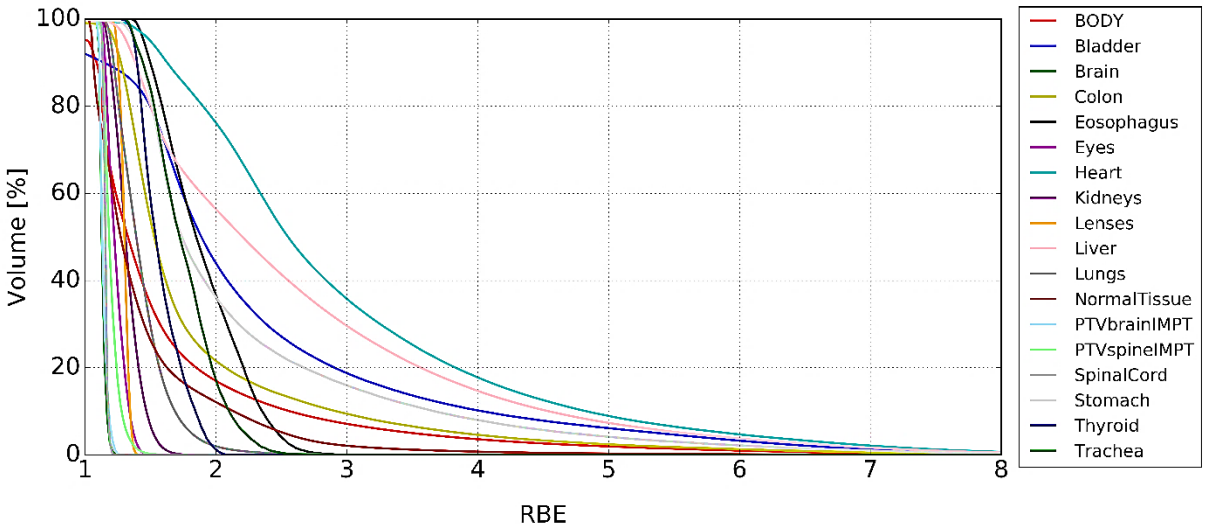

Figure A-7: RBE Volume Histogram for Carabe model only, with all structures. Specific data found in Appendix C.

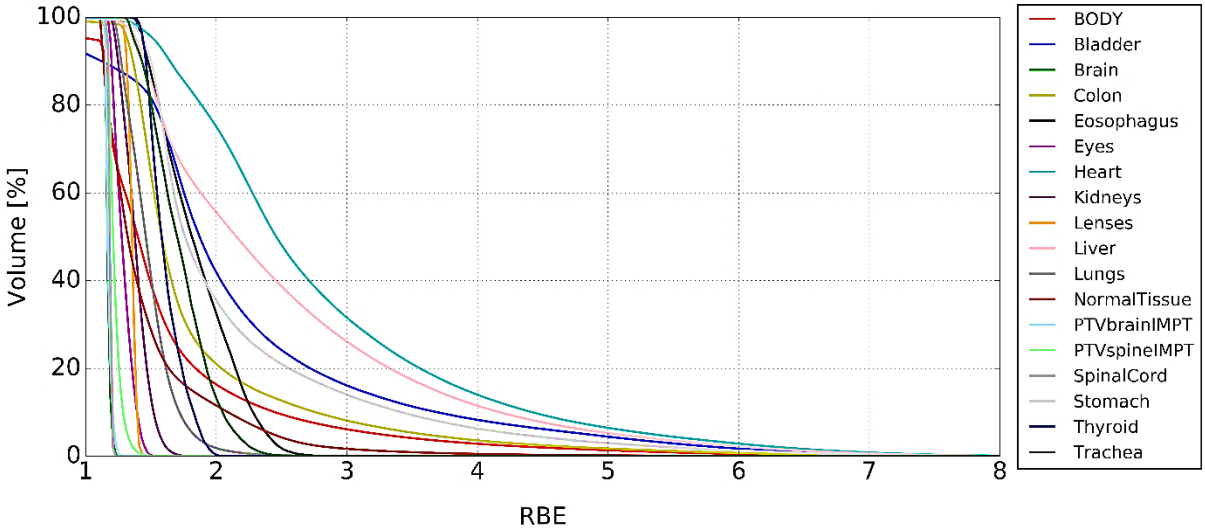

Figure A-8: RBE Volume Histogram for McNamara model only, with all structures. Specific data found in Appendix C.

Appendix B

Sub-formulas used to calculate the uncertainty of the RBE and how they are derived. B.1 is the uncertainty of the RBE formula 3.10. Using B.2, formulas B.3-B.5 are derived. Figures B-1 and B-2 shows the relative uncertainty calculated for the physical dose and the RBE for the water phantom.

$$\delta RBE = \sqrt{\left(\frac{\partial RBE}{\partial D}\delta D\right)^2 + \left(\frac{\partial RBE}{\partial RBE_{max}}\delta RBE_{max}\right)^2 + \left(\frac{\partial RBE}{\partial RBE_{min}}\delta RBE_{min}\right)^2} \quad (B.1)$$

$$U = \left(\frac{\alpha}{\beta}\right)_x^2 + 4RBE_{max}\left(\frac{\alpha}{\beta}\right)_x D + 4RBE_{min}^2 D^2 \quad (B.2)$$

$$\frac{\partial RBE}{\partial RBE_{max}} \rightarrow Product\ rule \rightarrow \sqrt{U}'(2D)^{-1} - \sqrt{U}((2D)^{-1})' = \sqrt{U}'(2D)^{-1} = \frac{\sqrt{U}'}{2D}$$

$$\sqrt{U}' = \frac{\partial\sqrt{U}}{\partial RBE_{max}} \rightarrow Chain\ rule \rightarrow \frac{\partial\sqrt{U}}{\partial U} * \frac{\partial U}{\partial RBE_{max}} = \frac{1}{2\sqrt{U}} * 4\left(\frac{\alpha}{\beta}\right)_x = \frac{2\left(\frac{\alpha}{\beta}\right)_x}{\sqrt{U}}$$

$$\frac{\partial RBE}{\partial RBE_{max}} = \frac{\frac{2\left(\frac{\alpha}{\beta}\right)_x}{\sqrt{U}}}{2D} \quad (B.3)$$

$$\frac{\partial RBE}{\partial RBE_{min}} \rightarrow Product\ rule \rightarrow \sqrt{U}'(2D)^{-1} + \sqrt{U}((2D)^{-1})' = \sqrt{U}'(2D)^{-1} = \frac{\sqrt{U}'}{2D}$$

$$\sqrt{U}' = \frac{\partial\sqrt{U}}{\partial RBE_{min}} \rightarrow Chain\ rule \rightarrow \frac{\partial\sqrt{U}}{\partial U} * \frac{\partial U}{\partial RBE_{min}} = \frac{1}{2\sqrt{U}} * 4RBE_{min}D = \frac{2RBE_m}{\sqrt{U}}$$

$$\frac{\partial RBE}{\partial RBE_{min}} = \frac{\frac{2RBE_{min}D}{\sqrt{U}}}{2D} \quad (B.4)$$

$$\frac{\partial RBE}{\partial D} \rightarrow Quotient\ rule \rightarrow \frac{\left(\sqrt{U} - \left(\frac{\alpha}{\beta}\right)_x\right)' 2D - \left(\sqrt{U} - \left(\frac{\alpha}{\beta}\right)_x\right)(2D)'}{(2D)^2}$$

$$\left(\sqrt{U} - \left(\frac{\alpha}{\beta}\right)_x\right)' = \sqrt{U}' = \frac{\partial\sqrt{U}}{\partial D} \rightarrow Chain\ rule \rightarrow \frac{\partial\sqrt{U}}{\partial U} * \frac{\partial U}{\partial D}$$

$$= \frac{1}{2\sqrt{U}} * \left(4RBE_{max}\left(\frac{\alpha}{\beta}\right)_x + 4RBE_{min}^2 D\right)$$

$$= \frac{2RBE_{max}\left(\frac{\alpha}{\beta}\right)_x + 2RBE_{min}^2 D}{\sqrt{U}}$$

$$\frac{\partial RBE}{\partial D} = \frac{\left(\frac{2RBE_{max}\left(\frac{\alpha}{\beta}\right)_x + 2RBE_{min}^2 D}{\sqrt{U}}\right) * 2D - 2\left(\sqrt{U} - \left(\frac{\alpha}{\beta}\right)_x\right)}{4D^2} \qquad (B.5)$$

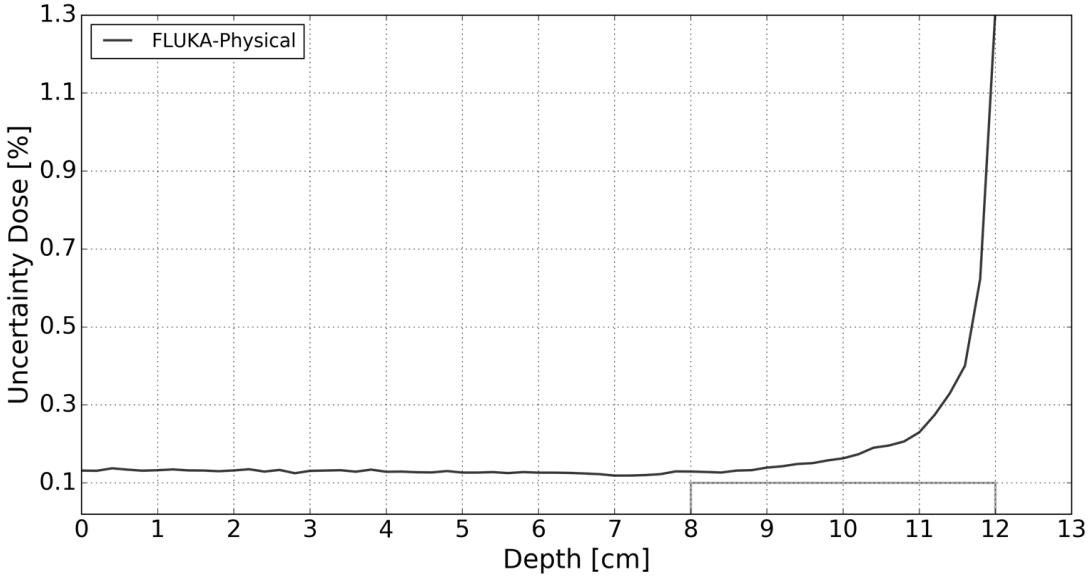

Figure B-1: 1D uncertainty plot for the physical dose of the water phantom. The grey box shows the boundary of the PTV on the depth-axis.

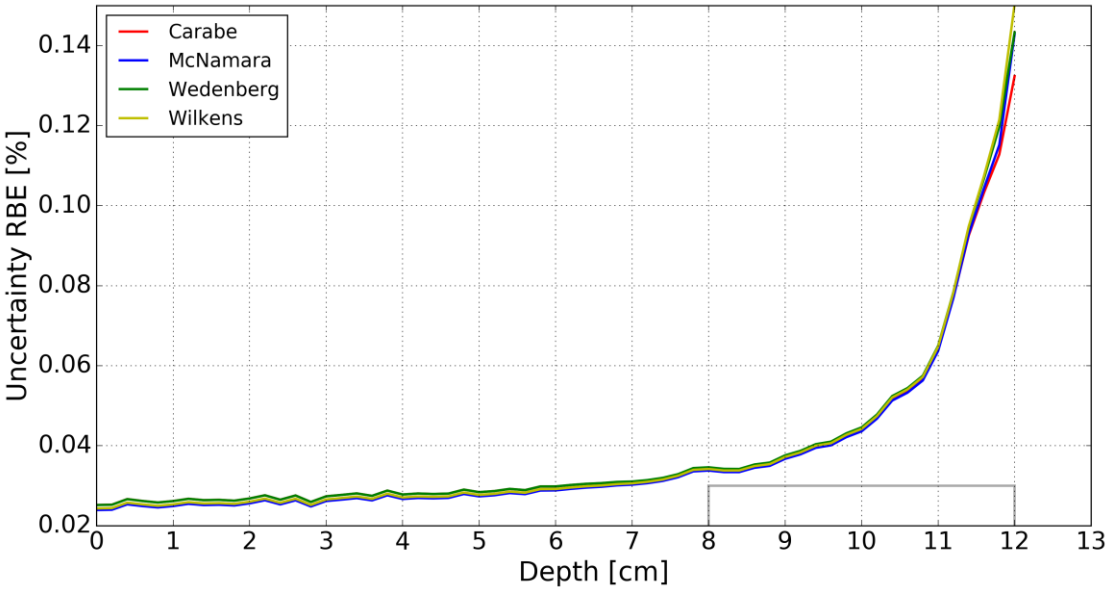

Figure B-2: 1D uncertainty plot for the RBE of the water phantom. The grey box shows the boundary of the PTV on the depth-axis.

Appendix C

Data from the figures in Appendix A. Table C-A lists the dose at a specific volume amount [%] as well as the mean dose in a structure. Table C-B lists RBE.

Table C-A: Patient dose coverage comparison other structures

	TPS	FLUKA	WIL	WED	CAR	MCN
Body						
D_{98}	0.0033	0.0048	0.0056	0.0056	0.0054	0.0055
D_{80}	0.0330	0.0484	0.0562	0.0566	0.0542	0.0550
D_{50}	0.0825	0.2431	0.3226	0.3317	0.2925	0.3005
D_{2}	24.031	25.035	27.193	26.922	26.634	27.150
Mean	6.2154	6.5599	7.1552	7.1690	6.9890	7.2038
Bladder						
D_{98}	0.0020	0.0023	0.0026	0.0026	0.0026	0.0026
D_{80}	0.0202	0.0235	0.0267	0.0266	0.0260	0.0261
D_{50}	0.0506	0.0589	0.0667	0.0667	0.0651	0.0652
D_{2}	0.0993	0.4964	0.8806	0.8793	0.7950	0.8070
Mean	0.0042	0.0569	0.1042	0.1038	0.0936	0.0945
Brain						
D_{98}	23.146	22.728	23.356	23.648	23.236	24.123
D_{80}	23.501	23.399	24.022	24.275	23.886	24.753
D_{50}	23.746	23.905	24.710	24.897	24.535	25.364
D_{2}	24.219	25.741	27.968	27.714	27.449	27.976
Mean	23.723	24.012	24.972	25.114	24.758	25.554
Colon						
D_{98}	0.0022	0.0066	0.0084	0.0084	0.0081	0.0082
D_{80}	0.0225	0.0660	0.0849	0.0848	0.0818	0.0820
D_{50}	0.0564	0.1966	0.2744	0.2816	0.2491	0.2605
D_{2}	1.6549	3.4698	4.9647	4.9669	4.5253	4.6724
Mean	0.1063	0.4335	0.6423	0.6480	0.5841	0.6050
Esophagus						
D_{98}	0.1324	0.1617	0.3726	0.3700	0.3356	0.3323
D_{80}	1.1724	1.2298	2.8440	2.7251	2.5151	2.4527
D_{50}	4.7533	6.1931	11.676	10.977	10.424	10.170
D_{2}	16.087	17.551	25.262	23.882	23.381	22.951
Mean	5.6292	6.8298	11.505	10.837	10.412	10.172
Eyes						
D_{98}	0.5481	1.9828	2.5807	2.6406	2.3735	2.5166
D_{80}	2.5130	4.5775	5.8147	5.8783	5.3912	5.6371
D_{50}	7.4210	9.3741	11.087	11.141	10.490	10.905
D_{2}	20.746	20.355	21.723	21.792	21.291	21.985
Mean	8.6135	9.9618	11.440	11.493	10.931	11.346

Heart						
D_{98}	0.0024	0.0027	0.0030	0.0030	0.0029	0.0029
D_{80}	0.0244	0.0278	0.0303	0.0302	0.0298	0.0297
D_{50}	0.0611	0.0695	0.0758	0.0755	0.0746	0.0743
D_{2}	8.3848	9.4817	14.450	13.840	13.182	13.117
Mean	0.5570	0.7417	1.2461	1.2000	1.1278	1.1196
Kidneys						
D_{98}	0.0056	0.3262	0.4164	0.4460	0.3704	0.3952
D_{80}	0.0560	0.6800	0.9199	0.9473	0.8472	0.8880
D_{50}	0.7360	2.6946	3.5666	3.6245	3.2745	3.4402
D_{2}	20.821	19.310	22.304	21.998	21.478	21.880
Mean	3.8563	5.0576	6.2234	6.2153	5.8554	6.0474
Lenses						
D_{98}	1.4544	3.2715	4.2430	4.2930	3.8930	4.0930
D_{80}	2.0174	4.2420	5.4420	5.4810	5.0420	5.2577
D_{50}	2.7764	5.3900	6.8500	6.8818	6.3333	6.6300
D_{2}	4.7651	7.8280	10.128	10.028	9.4280	9.7280
Mean	2.8861	5.4161	6.8718	6.9073	6.3852	6.6467
Liver						
D_{98}	0.0022	0.0030	0.0035	0.0034	0.0034	0.0034
D_{80}	0.0222	0.0309	0.0350	0.0349	0.0342	0.0342
D_{50}	0.0556	0.0774	0.0875	0.0873	0.0856	0.0856
D_{2}	8.2988	9.7575	13.701	13.315	12.659	12.767
Mean	0.4464	0.6448	0.9475	0.9277	0.8706	0.8793
Lungs						
D_{98}	0.0033	0.0647	0.1172	0.1183	0.1109	0.1130
D_{80}	0.0330	0.2384	0.3691	0.3756	0.3351	0.3490
D_{50}	0.0825	0.6529	0.9394	0.9583	0.8569	0.8884
D_{2}	20.299	19.349	23.113	22.610	22.151	22.376
Mean	2.3852	3.2226	4.0301	4.0075	3.7909	3.8943
Normal Tissue						
D_{98}	0.0236	0.0375	0.0526	0.0520	0.0499	0.0493
D_{80}	0.6663	1.9310	2.8209	2.8512	2.5762	2.6781
D_{50}	5.2403	7.0219	8.9303	8.9513	8.3442	8.6537
D_{2}	20.615	20.208	21.742	21.505	20.995	21.594
Mean	7.2695	8.1549	9.5316	9.5658	9.0878	9.4206
PTVbrain						
D_{98}	21.929	21.936	23.298	23.519	23.106	23.889
D_{80}	23.417	23.340	24.041	24.278	23.888	24.741
D_{50}	23.715	23.881	24.797	24.956	24.593	25.399
D_{2}	24.213	25.780	28.338	27.988	27.716	28.179
Mean	23.610	23.945	25.073	25.174	24.818	25.581

PTVspine						
D_{98}	21.231	19.530	22.533	22.507	21.875	22.469
D_{80}	23.211	22.334	24.947	24.906	24.364	25.007
D_{50}	23.581	23.601	26.219	26.005	25.571	26.111
D_{2}	24.400	26.056	29.853	28.864	28.740	28.759
Mean	23.461	23.425	26.192	25.927	25.518	26.007
PTV						
D_{98}	21.755	21.016	23.185	23.326	22.842	23.486
D_{80}	23.379	23.237	24.098	24.317	23.919	24.757
D_{50}	23.696	23.851	24.995	25.110	24.733	25.507
D_{2}	24.239	25.837	28.802	28.222	27.973	28.306
Mean	23.581	23.847	25.276	25.310	24.944	25.657
Spinal Cord						
D_{98}	22.984	23.178	24.777	24.946	24.282	25.153
D_{80}	23.368	23.944	25.452	25.541	25.051	25.840
D_{50}	23.650	24.700	26.285	26.234	25.978	26.611
D_{2}	24.240	26.455	28.591	28.246	28.232	28.622
Mean	23.641	24.725	26.338	26.303	25.997	26.659
Stomach						
D_{98}	0.0023	0.0050	0.0059	0.0058	0.0057	0.0057
D_{80}	0.0235	0.0501	0.0591	0.0589	0.0577	0.0576
D_{50}	0.0587	0.1890	0.3090	0.3117	0.2758	0.2837
D_{2}	7.9692	9.8179	13.705	13.320	12.651	12.761
Mean	0.4858	0.9318	1.4088	1.3847	1.2872	1.3034
Thyroid						
D_{98}	0.0066	0.1873	0.3522	0.3572	0.3286	0.3357
D_{80}	0.0664	0.4410	0.6536	0.6628	0.5951	0.6204
D_{50}	0.2889	0.8546	1.2658	1.2788	1.1426	1.1925
D_{2}	11.934	13.206	19.417	18.414	17.836	17.637
Mean	1.5857	2.2512	3.6821	3.5433	3.3333	3.3155
Trachea						
D_{98}	0.1063	0.6641	1.1772	1.1756	1.0706	1.1027
D_{80}	0.4561	1.3210	2.7116	2.6314	2.4130	2.3779
D_{50}	4.5169	6.4673	12.472	11.570	11.050	10.690
D_{2}	20.955	19.291	27.398	25.628	25.419	24.676
Mean	7.1100	7.8296	12.736	11.941	11.593	11.278

Structures Uterus/Cervix and Vertebrae were not included due to very low doses ($D_2 < 0.5$ Gy) and poor resolution.

Table C-B: Patient RBE coverage comparison other structures

	WIL	WED	CAR	MCN
Body				
RBE_{98}	0.3950	0.3912	0.3517	0.3480
RBE_{80}	1.1809	1.1949	1.1508	1.1856
RBE_{50}	1.4504	1.4858	1.3322	1.3981
RBE_{2}	5.6736	5.2996	4.9577	4.5026
Mean	1.7755	1.7568	1.6189	1.6209
Bladder				
RBE_{98}	0.4475	0.4408	0.3967	0.3876
RBE_{80}	1.6461	1.6587	1.4968	1.5199
RBE_{50}	2.1177	2.0871	1.8911	1.8776
RBE_{2}	7.5408	6.9854	6.5692	5.8730
Mean	2.5905	2.4965	2.2925	2.1905
Brain				
RBE_{98}	1.1037	1.1040	1.1038	1.1040
RBE_{80}	1.1398	1.1400	1.1398	1.1400
RBE_{50}	1.1999	1.2000	1.1999	1.2000
RBE_{2}	1.2960	1.2960	1.2960	1.2960
Mean	1.1436	1.1502	1.1339	1.1704
Colon				
RBE_{98}	1.2128	1.3081	1.1145	1.1778
RBE_{80}	1.4602	1.5134	1.3409	1.4037
RBE_{50}	1.6904	1.7154	1.5375	1.6001
RBE_{2}	6.0937	5.6892	5.3209	4.8348
Mean	2.0828	2.0639	1.8672	1.8674
Esophagus				
RBE_{98}	1.5127	1.3705	1.3398	1.3315
RBE_{80}	1.7441	1.6427	1.5838	1.5586
RBE_{50}	2.0752	1.9719	1.8565	1.8188
RBE_{2}	2.9433	2.8455	2.6268	2.4965
Mean	2.1214	2.0165	1.8988	1.8542
Eyes				
RBE_{98}	1.1078	1.1082	1.1050	1.1066
RBE_{80}	1.1781	1.1825	1.1501	1.1665
RBE_{50}	1.2953	1.3065	1.2252	1.2664
RBE_{2}	1.6058	1.6204	1.4804	1.4912
Mean	1.3087	1.3177	1.2365	1.2873
Heart				
RBE_{98}	1.5007	1.4543	1.3554	1.3655
RBE_{80}	2.1260	2.0849	1.9016	1.8878
RBE_{50}	2.8807	2.7930	2.5574	2.4650
RBE_{2}	8.1046	7.5219	7.0678	6.3476
Mean	3.3540	3.2079	2.9625	2.8064

Kidneys				
RBE_{98}	1.1213	1.1247	1.1085	1.1164
RBE_{80}	1.3047	1.3158	1.1859	1.2646
RBE_{50}	1.4190	1.4386	1.3147	1.3824
RBE_{2}	1.8008	1.8017	1.6463	1.6751
Mean	1.4307	1.4491	1.3228	1.3826
Lenses				
RBE_{98}	1.3030	1.3040	1.1084	1.1857
RBE_{80}	1.3395	1.3404	1.1848	1.3321
RBE_{50}	1.4005	1.4010	1.3107	1.3951
RBE_{2}	1.4980	1.4980	1.4924	1.4958
Mean	1.4012	1.4102	1.3002	1.3549
Liver				
RBE_{98}	1.3238	1.3336	1.1894	1.3039
RBE_{80}	1.6567	1.6751	1.5019	1.5633
RBE_{50}	2.4769	2.4185	2.2057	2.1568
RBE_{2}	7.8151	7.2603	6.8139	6.1228
Mean	2.9746	2.8692	2.6369	2.5276
Lungs				
RBE_{98}	1.1348	1.1386	1.1133	1.1251
RBE_{80}	1.3498	1.3657	1.2336	1.3191
RBE_{50}	1.5282	1.5592	1.3992	1.4590
RBE_{2}	2.2548	2.2273	2.0248	2.0195
Mean	1.5662	1.5830	1.4335	1.4874
Normal Tissue				
RBE_{98}	0.9268	1.0051	0.9194	1.1086
RBE_{80}	1.1374	1.1881	1.0943	1.1866
RBE_{50}	1.3729	1.3798	1.2772	1.3307
RBE_{2}	3.4501	3.3019	3.0492	2.8896
Mean	1.5733	1.5638	1.4558	1.4848
PTVbrain				
RBE_{98}	1.1038	1.1040	1.1038	1.1040
RBE_{80}	1.1399	1.1400	1.1398	1.1400
RBE_{50}	1.2001	1.2000	1.1999	1.2000
RBE_{2}	1.2964	1.2960	1.2960	1.2960
Mean	1.1517	1.1564	1.1399	1.1751
PTVspine				
RBE_{98}	1.1045	1.1044	1.1038	1.1043
RBE_{80}	1.1478	1.1447	1.1427	1.1432
RBE_{50}	1.2201	1.2119	1.2074	1.2081
RBE_{2}	1.4906	1.4687	1.4489	1.4495
Mean	1.2329	1.2201	1.2003	1.2232

PTV				
RBE_{98}	1.1039	1.1041	1.1039	1.1041
RBE_{80}	1.1412	1.1408	1.1404	1.1406
RBE_{50}	1.2033	1.2020	1.2012	1.2014
RBE_{2}	1.3840	1.3000	1.2986	1.2988
Mean	1.1667	1.1605	1.1511	1.1840
Spinal Cord				
RBE_{98}	1.1040	1.1040	1.1040	1.1040
RBE_{80}	1.1400	1.1400	1.1400	1.1400
RBE_{50}	1.2000	1.2000	1.2000	1.2000
RBE_{2}	1.2960	1.2960	1.2960	1.2960
Mean	1.1718	1.1703	1.1564	1.1861
Stomach				
RBE_{98}	1.3809	1.3927	1.3090	1.3282
RBE_{80}	1.6596	1.6756	1.5173	1.5590
RBE_{50}	1.9452	1.9369	1.7533	1.7820
RBE_{2}	7.0154	6.5407	6.1336	5.5287
Mean	2.4819	2.4219	2.2140	2.1647
Thyroid				
RBE_{98}	1.3961	1.4668	1.3089	1.3173
RBE_{80}	1.5687	1.5745	1.3961	1.4732
RBE_{50}	1.6989	1.7022	1.5496	1.6037
RBE_{2}	2.2554	2.1623	2.0330	1.9975
Mean	1.7481	1.7373	1.5806	1.6130
Trachea				
RBE_{98}	1.3615	1.3365	1.3250	1.3210
RBE_{80}	1.6538	1.5761	1.5256	1.5069
RBE_{50}	1.9159	1.8342	1.7230	1.7011
RBE_{2}	2.6755	2.5392	2.3769	2.2835
Mean	1.9504	1.8559	1.7558	1.7234

Structures Uterus/Cervix and Vertebrae were not included due to very low doses ($D_2 < 0.5$ Gy) and poor resolution.

Appendix D

The following figures are additional patient slices. The slice used in section 5.2 is located at chest height. Figures D-1, D-3, D-5, D-7 and D-8 are of a patient slice slightly below shoulder height. Figure D-2, D-4, D-6 and D-9 are of a head slice at the eyes level. DVHs and data for the structures are found in appendix A and appendix C.

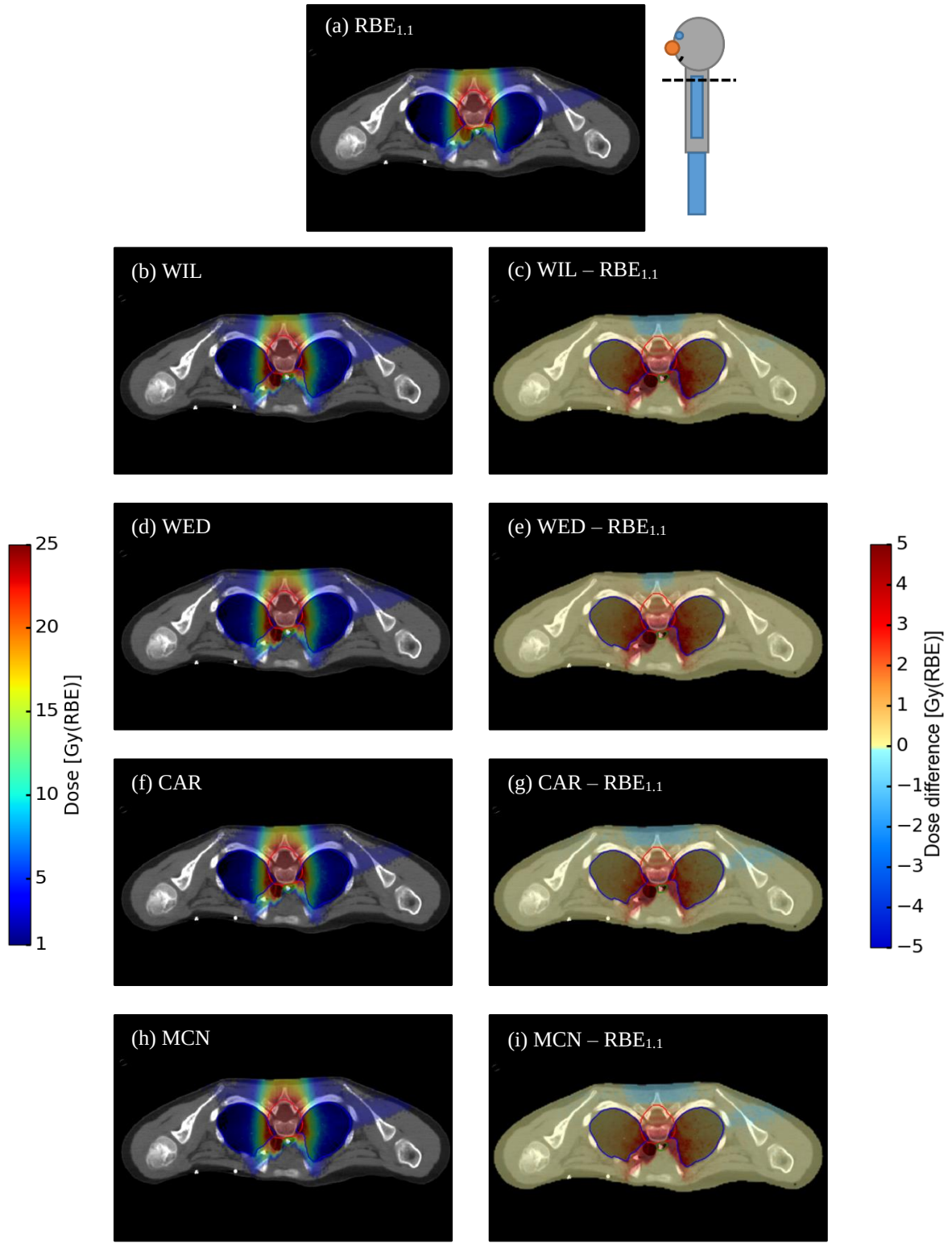

Figure D-1: 2D patient dose distribution plots of the different models used in the thesis. The left column shows the different distributions and uses the color bar on the left. The right column shows the difference between the model distributions and the $RBE_{1.1}$ (FLUKA) distribution showed in the top plot, while using the color bar on the right. The PTV is marked by the red curve, while other organs of interest such as the lungs (blue) and esophagus (green) are also marked. The dose values in the left column are transparent if the dose is less than 1 Gy. The axes in this figure are not shown, but are identical to that of figure 5-7.

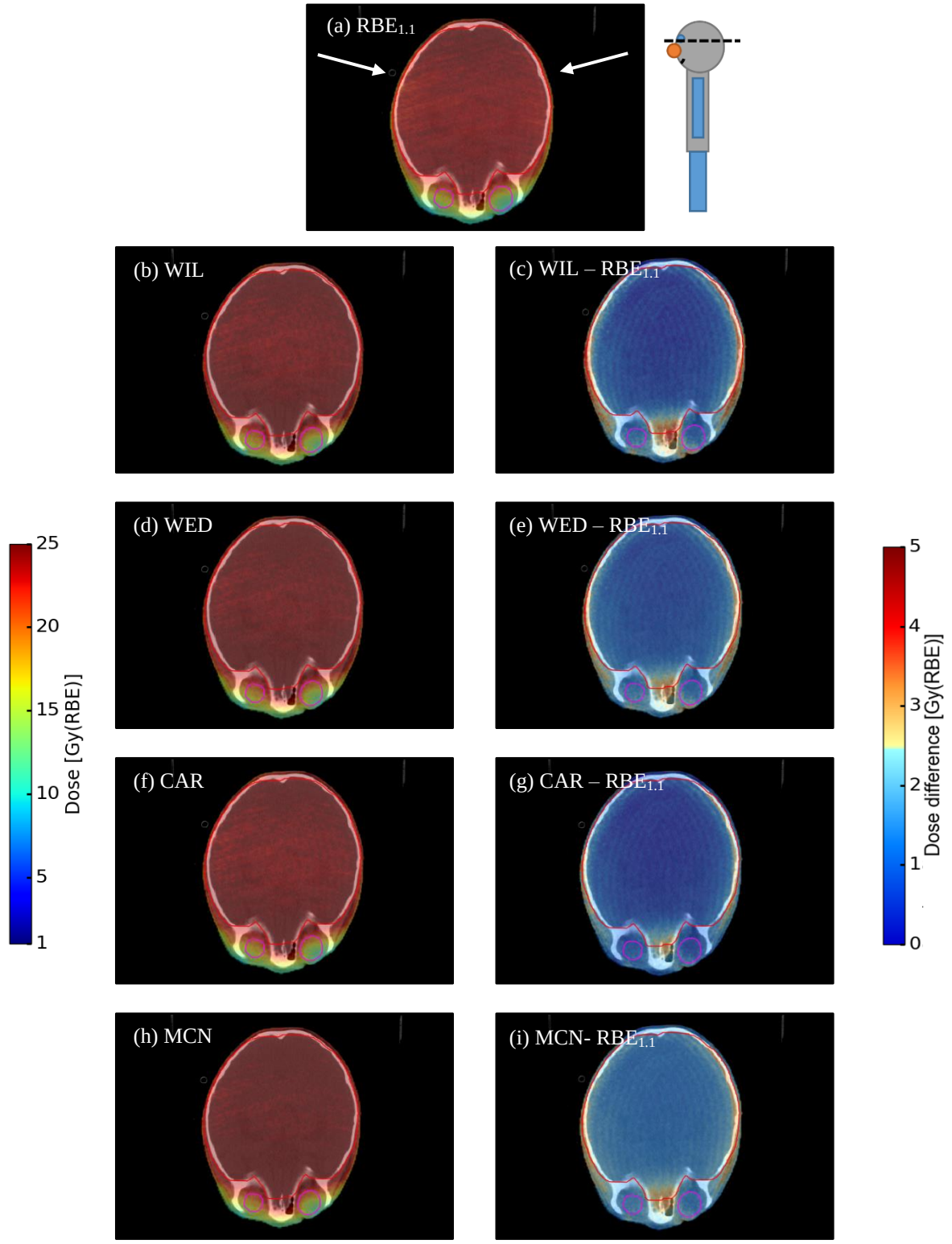

Figure D-2: 2D patient dose distribution plots of the different models used in the thesis. The left column shows the different distributions and uses the color bar on the left. The right column shows the difference between the model distributions and the FLUKA ($RBE_{1.1}$) distribution showed in the top plot, while using the color bar on the right. The PTV is marked by the red curve, while other organs of interest such as the eyes (pink) are also marked. The dose values in the left column are transparent if the dose is less than 1 Gy. The axes in this figure are not shown, but are identical to that of figure 5-7. Unlike for the other dose distribution figures, the colorbar is between 0 and 5. The head/brain was irradiated by two different fields, from roughly ±75 degrees of the depth axis as seen in (a). The artifacts on the top left and right are part of the apparatus holding the head in place.

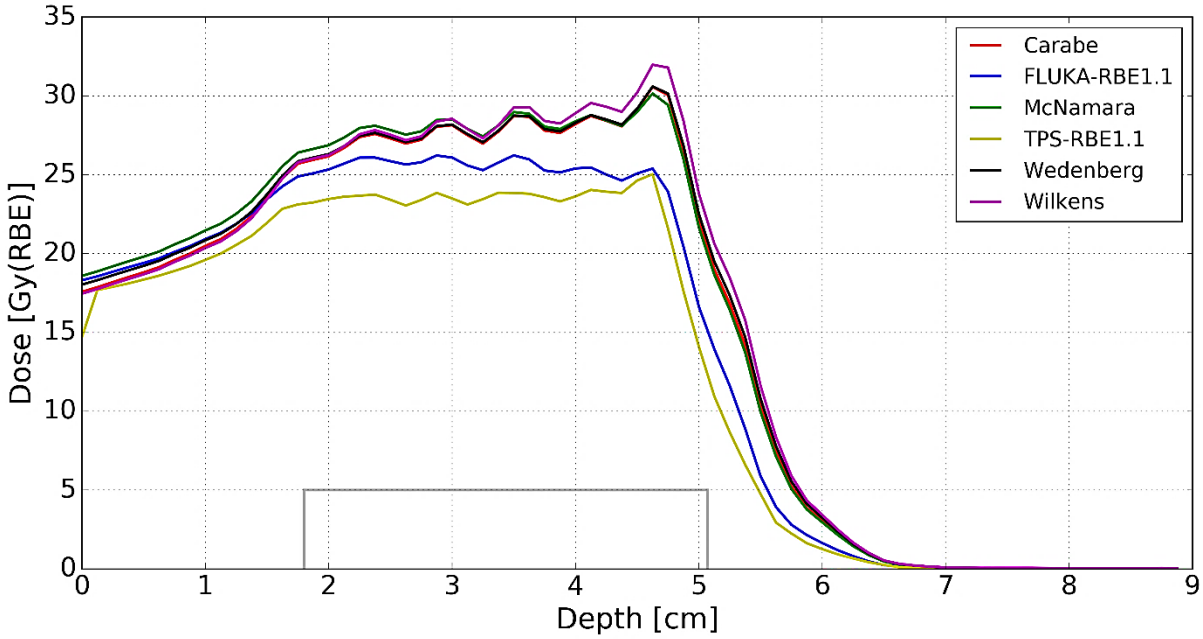

Figure D-3: 1D depth equivalent to figure D-1 (shoulder). Depth = 0 cm refers to the point of entry into the patient, while approx. 9 cm is the point of exit. Note that the grey box which shows the boundary of the PTV on the depth-axis is the equivalent to the red curve in the 2D plot.

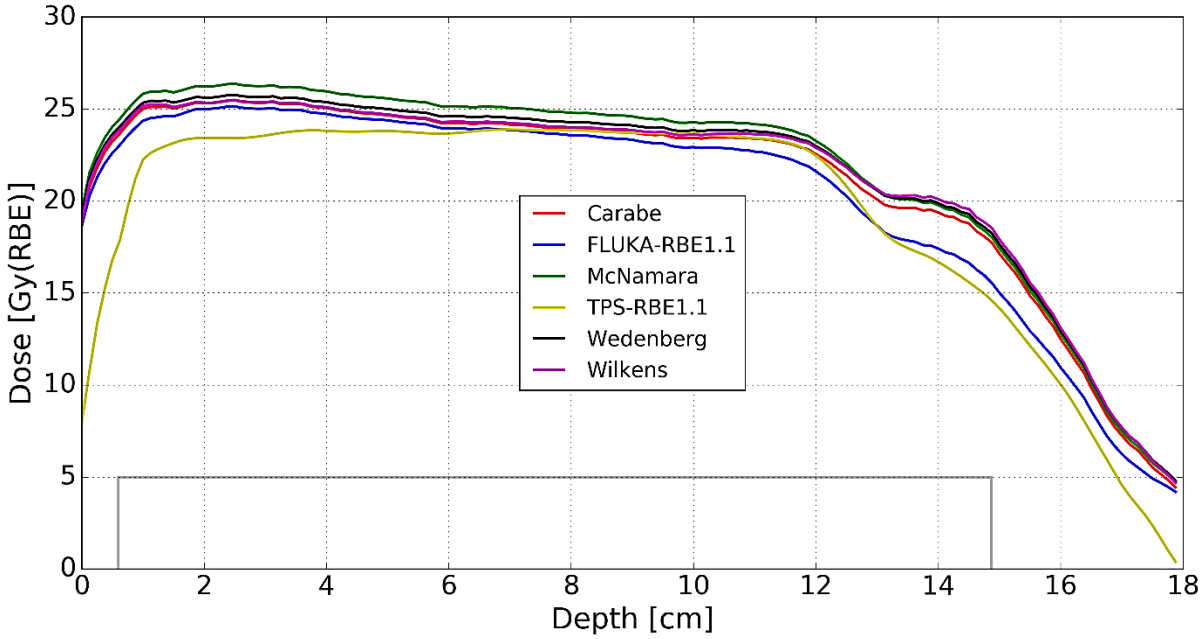

Figure D-4: 1D depth equivalent to figure D-2 (head). Depth = 0 cm refers to the back of the patient head, while approx. 18 cm is the front of the head. Note that the grey box which shows the boundary of the PTV on the depth-axis is the equivalent to the red curve in the 2D plot. The head/brain was irradiated by two different fields, from roughly ±75 degrees of the depth axis as seen in D-2(a).

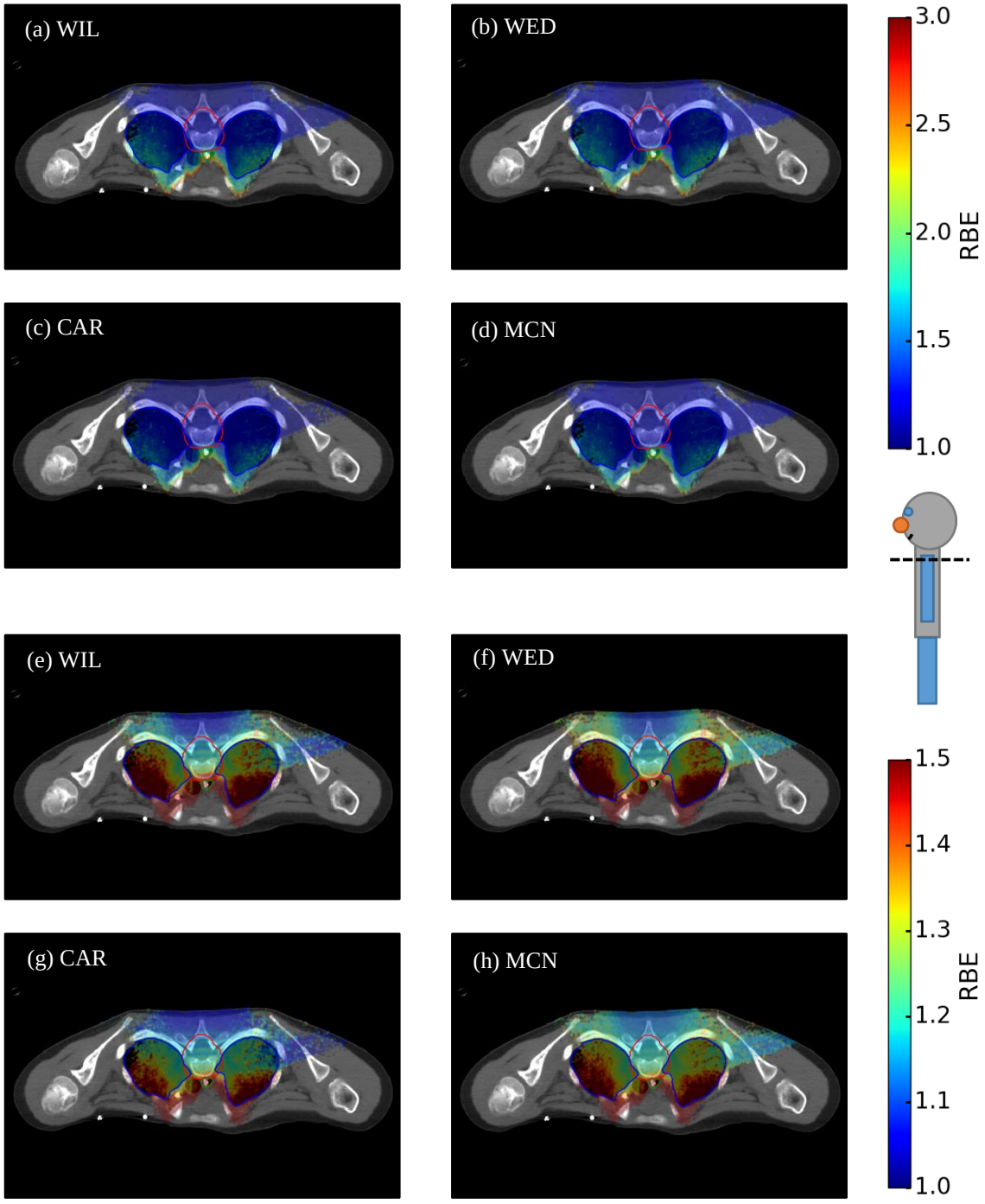

Figure D-5: RBE distributions of the second slice of the patient. The top 4 plots (a-d) has a wide RBE range (1-3), while the bottom 4 (e-h) has a narrow RBE range (1-1.5). Marked structures are the PTV (red), lungs (blue) and esophagus (green). The dose values in the plots are transparent if the dose is less than 1 Gy. The axes in this figure are not shown, but are identical to that of figure 5-7.

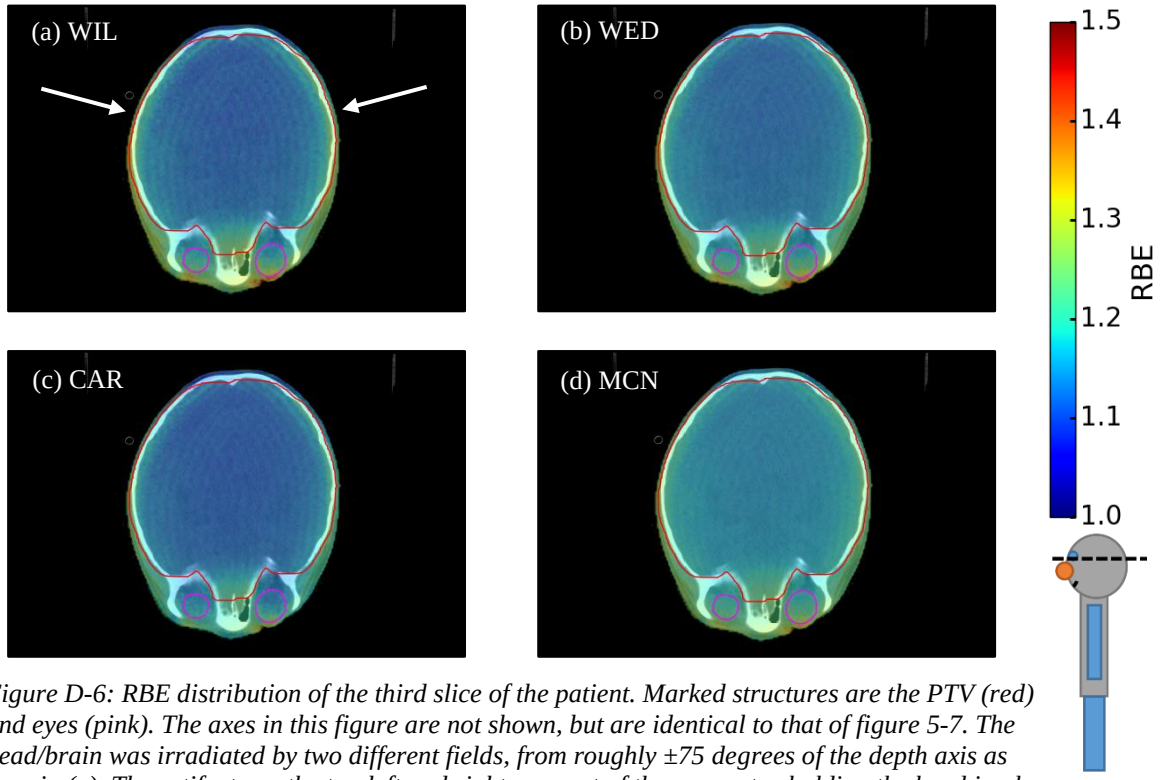

Figure D-6: RBE distribution of the third slice of the patient. Marked structures are the PTV (red) and eyes (pink). The axes in this figure are not shown, but are identical to that of figure 5-7. The head/brain was irradiated by two different fields, from roughly ±75 degrees of the depth axis as seen in (a). The artifacts on the top left and right are part of the apparatus holding the head in place.

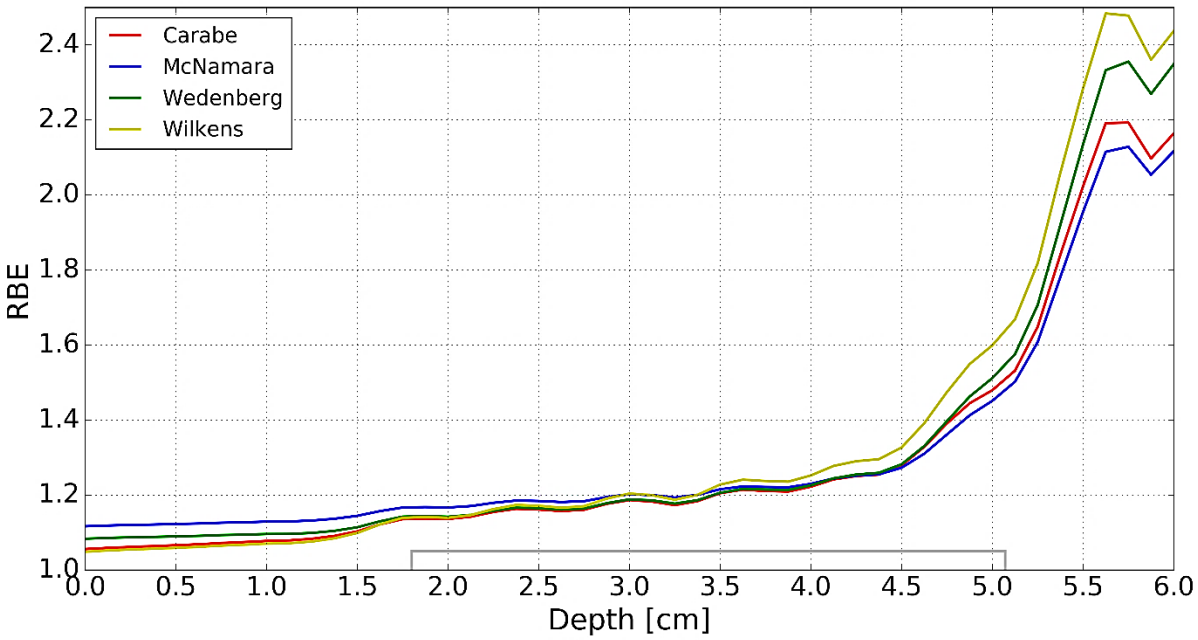

Figure D-7: 1D depth equivalent to figure D-5 (shoulder). Note that the grey box which shows the boundary of the PTV on the depth-axis is the equivalent to the red box in the 2D plot. Depth = 0 refers to the beam-entry point of the patient.

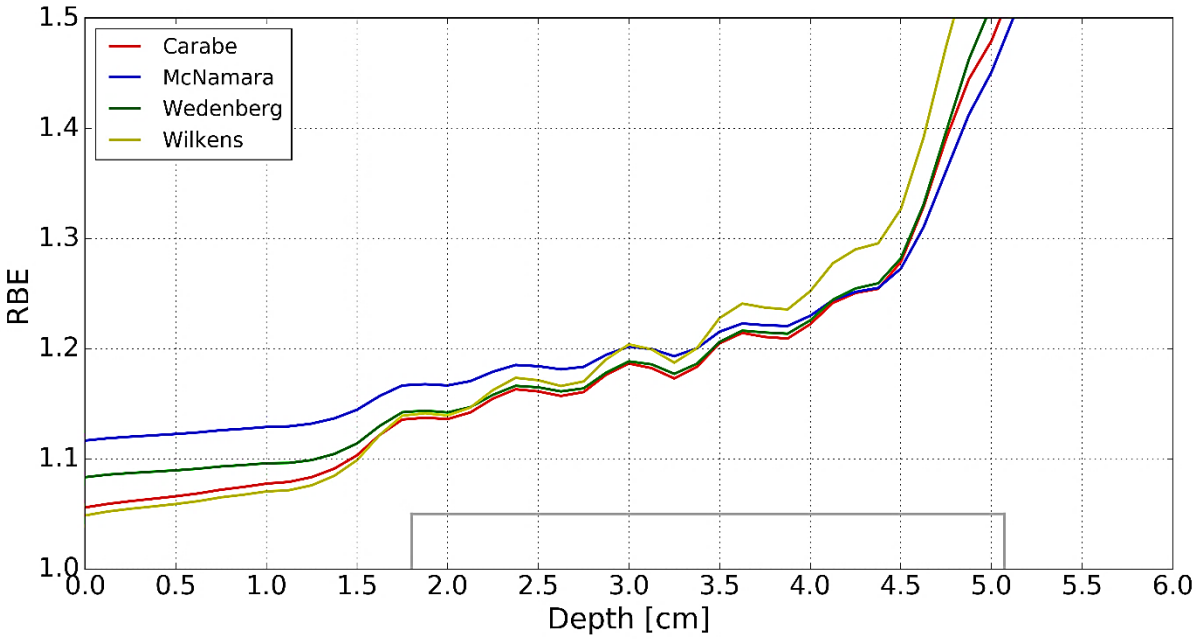

Figure D-8: 1D depth equivalent to figure D-5 (shoulder), with a narrower RBE range. Note that the grey box which shows the boundary of the PTV on the depth-axis is the equivalent to the red box in the 2D plot. Depth = 0 refers to the beam-entry point of the patient.

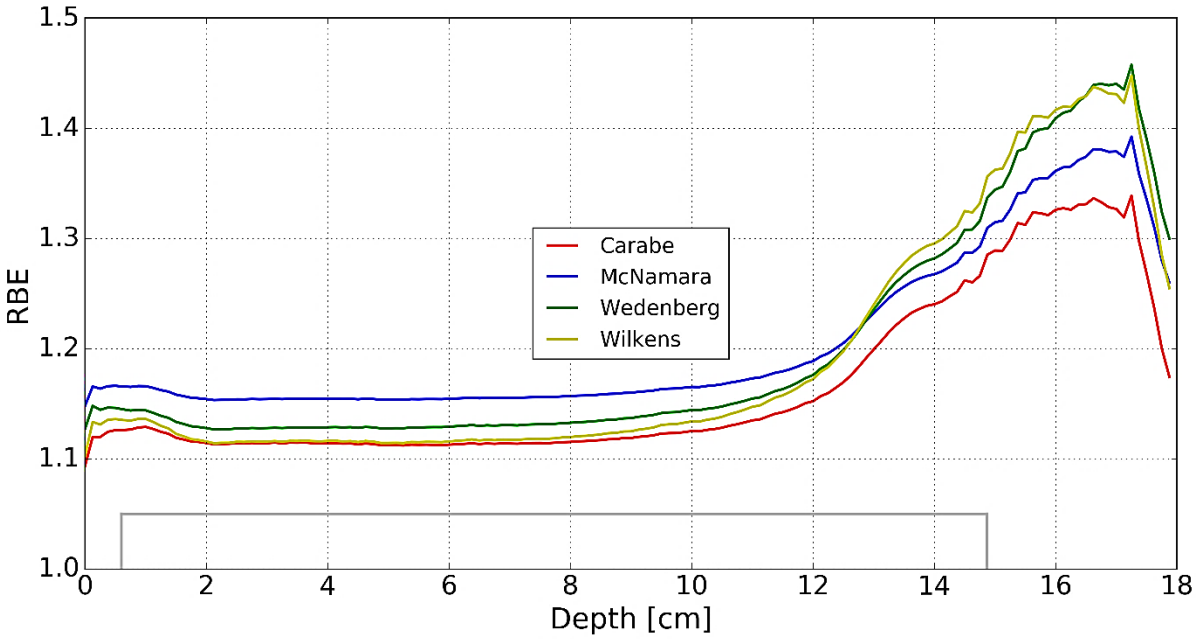

Figure D-9: 1D depth equivalent to figure D-6 (head). Note that the grey box which shows the boundary of the PTV on the depth-axis is the equivalent to the red box in the 2D plot. Depth = 0 refers to the beam-entry point of the patient. The head/brain was irradiated by two different fields, from roughly ±75 degrees of the depth axis as seen in D-6(a).

Appendix E

Figure 5-1a and 5-1b show the two-dimensional dose distributions in the water phantom calculated by the TPS and FLUKA respectively. All the plots are normalized to the average dose in the PTV, on the assumption that the distribution calculated by FLUKA and the TPS are very similar in this region (Fjæra, 2016). From the comparison in figure 5-1c, it would appear that FLUKA scores lower in the center entrance region, while higher in the low-dose regions on the distribution. This is in accordance with the work of Fjæra (Fjæra, 2016).

In the patient case with figure E-2, the FLUKA simulation seems to predict a higher dose in most areas, especially on the edges of the beam (like before) and in the center of the SOBP (like before). There is also dose distributed further past the PTV on the sides, which did not happen with the water phantom.

Figure E-1: Water phantom dose distribution TPS vs FLUKA comparison

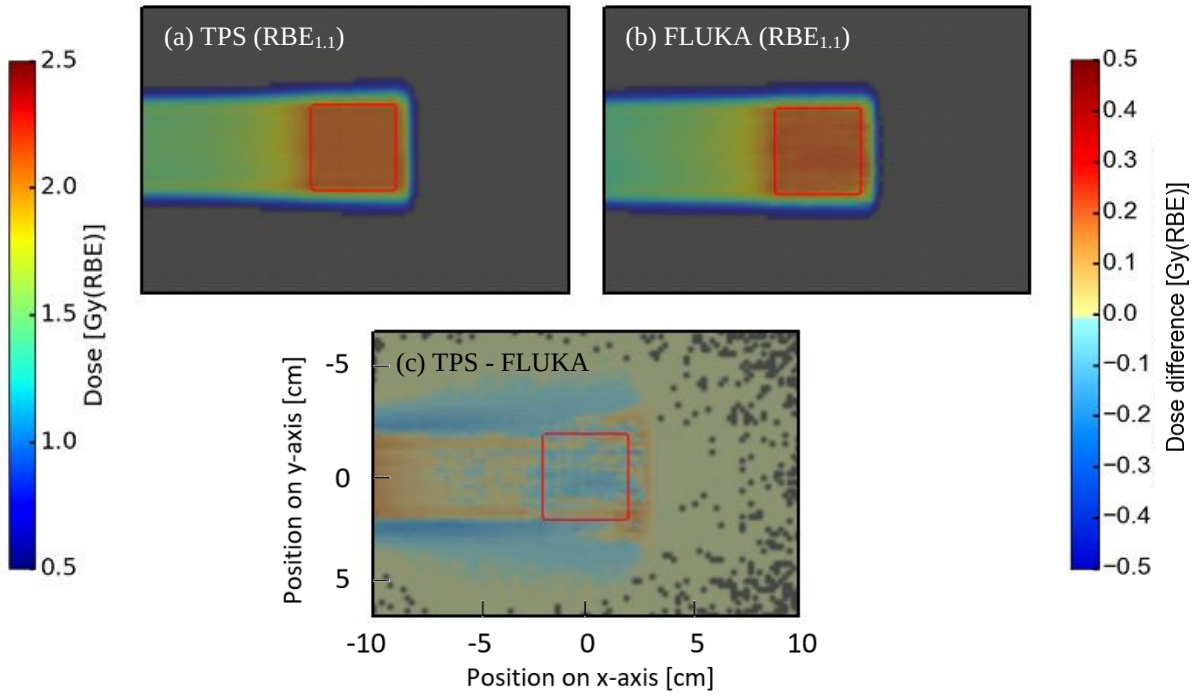

Figure E-1: 2D water phantom dose distribution plots of the TPS (a) vs FLUKA (b). The bottom plot (c) shows the difference between the two, by subtracting the dose value in each voxel in the FLUKA matrix from the TPS matrix. The top plots use the color bar on the left, while the bottom plot uses the one on the right. The PTV is a 4x4x4 cm cube in the center of a 20x20x20 cm water phantom and the displayed slices are located in the center of the phantom and PTV. The dose values in the top plots are transparent if the dose is less than 0.5 Gy.

Figure E-2: Patient [spinal] dose distribution TPS vs FLUKA comparison

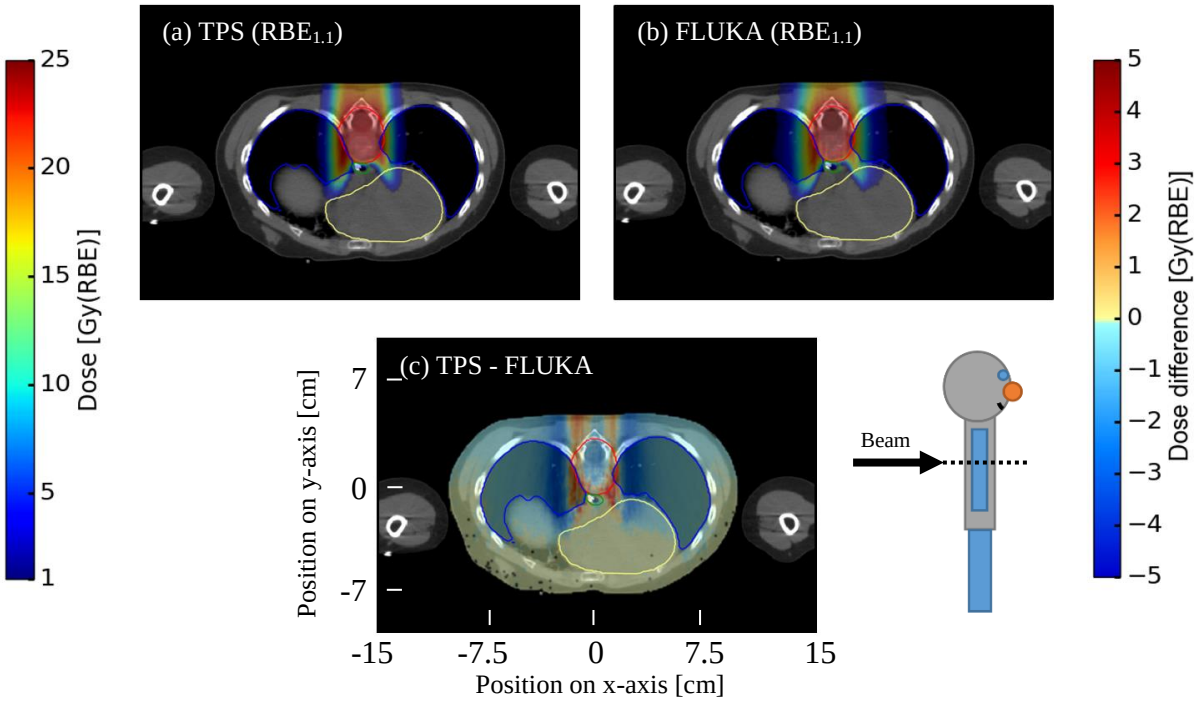

Figure E-2: 2D patient dose distribution plots of the TPS (a) vs FLUKA (b). The bottom plot (c) shows the difference between the two, by subtracting the dose value in each voxel in the FLUKA matrix from the TPS matrix. The top plots use the color bar on the left, while the bottom plot uses the one on the right. The PTV is marked by the red curve, while other organs of interest such as the lungs (blue), heart (yellow) and esophagus (green) are also marked. Due to the way DICOM handles the axes, the center isn't in 0,0 (x,y) as for the water phantom. Therefore, the displayed axes might seem confusing, but are displayed so that the 2D plots may be compared to the 1D plots and their axes. The dose values in the top plots are transparent if the dose is less than 1 Gy.